國立交通大學
土木工程學系碩士班
碩士論文

振動夯實造成土壓力及其應力路徑之變化

Variation of Earth Pressure and Stress Path due to Vibratory Compaction

研 究 生：江奕蓁

指導教授：方永壽 博士

中 華 民 國 九十八 年 九 月

振動夯實造成土壓力及其應力路徑之變化

Variation of Earth Pressure and Stress Path due to Vibratory Compaction

研 究 生: 江奕蓁　　Student：Yi-Jen Jiang

指導教授：方永壽 博士　Advisor：Dr. Yung-Show Fang

國 立 交 通 大 學 土 木 工 程 學 系 碩 士 班

碩士論文

A Thesis

Submitted to the Department of Civil Engineering

College of Engineering

National Chiao Tung University

in Partial Fulfillment of the Requirements

for the Degree of

Master of Engineering

in Civil Engineering

September, 2009

Hsinchu, Taiwan, Republic of China

中華民國九十八年九月

振動夯實造成土壓力及其應力路徑之變化

研究生：江奕蓁　　　指導教授：方永壽 博士

國立交通大學土木工程學系碩士班

摘要

本論文以實驗方法探討振動夯實造成之土壓力及其應力路徑的變化。本研究以氣乾之渥太華砂為回填土，分五層填土並且分層夯實。夯實土層為每層 0.3 m，總高度為 1.5 m.回填土初始相對密度(Dr)為 34.2 %,壓密後的相對密度(Dr)為 73.8 %。為了在實驗室模擬雙向平面應變的情況，本研究採用塑膠膜潤滑層來降低砂土和填砂槽側牆間的摩擦力。本研究進行一連串相關的實驗，來探察振動夯實對砂土所產生的影響。這些影響包括夯實後土壤的應力變化及其動態應力路徑。根據實驗結果，本研究獲得以下幾項結論：

1. 對於疏鬆砂土，土體內的垂直土壓力和水平土壓力可分別以 $\sigma_v = \gamma z$ 和 Jaky 公式來進行合理的估算。

2. 隨著夯實逐漸接近土壓力計，其應力路徑變化越來越明顯；在最靠近擋土牆的地方夯實時,位於土壓力計上方的應力路徑變化是最大的; 隨著覆土深度逐漸升高，因夯實造成之應力變化相當不顯著。

3. 比較各組之應力路徑發現，其大小尺寸是相似的，應力路徑軌跡像是一顆的彗星。而動態應力路徑都介於K_0線及K_p線。

4. 相較於Broms在 1971 提出之加載解載之應力路徑，本實驗量測出的應力路徑軌跡與Broms的應力路徑軌跡有很大的差異。Broms 所提出的應力路徑是在土體上方放置一個很重的且不會振動的壓路機,而本實驗是放置一個重量很輕且具振動力的夯實機。造成差異之原因有可能是因為夯實機不只有垂直方向的出

力(F_z)，還有平行牆面的力（Fy）及與牆表面垂直的力（Fx），這三個方向的出力造成了彗星形狀的應力軌跡。

關鍵字： 砂土、模型試驗、夯實、應力路徑、土壓力

Variation of Earth Pressure and Stress Path due to Vibratory Compaction

Student: Yi-Jen Jiang   Advisor: Dr. Yung-Show Fang

Institute of Civil Engineering

National Chiao Tung University

Abstract

This paper presents experimental data on the variation of earth pressure and dynamic stress path against a nonyielding retaining wall due to soil filling and vibratory compaction. The instrumented nonyielding wall facility at National Chiao Tung University in Taiwan was used to investigate the effects of vibratory compaction on the change of dynamic stress path. In this study, air-dry Ottawa sand was plated in five lifts and the height of backfill was 1.5 m. The initial relative density D_r of the backfill was 34.2 %, and the compacted relative density D_r of the backfill was 73.8 % . To simulate a plane strain condition in the laboratory, the friction between the soil and sidewalls of the soil bin was reduced with a lubrication layer. The variation of dynamic stress path was measured during compaction with a vibratory compactor. Based on the test results, the following conclusions were drawn.

1. For a loose backfill, the horizontal earth pressure in the soil mass was in good agreement with Jaky's solutions. The vertical earth pressure in soil was near to the equation $\sigma_v = \gamma z$.

2. As the area of the compaction approached the soil pressure transducer (SPT) in x-direction (perpendicular to the wall face), the dynamic stress path became more obvious when the compactor moved to the lane near the wall.

3. As the area of compaction passed the SPT in y-direction (parallel to the wall surface), the maximum dynamic stress path was obvious when the compactor was right in front of the SPT.

4. For a SPT at a lower elevation, when the area of compaction rose with the elevation of the lift surface, the compaction-induced stress path became less significant.

5. The dynamic stress path of a soil element under vibratory compaction had the shape of a comet. The shape size of the dynamic stress paths obtained at five different lifts was quite similar. The stress paths were bounded by the at-rest K_0-line and passive K_p-line.

6. The measured dynamic stress path was quite different from the stress path proposed by Broms (1971). The stress path reported by Broms was induced by a static heavy compactor. The vibratory compactor used in this study vibrated and generated cycle force in three direction: F_x, F_y, and F_z. This was probably the main reason why the dynamic stress path due to vibratory compaction was so different from Broms' finding.

Keywords: sand, model test, compaction, stress path, earth pressure.

ACKNOWLEDGEMENTS

Table of Contents

List of Tables

List of Figures

Lift 5 (Test 0805)

List of Symbols

C_u	Coefficient of uniformity
D_r	Relative density
δ	Friction angle
E	Young's modulus
e_i	Void ratio of soil
e_{max}	Maximum void ratio of soil
e_{min}	Minimum void ratio of soil
ε	Strain
ϕ	Effective stress friction angle
ϕ'	Effective stress friction angle for local shear failure
ϕ_{cv}	Constant-volume friction angle
G_s	Specific gravity of soil
γ	Unit weight of soil
γ_d	Dry unit weight of soil
$\gamma_{d(min)}$	Dry unit weight of soil in the loosest state
H	Thickness of backfill
K_a	Coefficient of active earth pressure
K_h	Coefficient of horizontal earth pressure
K_o	Coefficient of earth pressure at-rest
K_{ol}	Earth pressure coefficient due to locked-in stress
K_{onc}	At-rest earth pressure coefficient for NC soil
K_p	Coefficient of passive earth pressure
ν	Poisson's ratio
OCR	Overconsolidation ratio

P_h Total horizontal force

q_{ult} Ultimate bearing capacity of soil

S Wall movement

σ_1 Major principal stress

σ_3 Minor principal stress

σ_{cyc} Compaction loading

σ_h Effective horizontal stress

$\Delta\sigma_{h,ci}$ Peak compaction-influenced horizontal pressure

σ_n Normal stress

σ_v Effective vertical stress
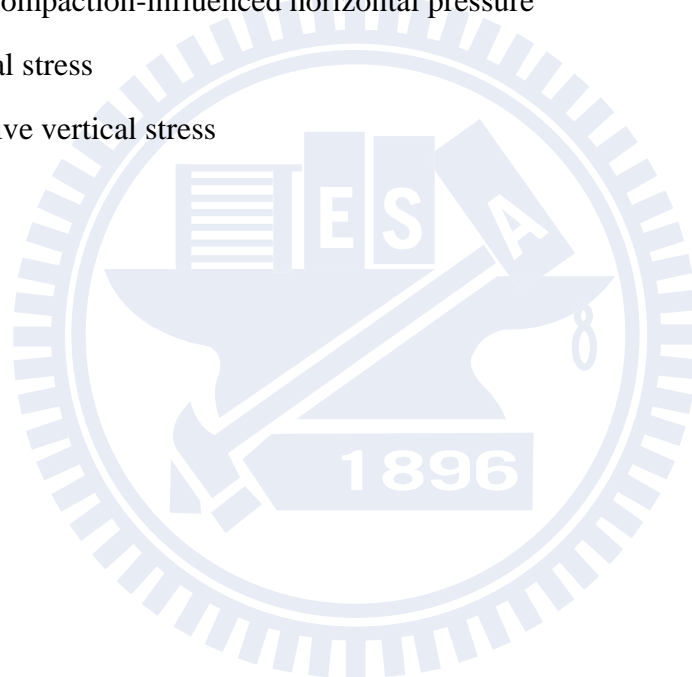
Chapter 1

INTRODUCTION

In the construction of highway embankments, earth dams, and many other engineering structures, engineers will compact loose soils to increase their unit weights. The objective of the compaction operation is to improve the engineering properties of soil such as increasing the fill bearing capacity or reducing settlement. In various methods of compaction, vibratory compactions are used mostly for the densification of granular soils

Before compaction, the vertical earth pressure is calculated by the equation $\sigma_v = \gamma z$,

and the horizontal earth pressure is estimated with Jaky's formula. According to Chengand Fang (2008), it shows the increment of horizontal pressure was more significant than vertical pressure on compaction. In this study, the variation of dynamic stress path will be described and compare to theoretical stress path.

1.1 Objectives of Study

To analyze the residual lateral earth pressure induced by soil compaction, several methods of analysis have been proposed by Broms (1971), Duncan and Seed (1986), Peck and Mesri (1987) and other researchers. Duncan et al. (1991) used the analytical procedures proposed by Duncan and Seed (1986) to develop earth pressure charts and tables that can be used to estimate residual earth pressure due to compaction. However, little information regarding the mechanism of compaction on soil is obtained. This

study presents experimental data to investigate dynamic stress path due to compaction. All experiments mentioned in this study were conducted in the National Chiao Tung University (NCTU) retaining wall facility that is described in Chapter 3. The horizontal and vertical stresses were measured with the soil pressure transducers (SPTs) which mounted on the wall and embedded in the backfill.

1.2 Research Outline

This research utilizes the NCTU model wall facility to investigate the earth pressures against a non-yielding wall. The at-rest earth pressure theory and experimental findings associated with vibratory compaction are summarized in Chapter 2. Details of the NCTU non-yielding model wall system and the vibratory compactor used for the experiments are discussed in Chapter 3. Test results regarding the characteristics of backfill and soil density control are introduced in Chapter 4.

To investigate the earth pressure and dynamic stress path induced by compaction, the backfill was prepared by air-pluviated method and compaction method. A vibratory compactor was employed to densify the cohesionless fill. Experimental results of the earth pressures and stress path due to vibratory compaction are reported in Chapter 5.

1.3 Organization of Dissertation

This paper is divided into the following parts:

1. Review of theories regarding the earth pressure at-rest and past investigations about soil compaction. (Chapter 2)

2. Description of National Chiao Tung University non-yielding retaining-wall facility. (Chapter 3)

3. Backfill characteristics and soil density control. (Chapter 4)

4.Experimental results of earth pressure and dynamic stress path due to vibratory compaction, and the Comparison of Theoretical and Experimental Stress Paths. (Chapter 5)

5.Conclusions. (Chapter 6)

Chapter 2

Literature Review

To improve its engineering properties, contractors are generally required to compact the loose soils to increase their unit weights and reducing settlements. Previous studies associated with the compaction-induced effects such as the change of soil density, the change of stresses in the soil mass and mechanism of soils under compaction are discussed in this chapter.

2.1 Earth Pressure At–Rest

2.1.1 Coefficient of Earth Pressure At–Rest

As shown in Fig. 2.1(a), a soil element A located at depth z is compressed by the overburden pressure $\sigma_v = \gamma z$. During the formation of the deposit, the element A is consolidated under the pressure σ_v. The vertical stress induces a lateral deformation against surrounding soils due to the Poisson's ratio effect. Over the geological period, the horizontal strain is kept to be zero and the surrounding soil would develop a lateral stress to counteract the lateral deformation. A stable stress state will develop that the principal stresses acts σ_1 and σ_3 on the vertical and horizontal planes, as shown in Fig. 2.1(b).

The soil in a state of static equilibrium condition is commonly termed as the K_o condition. Donath (1891) defined the ratio of the horizontal stress σ_h to vertical stress σ_v is as the coefficient of earth pressure at-rest, K_o, or

$$K_o = \frac{\sigma_h}{\sigma_v} \qquad (2.1)$$

since $\sigma_v = \gamma z$, then $\sigma_h = K_o \gamma z$, where γ is the unit weight of soil.

For an isotropic soil element shown in Fig. 2.2, if the soil behaved as an ideal elastic material, based on the mechanics of materials, the lateral strain ε_y can be expressed as:

$$\varepsilon_y = \frac{\sigma_y}{E} - \frac{v}{E}(\sigma_x + \sigma_z) \qquad (2.2)$$

or

$$\varepsilon_h = \frac{\sigma_h}{E} - \frac{v}{E}(\sigma_h + \sigma_v) \qquad (2.3)$$

where E is the elastic modulus and v is the Poisson's ratio of the soil.

Base on the definition of the at-rest condition, the lateral strain would be zero ($\varepsilon_h = 0$) under the application of stress state and the $\sigma_h = K_o \sigma_v$. Then the Eq. 2.3 can be written as:

$$\varepsilon_h = \frac{1}{E}(K_o \sigma_v - v K_o \sigma_v - v \sigma_v) = 0 \qquad (2.4)$$

$$K_o = \frac{v}{1-v} \qquad (2.5)$$

It should be mentioned that Eq. 2.5 is applicable for the isotropic and elastic materials only. However, the behavior of soil element is more complex and far from these assumptions. It is evident that the relationship between K_o and elastic parameter, v of Eq. 2.5 is not practical for predicting in-situ horizontal stress.

2.1.2 Jaky's Formula

Several scholars attempted to set up a theoretical relationship between the

strength properties of a soil and K_o. The empirical relationship to estimate K_o of coarse-grained soil is discussed in the following section.

Mesri and Hayat (1993) reported that Jaky (1944) established a relationship between K_o and maximum effective angle of internal friction ϕ by analyzing a talus of granular soil freestanding at the angle of repose. Jaky (1944) supposed that the angle of repose is analogous to the angle of internal friction ϕ. This is reasonable for a sedimentary, normally consolidated material. Jaky (1944) reasoned that the sand cone OAD in Fig. 2.3 is in a state of equilibrium and its surface and inner points are motionless. The horizontal pressure acting on the vertical plane OC is the earth pressure at-rest. Slide planes exist in the inclined sand mass. However, as OC is a line of symmetry, shear stresses can not develop on it. Hence OC is a principal stress trajectory. Based on the equations of equilibrium, Jaky expressed the coefficient of earth pressure at-rest K_o with the angle of internal friction, ϕ :

$$K_o = (1 - \sin\phi)\frac{1 + \frac{2}{3}\sin\phi}{1 + \sin\phi} \qquad (2.6)$$

In 1948, Jaky presented a modified simple expression given by Eq. 2.7.

$$K_o = 1 - \sin\phi \qquad (2.7)$$

Mayne and Kulhawy (1982) reported that, the approximate theoretical relationship for K_o for normally consolidated soils supposed by Jaky appears valid for cohesionless soils. Using Jaky's equation to estimate the in-situ lateral earth pressure is reliable for most engineering purposes.

2.2 Plane Strain Condition

In many soil mechanics problems, a type of state-of-stress that is often encountered is the plane strain condition. Referring to Fig. 2.4, for the strip footing the strain in the y direction at any point P in the soil mass is equal to zero ($\varepsilon_y = 0$). The normal stress σ_y at all sections in the xz plane (i.e., normal to the y axis) are the same, and the shear stresses ($\tau_{yx} = 0, \tau_{yz} = 0$) on these sections are zero. Under a plane-strain state of stress, the normal and shear stresses on the plane normal to the x axis are equal to σ_x and τ_{xz}. Similarly, the normal and shear stress on the plane normal to the z axis are σ_z and τ_{zx}. The relationship between the normal stresses can be expressed as

$$\sigma_y = v(\sigma_x + \sigma_z) \tag{2.8}$$

where v is Poisson's ratio.

2.3 Distribution of Contact Stress over Footings

In calculating the vertical stress σ_z acting between a footing and soil, it is generally assume that the foundation of a structure is flexible and the contact stress σ_x is uniform. The actual nature of the distribution of contact stress will depend on the stiffness of the foundation and the soil on which the nature of the foundation is resting.

In Fig.2.5 (a), when a flexible foundation resting on a cohesionless soil, the distribution of contact pressure will be uniform. However, the maximum settlement will in the center of the foundation.This occus decause the soil located at the edge of foundation lacks lateral confining pressure and hence passesses less strength. In Fig. 2.5(b), a rigid foundation resting on a sand layer

will settle uniformly. The maximum contact pressure will be on the center of foundation.

2.4 Effects of Soil Compaction on Earth Pressure

Compaction of a loose soil can produce a stiff, settlement-free and less permeable mass. It is usually accomplished by mechanical means that cause the density of soil to increase. At the same time the air voids were reduced. It had been realized that the compaction of backfill material has important effects on the earth pressure in the soil mass.

Several theories and analytical methods had been proposed to analyze the residual lateral earth pressures induced by soil compaction. Most of these theories introduced the idea that compaction represented a form of over consolidation, where stresses resulting from a temporary or transient loading condition were retained following the removal of this load.

2.4.1 Study of Broms

Considering placement and compaction of horizontal layers of backfill adjacent to a non-deflection vertical wall, Broms (1971) proposed an analytical procedure based on the concept of hysteretic loading and unloading behavior. The stress path of hysteretic model that Broms' analytical procedure based is shown in Fig. 2.6a. Consideration of a soil element existed at some depth of backfill, the initial horizontal stress state of the element can be illustrated as $\sigma_{hi} = K_o \sigma_{vi}$ which is shown at point A in Fig. 2.6. When the compactor was positioned immediately above the soil element, an increase of the vertical stress results in an increase in horizontal stress on the basis of the assumption of no

lateral yield. The stress state can be expressed as $\sigma_{hm} = K_o\sigma_{vm}$ (point B). As the compactor moves off the fill, a subsequent decrease in vertical effective stress (unloading) results in no lateral stress decrease until a limitation (K_r-line) is reached (point C). The assumption is made that the maximum value of the horizontal stresses induced by compaction sustained until the vertical stress is reduced below a critical value at point C as shown in Fig. 2.6. After that, further unloading results in a decrease in horizontal stress through the stress path as $\sigma_{hf} = K_r\sigma_{vi}$ (point D) until the original vertical stress is reached. K_r is the coefficient of lateral earth pressure ($K_o \leq K_r \leq K_p$, where K_p = coefficient of passive earth pressure). Broms (1971) assumed that K_r equals to $1/K_o$. Compared with the residual horizontal stress, σ_{hf} and initial horizontal stress, σ_{hi} at the same vertical effective stress. It is obviously that the σ_{hf} is much higher than σ_{hi}. The process of soil compaction would result in a higher residual horizontal stress exists.

For a deeper soil element, the vertical stress on the soil element increases under the roller load from A′ to B′, and upon unloading the full maximum horizontal load (σ_{hm}) is retained. Therefore, a critical depth z_c will exist, where the stress state after compaction will return exactly to point C′. The critical depth z_c can be expressed as follows:

$$z_c = \frac{K_o\sigma_{vm}}{\gamma K_r} \tag{2.10}$$

where $\sigma_{vm} = \gamma z + \Delta\sigma_v$, γz is the vertical stress due to the weight of soil, and $\Delta\sigma_v$ is the temporary increase in vertical stress at depth z due to the compactor.

Using the method proposed by Broms to calculate the compaction-induced

earth pressure involves incremental analysis of the stresses resulting from the placement and compaction of each layer of backfill. Compaction at any point is modeled as the application of a transient increase in vertical effective stress ($\Delta\sigma_v$) caused by the compaction vehicle as determined by simple Boussinesq elastic analysis, followed by subsequent removal of the transient vertical load. The horizontal effective stresses due to the transient compaction loading, as well as those due to surcharge increases as a result of fill placement, are then determined by the model shown in Fig. 2.6.

Considering the effect of placing and removing a compactor at the surface of the fill, the distribution of lateral pressure due to compaction proposed by Broms (1971) is shown in Fig. 2.7 (a). Before compaction is applied to the fill, the soil element is under the condition of at-rest, and the horizontal pressure is equal to $K_o\sigma_v$ (curve 1). The application of the compactor leads to an increase in vertical stress which decreases with depth. The maximum horizontal pressure can be calculated with $K_o\sigma_{vm}$, where σ_{vm} equals to $\sigma_v + \Delta\sigma_v$ and $\Delta\sigma_v$ is the increase in vertical stress at any depth due to the compactor (curve 2). As the compactor is removed, the backfill below the critical depth retains the increased horizontal stress and the fill above the critical depth reduces its horizontal stress to $K_r\sigma_v$ (curve 3). Based on the above discussions, as the backfill is compacted at the surface, the profile of the pressure distribution is indicated by the shaded area in Fig. 2.7 (a).

In reality, compaction is carried out regularly on thin layers of fill up the back of the retaining wall. The residual lateral pressure distribution is then given by the locus of the point A as the surface of the fill moves upward. A simplified distribution is illustrated in Fig. 2.7 (b).

2.4.2 Study of Duncan and Seed

Duncan and Seed (1986) presented an analytical procedure for evaluation of peak and residual compaction-induced stresses either in the free field or adjacent to vertical, non-deflecting soil-structure interfaces. This procedure employs a hysteretic K_o -loading model shown in Fig. 2.8. The model is adapted to incremental analytical methods for the evaluation of peak and residual earth pressures resulting from the placement and compaction of soil. When the surcharge is applied on the soil surface, it will increase the vertical stress and the horizontal stress. In Fig. 2.8, as the virgin loading is applied on the soil, both σ_v and σ_h increase along the K_o -line ($K_o = 1\text{-}sin\phi$). Nevertheless, when the surcharge is removed, σ_v and σ_h would decrease along the virgin unloading path. As virgin reloading was applied again, the increment of earth pressure is less than that induced by the first virgin loading.

The hysteretic model may be applied to the analysis of compaction as represented by a transient, moving surficial load of finite lateral extent by directly modeling loading due to increased overburden as an increase in vertical effective stress ($\Delta\sigma'_v$). To model compaction loading in terms of the peak virgin, compaction-induced horizontal stress increase ($\Delta\sigma'_{h,vc,p}$) is defined as the horizontal effective stress which would be induced by the most critical positioning of the compactor. The $\Delta\sigma'_{h,vc,p}$ could be evaluated by the simple elastic analysis if the soil had been previous uncompacted (if the soil had no "lock-in" residual stresses due to previous compaction). While the hysteretic model is applied to the analysis of compaction loading cycle, the $\Delta\sigma'_{h,vc,p}$ should be transformed to an equivalent peak vertical load increment ($\Delta\sigma'_{v,e,p}$) calculated as

$$\Delta\sigma'_{v,e,p} = \frac{\Delta\sigma'_{h,vc,p}}{K_o} \tag{2.11}$$

It is important to note the peak compaction loading must be based on directly

calculated lateral stress increase rather than directly calculated peak vertical stress increase multiplied by K_o, K_a or some other coefficient. Seed and Duncan (1983) concluded that either in the free field, or at or near vertical, nondeflecting soil/structure interfaces, $\Delta\sigma'_{h,vc,p}$ resulting from surficial compaction loading can be calculated directly by simple elastic analysis. The parameter of Poisson's ratio, ν for surficial compaction loading may be chosen according to the empirically derived relationship

$$\nu = \nu_o + \frac{1}{2}(0.5 - \nu_o)$$
(2.12)

where $\nu_o = \dfrac{K_o}{1 + K_o}$

$K_o = 1-sin\phi$

Seed and Duncan (1983) also brought up a simple hand calculation procedure which results in good agreement with the incremental procedure described above. In Fig. 2.9, it is apparent the simple hand solution has a good agreement with the incremental procedure.

2.4.3 Study of Peck and Mesri

Based on the elastic analysis, Peck and Mesri (1987) presented a calculation method to evaluate the compaction-induced earth pressure. The lateral pressure profile can be determined by four conditions on σ_h, as illustrated in Fig. 2.10 and summarized in the following.

1. Lateral pressure resulting from the overburden of the compacted backfill,

$$\sigma_h = (1 - \sin\phi)\gamma z$$
(2.13)

12

2. Lateral pressure limited by passive failure condition,

$$\sigma_h = \tan^2(45 + \phi/2)\gamma z \qquad (2.14)$$

3. Lateral pressure resulting from backfill overburden plus the residual horizontal stresses,

$$\sigma_h = (1 - \sin\phi)\gamma z + \frac{1}{4}(5^{1.2\sin\phi} - 1)\Delta\sigma_h \qquad (2.15)$$

where $\Delta\sigma_h$ is the lateral earth pressure increase resulted from the surface compaction loading of the last backfill lift and can be determined based on the elastic solution.

4. Lateral pressure profile defined by a line which envelops the residual lateral pressures resulting from the compaction of individual backfill lifts. This line can be computed by Eq. 2.16.

$$\frac{\Delta\sigma_h}{\Delta z} = \frac{1 - \sin\phi}{4}(5 - 5^{1.2\sin\phi})\gamma \qquad (2.16)$$

Fig. 2.10 indicates that near the surface of backfill, from point a to b, the lateral pressure on the wall is subject to the passive failure condition. From b to c, the overburden and compaction-induced lateral pressure profile is determined by Eq. 2.15. From c the lateral pressure increases with depth according to Eq. 2.16 until point d is reached. Below d, the overburden pressure exceeds the peak increase in stress by compaction. In the lower part of the backfill, the lateral pressure is directly related to the effective overburden pressure.

2.4.4 Study of Chen and Fang

Chen and Fang (2008) reported some experiments in nonyielding retaining wall at National Chiao Tung University to investigate influence of earth pressure due to vibratory compaction. Air-dry Ottawa sand was used as backfill material. Vertical and horizontal stresses in the soil mass were measured in loose sand and compacted sand. Based on his test results, Chen and Fang (2008) proposed the following conclusions: (1) after compaction, the lateral stress measured near the top of backfill is almost identical to the passive earth pressure estimated with Rankine theory. The compaction-influenced zone rises with rising compaction surface. Below the compaction-influenced zone, the horizontal stresses converge to the earth pressure at-rest, as indicated in Fig. 2.11 and Fig.2.12; (2) when total (static + dynamic) loading due to the vibratory compacting equipment exceeds the bearing capacity of foundation soils, the mechanism of vibratory compaction on soil can be described with the bearing capacity failure of foundation soils; (3) the vibratory compaction on top of the backfill transmits elastic waves through soil elements continuously. For soils below the compaction-influenced zone, soil particles are vibrated. The passive state of stress among particles is disturbed. The horizontal stresses among soil particles readjust under the application of a uniform overburden pressure and constrained lateral deformation, and eventually converge to the at-rest state of stress.

Chen's test results were compared with the design recommendations proposed by NAVFAC DM-7.2 (1982), Duncan and Seed (1986), Peck and Mesri (1987), and Duncan et al. (1991) as shown in Fig. 2.13. Parameter values used in the stress calculation including the unit weight γ, relative D_r, internal friction angle ϕ, wall friction angle δ, and cyclic compaction stress σ_{cyc} are shown in Fig. 2.13. The horizontal pressure distribution suggested by the Navy Design Manual DM-7.2 was based on the analytical method proposed by Ingold (1979). The pressure distribution calculated with the method proposed by Duncan et al. (1991) was obtained from the

design chart for vibratory plates with a cyclic compaction stress $q = 34.9$ kN/m^2 (5 psi).

In Fig. 2.13, Chen's test data are in good agreement with the proposed design methods. The horizontal stresses in the uppermost compacted lift are equal to or slightly less than the passive Rankine pressure. However, at a lower depth, the Chen's test data are apparently lower than the calculated horizontal stresses. It is important that the application of Chen's test findings are limited to estimating the horizontal stresses acting on a nonyielding wall induced by a small size vibratory hand tamper.

Chapter 3

Experimental Apparatus

To investigate the effects of vibratory compaction on the vertical stress σ_v and horizontal stress σ_h in a cohesionless soil mass, the instrumented non-yielding model retaining wall facility at National Chiao Tung University (NCTU) was used. This chapter introduced the NCTU non-yielding retaining wall facility and the vibratory compactor. Chen and Fang (2008) described the facility consist of three components: (1) model retaining wall; (2) soil bin; and (3) data acquisition system. The details of the foregoing apparatuses are described in the following sections.

3.1 Model Retaining Wall

The model wall shown in Fig. 3.1 is 1,500 mm-wide, 1,600 mm-high, and 45 mm-thick. To achieve an at-rest condition, the wall material should be nearly rigid. It is hoped that the deformation of the model wall could be neglected with the application of earth pressure. As indicated in Fig. 3.1, twenty-four 20 mm-thick steel columns were welded to the four sidewalls to reduce any lateral deformation during loading. In addition, twelve C-shaped steel beams were also welded horizontally around the box to further increase the stiffness of the box.

3.2 Soil Bin

To simulate a plane strain condition for model test, the soil bin is designed to minimize the lateral deflection of sidewalls. In Fig. 3.1, the soil bin was fabricated of steel plates with inside dimensions of 1,500 mm ×1,500 mm ×1,600 mm.

Assuming a 1,500 mm-thick cohesionless backfill with a unit weight $\gamma = 17.1$ kN/m^3, and an internal friction angle $\phi = 41°$ was pluviated into the soil bin. A 45 mm-thick solid steel plate with a Young's modulus of 210 GPa was chosen as the wall material. The estimated deflection of the model wall would be only 1.22×10^{-3} mm. Therefore, it can be concluded that the lateral movement of the model wall is negligible and an at-rest condition can be achieved.

The end-wall and sidewalls of the soil bin were made of 35 mm-thick steel plates. Outside the steel walls, vertical steel columns and horizontal steel beams were welded to increase the stiffness of the end-wall and sidewalls. If the soil bin was filled with dense sand, the estimated maximum deflection of the sidewall would be 1.86×10^{-3} mm. From a practical point of view, the deflection of the four walls around the soil bin can be neglected.

To investigate the distribution of horizontal earth pressure σ_h, soil pressure transducers (SPT) were attached to the model wall as illustrated in Fig. 3.2. Fifteen strain-gage-type transducers (Kyowa PGM-02KG, capacity = 19.62 kN/m^2) were arranged within the central zone of the wall. The soil pressure transducer with the adapter is shown in Fig. 3.3. The diameter of the SPT sensing area is 12 mm. To investigate the development of vertical stress σ_v in the backfill, another series of soil pressure transducers (Kyowa BE-2KCM17, capacity = 98.1 kN/m^2) were arranged behind the model wall. The transducers were used to measure the variation of vertical earth pressure σ_v during the filling and compaction process. The soil pressure transducer buried in the backfill is shown in Fig. 3.4. The diameter of the SPT sensing area is 22 mm.

3.3 Data Acquisition System

A data acquisition system was used to collect and store the considerable amount of data generated during the tests. In the Fig. 3.5, the data acquisition system is composed of the following four parts: (1) dynamic strain amplifiers (Kyowa: DPM601A and DPM711B); (2) AD/DA card (NI BNC-2090); and (3) Personal

Computer. The analog signals from the sensors were filtered and amplified by the dynamic strain amplifiers. Then, the analog experimental data were digitized by an A/D-D/A card. The digital signals were then transmitted to the personal computer for storage and analysis.

3.4 Vibratory Compactor

To simulate compaction of backfill in the field, the vibratory compactor shown in Fig. 3.6 and Fig.3.7 was made by attaching an eccentric motor (Mikasa Sangyo, KJ75-2P) to a 225 mm ×225 mm steel plate. The mass of the vibratory compactor is 12.1 kg. Fig. 3.8 shows that the eccentric force can be controlled by adjusting the number of eccentric steel plates attached to the rotating shaft of motor. For this study, a total of sixteen eccentric plates (8+8) were used. The technical information regarding the eccentric motor is listed in Table 3.1. It should be mentioned that the distribution of contact pressure between the foundation and soil varies with the stiffness of the footing. If the footing is perfectly rigid, the static contact pressure on the footing increases from zero at the edge to a maximum at the center.

Chapter 4

Backfill and Interface Characteristics

The characteristics of the backfill, and the side wall friction are introduced in this chapter.

4.1 Backfill Properties

Air-dry Ottawa silica sand (ASTM C-778) was used as the backfill material in all experiments. Physical properties of the soil were summarized in Table 4.1. Grain-size distribution of the backfill is shown in Fig. 4.1. The major reasons to select Ottawa sand as the backfill material are listed below.

1. Its round shape, which avoids the effect of angularity of soil grains.

2. Its uniform distribution of grain size (coefficient of uniformity C_u = 1.5), which avoids the effects due to soil gradation.

3. High rigidity of solid grains, which reduces possible disintegration of soil particles under loading.

4. Its high permeability, which allows fast drainage and therefore reduces water pressure behind the wall.

To establish the relationship between unit weight of backfill γ and its internal friction angle ϕ, direct shear tests have been conducted. The shear box used has a square (60 mm × 60 mm) cross-section, and its testing arrangement is shown in Fig. 4.2. Before shearing, Ottawa sand was air-pluviated into the shear box and then compacted to the desired density.

Chang (2000) established the relationship between the internal friction angle ϕ and unit weight γ of Ottawa sand as shown in Fig. 4.3. It is obvious in the figure that soil strength increases with increasing soil density. For the air-pluviated backfill, the empirical relationship between soil unit weight γ and ϕ angle can be formulated as follows

$$\phi = 6.43\,\gamma - 68.99 \qquad (4.1)$$

where

ϕ = angle of internal friction of soil (degree)

γ = unit weight of soil (kN/m^3)

Eq. (4.1) is applicable for $\gamma = 15.45 \sim 17.4$ kN/m^3 only.

For compacted backfill, the following relationship can be formulated.

$$\phi = 7.25\,\gamma - 79.51 \qquad (4.2)$$

Eq. (4.2) is applicable for $\gamma = 15.8 \sim 17.05$ kN/m^3 only.

4.2 Side wall Friction

To constitute a plane strain condition for model wall tests, the shear stress between the backfill and the side walls should be minimized to nearly frictionless. To reduce the friction between side wall and backfill, a lubrication layer fabricated with plastic sheets was furnished for all experiments. Two types of plastic sheeting, one thick and two thin plastic sheets, were adopted to reduce the interface friction. All plastic sheets were hung vertically on the side walls before the backfill was deposited as shown in Fig. 4.4.

Multiple layers of thin plastic sheets (without any lubricant) were used by McElroy (1997) for shaking table tests of geosynthetic reinforced soil (GRS) slopes. Burgess (1999) used three thin plastic sheets to reduce side wall friction in full-scale GRS wall tests. The wall friction angle was approximately 15° as

determined by the shear box tests. In this study, two thin (0.009 mm-thick) and one thick (0.152 mm-thick) plastic sheets were adopted for the earth pressure experiments. The friction angle developed between the plastic sheets and steel sidewall could be determined by the sliding block test. A schematic diagram and a photograph of the sliding block test proposed by Fang et al. (2004) are illustrated in Fig. 4.5. and Fig. 4.6. The side wall friction angle δ_{sw} for the sliding block test was determined using the basic principles of physics.

As the inclination of the plate is increased, based on the equilibrium of forces, the sliding resistance T also increases until the driving force overcomes the resistance and the soil box starts to move. At this moment, the inclination angle of the plate to the horizontal is the interface friction angle δ that represents the characteristics of the lubrication layers. Fig. 4.7. shows the variation of side-wall friction angle δ_{sw} as a function of the normal stress σ_n for the plastic sheet method (1 thick + 2 thin sheeting) used in this study. The measured side-wall friction angle with this method is about 7.5°. It is clear in Fig.4.8. that the wall friction angle δ_{sw} is nearly independent of the applied normal stress σ_n. This constancy is an important advantage in establishing the input soil properties for analytical models that might be used to analyze the experimental results. For all experiments in this paper, the lubrication layers were wall applied o two side walls as indicated in Fig. 4.4. The plastic sheets not only can help to reduce the friction force between the side walls and the backfill, but also can help to reduce the reflection of elastic waves transmitted to the soil-wall boundaries during compaction.

4.3 Control of Soil Density

4.3.1 Air-Pluviated loose Ottawa Sand

To achieve a uniform soil density in the backfill, Ottawa sand was deposited by air-pluviation method into the soil bin. The air-pluviation method had been widely used for a long period of time to reconstitute laboratory sand specimens. Rad and Tumay (1987) reported that pluviation is the method that provides reasonably homogeneous specimens with desired relative density. Lo Presti et al. (1992) reported that the pluviation method could be performed for greater specimens in less time.

Das (1994) suggested that relative densities of 15~50%, and 70~85% are defined as loose and dense condition, respectively. Ho (1999) established the relationship among slot opening, drop height, and density as shown in Fig. 4.8.To achieve a loose backfill (D_r = 32%), Chen (2003) adopted the drop height of 1 m and hopper slot opening of 15 mm. In this study, to reduce the disturbance due to soil drooping, the drop height of 0.5 m and the hopper slot-opening of 10 mm were selected to achieve the loose backfill. In Fig. 4.9 shows, the soil hopper that let the sand flow through a calibrated slot opening at the lower end. A picture of the soil pluviating processes is shown in Fig. 4.10.

4.3.2 Compacted Dense Sand

To simulate the backfill compacted in the field, the loose backfill was placed in five lifts. Each lift was pluviated into the soil bin, carefully leveled, then compacted with a vibratory compactor shown in Fig.3.7. As indicated in Fig. 4.11, the soil surface was divided into six lanes parallel to the face of the model wall, and each lane was compacted with the vibratory compactor with a pass of 70 seconds. Each compacted lift has a thickness of 0.3 m.

4.3.3 Uniformity of Soil Density

To observe the distribution of soil density in the soil bin, the soil density cups were made. The soil density control cup made of acrylic is illustrated in Fig. 4.12. and Fig. 4.13. During the preparation of soil specimen, density cups were buried in the soil mass at different elevations and different locations in the backfill as shown in Fig. 4.14 and Fig. 4.15. After the soil had been filled up to 1.5 m from the bottom of the soil bin, soil density cups were dug out from the soil mass carefully. Fig. 4.16(a) shows the density cup was placed in the soil bin at desired locationand Fig. 4.16(b) shows the mass of the cup and soil in the cap was measured with an electrical scale. The distribution of soil density with depth for sand is shown in Fig. 4.17. For the air-pluviated loose sand, the mean unit weight γ is 15.6 kN/m^2, the mean relative density is D_r = 34.2 % with the standard deviation of 2.3%. For the compacted dense sand, the mean unit weight γ is 16.6 kN/m^2, the mean relative density is about 73.8 % with the standard deviation of 2.68 %. Das (1994) suggested that for the relative density 15 % $\leq D_r \leq$ 50 % is defined as loose sand, while 70 % $\leq D_r \leq$ 85 % is defined as dense sand.

Chapter 5

Test Results and Discussion

This chapter reported experimental results regarding the vertical and horizontal earth pressures in air-pluviated loose sand and vibratory compacted dense sand. The stress path during compaction was carefully investigated. Based on the experimental evidence, a rational mechanism of vibratory compaction on cohesionless soil is proposed. For all experiments, the surface of backfill was finally horizontal and the backfill was filled up to 1.5 m above the base of the model wall.

5.1 Stresses in loose sand

For comparison purposes, at the beginning of this study, experiments were conducted to investigate the stresses in an uncompacted loose backfill. The method of air-pluviation was adopted to prepare the backfill and the relative density Dr achieved for the loose sand was 34.2 %. Fig. 5.1 illustrated stress σ_v showed the location of soil pressure transducers to measure the distribution of vertical and horizontal earth pressure σ_h with depth. SPT102, SPT105, SPT108, SPT111, and SPT114 were buried in the soil mass to measure σ_v. The vertical earth pressure σ_v measured in the soil mass was illustrated in Fig. 5.2 (a). In this figure, the vertical pressure σ_v increased linearly with increasing depth z and the test data were in fairly good agreement with the traditional equation $\sigma_v = \gamma z$. In this study, unit weight γ was 15.6 kN/m^3 for the loose sand. The distribution of horizontal earth pressure σ_h with depth was illustrated in Fig. 5.2(b). In the figure, the earth pressure profile induced by the 1.5 m-thick loose backfill was

approximately linear and was in good agreement with the Jaky's equation. Mayne and Kulhawy (1982), Mesri and Hayat (1993) reported that Jaky's equation was suitable for backfill in its loosest state. From a practical point of view, it was concluded that for a loose backfill, the vertical and horizontal earth pressure in the soil mass can be properly estimated with the equation $\sigma_v = \gamma z$ and Jaky's equation, respectively.

5.2 Dynamic Behavior of the Soil compactor

The vibratory compactor was made by attaching an electric motor (Mikasa Sangyo, KJ75-2P) to a steel plate as shown in Fig. 5.4. For investigating the variation of earth pressure in the compacted sand, it was necessary to measure the forces applied to the sand by vibratory compactor. Fig. 3.8 showed the definition of x-y-z axes for this study. The photograph of the accelerometer is shown in Fig. 5.3. In the Fig. 5.4, the accelerometer was attached to the compactor to measure its acceleration in x-direction a_x. The measured acceleration in x-direction with time is illustrated in Fig. 5.5(a). In the figure, the maximum acceleration a_x was about $\pm$ 23.1 m/s^2. The mass of the compactor was 12.1 kg. Since F = ma, the maximum force in the x-direction shown if Fig. 5.5(b) F_x was $\pm$ 280 N.

In the Fig. 5.6, the accelerometer was attached to the compactor to measure its acceleration in the y-direction. Fig. 5.7(a) showed the maximum acceleration in y-direction a_y was about $\pm$ 100.3 m/s^2. Fig. 5.7(b) showed the maximum force in y-direction F_y was $\pm$ 1320 N.

In the Fig. 5.8, the accelerometer was attached to the compactor to measure the acceleration in z-direction. Fig. 5.9 showed the maximum acceleration in z-direction a_z was about $\pm$ 140.37 m/s^2. Fig. 5.9(b) showed the maximum dynamic force was $\pm$ 1690 N. In Fig. 5.5, 5.7 and 5.9, the acceleration a_z ($\pm$ 140.37 m/s) and a_y ($\pm$ 100.3 m/s) was much stronger than a_x ($\pm$ 23.1 m/s). It may be observed in Fig. 3.8 that x-axis was the center of rotation of the eccentric plates. The eccentric force

was generated mainly in y and z (vertical)direction.

F_z is the vertical force the vibratory compactor applied on the soil surface. The F_z included the static dead load of the compactor W and the dynamic vertical force $F_{z,dynamic}$.

$$F_z = W \pm F_{z,dynamic} \qquad (5.1)$$

Where $W = mg = 12.1 \text{ kg} \times 9.81 \text{ m/s}^2 = 119$ N. It should be mentioned that only positive force (compression) can be applied at the soil-compactor interface as shown in Fig 5.9(b). As a result, in Fig. 5.10, the total force (static + dynamic) F_z was about 1819 N. Assuming the distribution of contact pressure between the base plate (0.225 m × 0.225 m) and soil is uniform, the peak cyclic vertical stress σ_z applied on the surface of soil would be about 35750 N/m².

5.3 Vertical and Horizontal Stresses in Sand during Compaction

To obtain the expected dense condition, the loose backfill was placed and compacted in five lifts as shown in Fig. 5.1. Each lift in Fig. 4.11 was divided into six lanes, and each 1.5 m long lane was compacted with the vibratory compactor for 70 seconds. Fig. 5.11 showed the vertical pressure σ_v profile after the vibratory compaction. In the figure, the measured vertical stresses increased with increasing depth. It is clear in the figure that the vertical overburden pressure σ_v can be properly estimated with the equation $\sigma_v = \gamma z$. As compared with the σ_v for loose sand, σ_v measured in dense sand was slightly greater because the compacted backfill had a slightly higher unit weight. It is clear in the figure that the compaction process did not result in significant residual stress in the vertical direction. It may be concluded that the effect of vibratory compaction on the vertical pressure σ_v was insignificantly.

The distributions of horizontal earth pressure against the nonyielding wall after the compaction of soil from lift 1 to lift 5 were shown in Fig. 5.12 (a) to (e). The test results reported by Chen and Fang (2008) were also plotted in Fig. 5.12. Each compacted lift is 0.3 m-thick after compaction. The variation of lateral earth pressure was monitored by the soil pressure transducer mounted on the wall. Before compaction, the earth pressure at-rest can be properly estimated with Jaky's equation. However, after vibratory compaction, it is clear in Fig. 5.12 (d) that an extra horizontal stress $\Delta\sigma_{h,ci}$ was induced by compaction. The compaction-influenced zone indicated in Fig. 5.12 (d) extended from the compacted surface to the depth of approximately 0.7 m. In Fig. 5.12 (c) to (e), the compaction-influenced zone rose with rising compaction surface. It was interesting to note in Fig. 5.12 (e) that, below the compaction-influenced zone the horizontal stresses converged to the earth pressure at-rest based on Jaky's equation. The lateral stress measured near the top of backfill was almost identical to the passive earth pressure estimated with Rankine theory. It should be emphasized that the influence of vibratory compaction on the horizontal earth pressure σ_h in the soil mass was quite significant.

5.4 Stress Paths for Filling and Compaction of Backfill

The stress path (σ_v versus σ_h) for a soil element under the filling and compaction of the backfill for Test 0812 was shown in Fig. 5.13. Chen and Fang (2008) reported that the compaction process would not result in residual stress in the vertical direction. On the other hand, horizontal earth pressure near the top of the wall increased significantly due to compaction. The test data shown in Fig. 5.13 (a) to (e) were measured by SPT2, SPT5, SPT8, SPT11, and SPT14 respectively. In Fig. 5.13, the stress path F represented the stress variation due to the filling of the 0.3 m-thick Ottawa sand. Stress path C represents the stress variation due to the vibratory compaction on the surface of the lift. From these figures, it was clear in

Fig. 5.13(a) that at SPT2, compaction of lift1 caused the σ_h to increase as shown in stress path C1. The compaction of lift 3 to lift 5 gradually brought the σ_h back to an at-rest stress condition indicated by the K_0-line. The Rankine passive pressure (K_p-line) was apparently the upper bound of the induced lateral earth pressure. The path C2 in Fig. 5.13(b), path C3 in Fig. 5.13(c), path C4 in Fig. 5.13(d), and path C5 in Fig. 5.13(e) indicated that the variation of lateral stress was mainly caused by the compaction of backfill near the pressure-transducer, not soil filling. Based on the test results of Test 0804. 0805, 0806, 0810, similar stress variation of stress path could be shown in Fig. 5.14. It appeared the test results were quite reproducible.

5.5 Dynamic Stress Paths during Compaction

The dynamic stress paths (σ_h vs. σ_v) due to vibratory compaction were investigated in this study based on soil pressure transducer measurements. In Fig. 5.13(a) the stress path F1 represented the stress path due to the Filling of Lift 1. The F1 stress path basically followed the K_0-line as expected. The stress path C1 represented the Compacting of Lift 1. It should be mentioned that the loose backfill was placed and compacted in five Lifts, from Lift 1 to Lift 5 as shown in Fig. 5.15(d). Each compacted lift had a thickness of 0.3 m.

In Fig. 5.15(a) showed the soil surface of each lift was divided into six lanes parallel to the face of the model wall. Lane f compacted first and Lane a was compacted last. Each lane was densified with a pass having duration of 70 seconds.

In Fig. 5.13(a), the stress path C1 was approximated with a straight lone. However the dynamic stress path from point A to point B was much more complicated than a straight line. As illustrated in Fig. 5.15, the dynamic stress paths in the sandy backfills were discussed in three conditions: (1) compaction approaching SPT in x-direction; (2) compaction passing SPT in y-direction; and (3) compaction rising in z-direction.

5.5.1 Compaction Approaching SPT in x-direction

Fig. 5.16 showed the dynamic stress paths due to compaction of Lift 1 from lane f to lane a. Each lane was compacted with a pass of 70 seconds. To avoid confusion due the large amount of test data obtained, only the dynamic stress path measured from t = 34.5 to 35.5 s (duration = 1 second) was plotted in Fig. 5.16. In Fig. 5.16(a) the legend C1-f-center represented the Compaction of Lift 1 , on Lane f, at the center part of the lane. In this figure, the horizontal stress σ_h and vertical stress σ_v were measure by SPT2 and SPT102, respectively, as illustrated in Fig. 5.1. Since Lane f was about horizontally 1.25 m away from the SPT, the dynamic stress path illustrated in Fig. 5.16(a) was insignificant. As the vibratory compactor moved from Lane f towed Lane a, the compaction-induced stresses increased.

In Fig. 5.16(f), the dynamic stress path due to the 1-second compaction on Lift 1 at the center part of Lane a was quite apparent. The stress paths were bounded by the at-rest k_0-line and passive k_p-line. The shape of the stress path was quite different from the stress paths proposed by Broms(1971), and Duncan and Seed(1986).

The dynamic stress path due to the compaction on Lift 2, 3, 4, and 5 were illustrated in Fig/ 5.17, 5.18, 5.19 and 5.20, respectively. In three figures, with the approaching of compaction toward the earth pressure transducers , the stress paths became more significant. No stress beyond the k_p-line had been observed in the experiments.

5.5.2 Compaction Passing SPT in y-direction

The stress paths due to the compaction on Lane a of　Lift 1 were shown in Fig. 5.21. As illustrated in Fig. 5.15(b), only the stress path due to the 1-second compaction at: (1) Center-R750; (2) Center-R375; (3) Center; (4)

Center-L375; and (5) Center-L750 were reported. Center-R750 represented a location 750 mm to the right of the centerline of the model wall.

In Fig. 5.21(a), the measured stress path was not obvious, because the point of compaction was 750 mm to the right of SPT2 and SPT102. As the compaction moved toward the SPT in y-direction, the stress path became move apparent in Fig. 5.21(b). In Fig. 5.21(c), the compaction-induced stresses were most significant. The stress path was definitely not a straight line. As the point of compaction passed and moved away from the SPT, the effects compaction became less obvious.

The dynamic stress path due to the passing of compactor on Lane a of Lift 2, 3, 4 and 5 were indicated in Fig. 5.22, 5.23, 5.24 and 5.25, respectively. In three figures, as the compactor moved toward the SPT in y-direction, the stress paths became more apparent. No stress below the K0-line had been observed.

5.5.3 Compaction Rising in z-direction

Fig. 5.26 showed the dynamic stress paths measured at SPT2 and SPT102 due to compaction on the center part of Lane a of Lift 1 to Lift 5. In Fig. 5.26(a), since the vibratory compaction was only about 0.15 m right above the pressure transducers, the compaction-induced stress path was quite obvious. In Fig. 5.26(b), (c) and (d), the thickness of the overburden soil increased, and the compaction induced stress path became less significant. In Fig. 5.26(d), the compaction of Lift 5 draged the stress path to a point below the K_0-line. The stress paths due to compaction measured with SPT5 and SPT105, SPT8 and SPT108, SPT11 and SPT111, and SPT14 and SPT114 were shown in Fig. 5.27, 5.28, 5.29 and 5.30 respectively In Fig. 5.28(b), the 1-second dynamic stress path due to the compaction on the center part of Lane of Lift 4 was beyond the C4 stress path. It is possible

that the dynamic stress path may not be restrained and described by the simplified straight-line stress path

5.6 Comparison among Lifts and Tests

Fig. 5.31(a) to (e) showed the stress paths due to the 1-second compaction at the center of Lane a for Lift 1 to Lift 5. It was observed in these figures that the shape and the size of the dynamic stress paths obtained at five different lifts were quite similar. The dynamic stress path had the shape of a comet. The comet moved between the K_0-line and K_f-line. Fig. 5.32 showed similar experimental results were obtained from Test 0805.

5.7 Comparison of Theoretical and Experimental Stress Paths

Fig. 5.33 showed the theoretical stress path of hysteretic model proposed by Broms (1971). For a soil element existed at some depth of backfill, the initial vertical stress due to the overburden soil was σ_{vi}. The initial horizontal stress was $\sigma_{hi} = K_0 \sigma_{vi}$, which was represented by the point A in Fig. 5.33. When a heavy compactor was positioned immediately above the soil element, following the K_0-line, an increase of the vertical stress resulted in an horizontal stress increase based on the assumption of no lateral yield. The stress state can be expressed as $\sigma_{hm} = K_0 \sigma_{vm}$ (point B). As the heavy compactor moved off the fill, a subsequent decrease in σ_v (unloading) resulted in no σ_h decrease until a limitation (K_r-line) was reached (point C). the assumption was made that the maximum horizontal stress induced by compaction σ_{hm} sustained until the vertical stress is reduced below a critical value at point c. After that, further σ_v unloading resulted in a decrease in σ_h following the K_r-line as $\sigma_{hf} = K_r \sigma_{vi}$ (point D) until the original

vertical stress σ_{vi} was reached. Broms (1971) assumed that $K_r = 1/K_0$.

The experiment stress paths due to the filling of backfill of Lift 2 (F2) and the compaction of Lift 2 (C2) were shown in Fig. 5.33. It is interesting to note that the starting point A and ending point D lased on Brown's theory, was similar to the starting point A and ending point E of the stress path C2. It was indicated that compaction would result in an increase of stress only in the horizontal direction, but not in the vertical direction.

The dynamic stress path due to on-cycle of compaction at the center part of Lane A was also illustrated in Fig. 5.33. It was obvious that the comet-shaped dynamic stress path was quite different from the stress path proposed by Broms. It should be mentioned that the stress path AB in Fig. 5.33 indicated the heavy compactor generally 5~15 ton applied a large static vertical pressure σ_v on the surface of fill. However, stress path BC represented the removal of the heavy compactor. The mass of hand-operated square-plate compactor used in this study was only 12.1 kg (W= 119 N). Fig. 5.9 showed the peak dynamic force applied on the surface of fill was $F_x = \pm 280$ N, $F_y = \pm 1320$ N, and $F_Z = 1690$ N. The vibratory compaction was 3-dimentional and was controlled by the cyclic loading instead of the dead-load of the compactor. This was probably the main reason why the dynamic stress path due to vibratory compaction was so different from Broms' finding.

Chapter 6

CONCLUSIONS

This paper studied variation of earth pressure and dynamic stress path in compacted sand. Based on the experiment results, the following conclusions were drawn.

1. For a loose backfill, the horizontal earth pressure in the soil mass was in good agreement with Jaky's solutions. The vertical earth pressure in soil was near to the equation $\sigma_v = \gamma z$.

2. After compaction, the lateral stress measured near the top was almost identical to the passive earth pressure estimated with Rankine theory. The effect of vibratory compactiom on the vertical pressure was insignificant.

3. After compaction, the thickness of the compaction-influenced zone rose with the elevation of the compaction surface. Below the compaction-influenced zone, the horizontal stresses converged to the earth pressure at-rest based on Jaky's equation.

4. As the area of the compaction approached the soil pressure transducer (SPT) in x-direction (perpendicular to the wall face), the dynamic stress path became more obvious when the compactor moved to the lane near the wall.

5. As the area of compaction passed the SPT in y-direction (parallel to the wall surface), the maximum dynamic stress path was obvious when the compactor was right in front of the SPT.

6. For a SPT at a lower elevation, when the area of compaction rose with the elevation of the lift surface, the compaction-induced stress path became less significant.

7. The dynamic stress path of a soil element under vibratory compaction had the shape of a comet. The shape size of the dynamic stress paths obtained at five different lifts was quite similar. The stress paths were bounded by the at-rest K_0-line and passive K_p-line.

8. The measured dynamic stress path was quite different from the stress path proposed by Broms (1971). The stress path reported by Broms was induced by a static heavy compactor. The vibratory compactor used in this study vibrated and generated cycle force in three direction: F_x, F_y, and F_z. This was probably the main reason why the dynamic stress path due to vibratory compaction was so different from Broms' finding.

References

1. Borowicka, H., Influence of Rigidity of a Circular Foundation Slab on the Distribution of Pressures over the Contact Surface, *Proc. 1ˢᵗ Int. Conf. Soil Mech. Found. Eng.*, vol. 2, pp. 144-149, 1936.

2. Borowicka, H., The Distribution of Pressure under a Uniformly Loaded Elastic Strip Resting on Elastic-Isotropic Ground, *2d Cong. Int. Aaaoc. Bridge Struct. Eng., Berlin, Final report*, vol. 8, no. 3, 1938.

3. Broms, B. (1971). "Lateral earth pressures due to compaction of cohesionless soils." Proc., 4th Int. Conf. Soil Mech., Budapest, 373-384.

4. Burgess, G. P. (1999). "Performance of Two Full-scale Model Geosynthetic Reinforced Segmental Retaining Walls," MS thesis, Royal Military College of Canada, Kingston, Ontario, 207.

5. Chang, S. Y. (2000). "Effects of Backfill Density on Active Earth Pressure." MS thesis, Dept. of Civil Engineering, National Chiao Tung University, Hsinchu, Taiwan.

6. Chen, T. J., and Fang, Y. S, (2002). "A New Facility For Measurement of Earth Pressure At-Rest," *Geotechnical Engineering Journal*, SEAGS, 3(12), 153-159.

7. Chen, T. J., (2003). "Earth Pressure Due to Vibratory Compaction", Doctor of Philosophy Dissertation, National Chiao Tung University, Hsinchu, Taiwan.

8. Chen, T. J., and Fang, Y. S, (2008). "Earth Pressure Due to Vibratory Compaction", *Journal of Geotechnical and Geoenvironmental Engineering*, ASCE, 134(4), 1-8.

9. D'Appolonia, D. J., Whitman, R. V., and D'Appolonia, E. (1969). "Sand Compaction with Vibratory Rollers." *Journal of the Soil Mechanics and Foundations Division*, ASCE, 95(SM1), 263-284.

10. Das, B. M., (1994), "Principal of Geotechnical Engineering. " 3ʳᵈ Edition, PWS Publishing Company, Boston.

11. Donath, A. D. (1891). "Untersuchungen veber den erddruck auf

stuetzwaende." *Zeitschrift fuer Bauwesen*, Berlin.

12. Duncan, J. M., and Seed, R. B. (1986). "Compaction-induced Earth Pressures under K_o-conditions." *Journal of Geotechnical Engineering*, ASCE, 112(1), 1-22.

13. Duncan, J. M., Williams, G. W., Sehn, A. L., and Seed, R. B. (1991). "Estimation earth pressures due to compaction." *Journal of Geotechnical Engineering*, ASCE, 117(12), 1833-1847.

14. Fang, Y. S. (1983). "Dynamic earth pressures against rotating walls." Ph.D. dissertation, Department of Civil Engineering, University of Washington, Seattle, Washington.

15. Fang, Y. S., Chen, T. J., Holtz, R. D., and Lee, W. F., (2004). "Reduction of Boundary Friction in Model Tests", *Geotechnical Testing Journal*, ASTM, 27(1), 1-10.

16. Filz, G. M., and Duncan J. M. "Earth Pressures due to Compaction: Comparison of Theory with Laboratory and Field Behavior." *Transportation research record*, 1526, 28-37.

17. Ho, Y. C., (1999). "Effects of Backfill Compaction on Passive Earth Pressure." MS thesis, Dept. of Civil Engineering, National Chiao Tung University, Hsinchu, Taiwan.

18. Ingold, T. S. (1979). "Retaining wall performance during backfilling." *Journal of the Geotechnical Engineering Division*, ASCE, 105(GT5), 613-626.

19. Ingold, T. S. (1979). "The effects of compaction on retaining walls." *Geotechnique*, 29(3), 265-283.

20. Jaky, J. (1944). "The Coefficient of Earth Pressure at rest." *Journal for Society of Hungarian Architects and Engineers*, Budapest, Hungary, Oct., 355-358.

21. Jaky, J., (1948), "Pressure in Soils," *Proceedings, 2nd International Conference on Soil Mechanics and Foundation Engineering*, 1, 103-107.

22. Johnson, A. W., and Sallberg, J. R. (1960). " Factors That Influence Field Compaction of Soil." Highway Research Board, *Bulletin* No. 272.

23. Lo Presti, D. C. F., Pedroni, S., and Crippa, V. (1992). "Maximum Dry Density of Cohesionless Soils by Pluviation and by ASTM D 4253-83: A comparative study." *Geotechnical Testing Journal*, ASTM, 15(2), 180-189.

24. Mayne, P. W., and Kulhawy, F. H. (1982). "K_o-OCR Relationships in Soil." *Journal of Geotechnical Engineering Division*, ASCE, 108(GT6), 851-872.

25. McElroy, J. A. (1997). "Seismic Stability of Geosynthetic Reinforced Slopes: A shaking table study." MS thesis, University of Washington, Seattle, 286.

26. Mesri, G., and Hayat, T. M. (1993). "The Coefficient of Earth Pressure at rest." *Canadian Geotechnical Journal*, 30(4), 647-666.

27. Peck, R. B., and Mesri, G. (1987). Discussion of "Compacted-induced earth pressures under K_o-conditions." *Journal of Geotechnical Engineering*, ASCE, 113(11), 1406-1408.

28. Rad, N. S., and Tumay, M. T. (1987). "Factors affecting sand specimen preparation by raining." *ASTM Geotechnical Testing Journal*, 10(1), 31-37.

29. Seed, R. B., and Duncan, J. M. (1983). "Soil-Structure Interaction Effects of Compaction-induced Stresses and Deflections." *Geotechnical Engineering Research Report No. UcB/GT/83-06*, Univ. of California Berkeley, CA.

30. Sowers, G. F., Robb, A. D., Mullis, C. H., and Glenn, A. J. (1957). "The Residual Lateral Pressures Produced by Compacting Soils." *Proceedings, 4th International Conference on Soil Mechanics and Foundation Engineering*, London, 243-247.

31. Terzaghi, K. (1934). "Large retaining-wall tests (I): Pressure of dry sand." *Engineering News-Record*, 112, 136-140.

32. Terzaghi, K. (1941). " General wedge theory of earth pressure." *ASCE Transactions*, 106, 68-80.

33. Terzaghi, K. (1943). *Theoretical Soil Mechanics*, Wiley, New York.

34. Tzeng, S. K., (2002). "Horizontal Pressure on an Unyielding Wall due to Strip Loading on Backfill with Different Densities." MS thesis, Dept. of Civil Engineering, National Chiao Tung University, Hsinchu, Taiwan.

35. US NAVY. (1982). "Foundations and Earth Structures." *NAVFAC Design Manual DM-7.2*. Naval Facilities Engineering Command, U.S. Government Printing Office, Washington, D. C., 60.

36. Vesic, A. S. (1973). " Analysis of Ultimate Loads of Shallow Foundations." *Journal of the Soil Mechanics and Foundations Division*, 99(SM1), 45-73.

37. Vesic, A. S., Banks, D. C., and Woodard, J. M. (1965). " An Experimental Study of Dynamic Bearing Capacity of Footings on Sand." *Proceedings, Sixth International Conference on Soil Mechanics and Foundation Engineering*, Montreal, Canada, II, 209-213.

38. Wang, F. J., (2005). "Effects of Adjacent Rock Face Inclination on Earth Pressure at-rest." MS thesis, Dept. of Civil Engineering, National Chiao Tung University, Hsinchu, Taiwan.
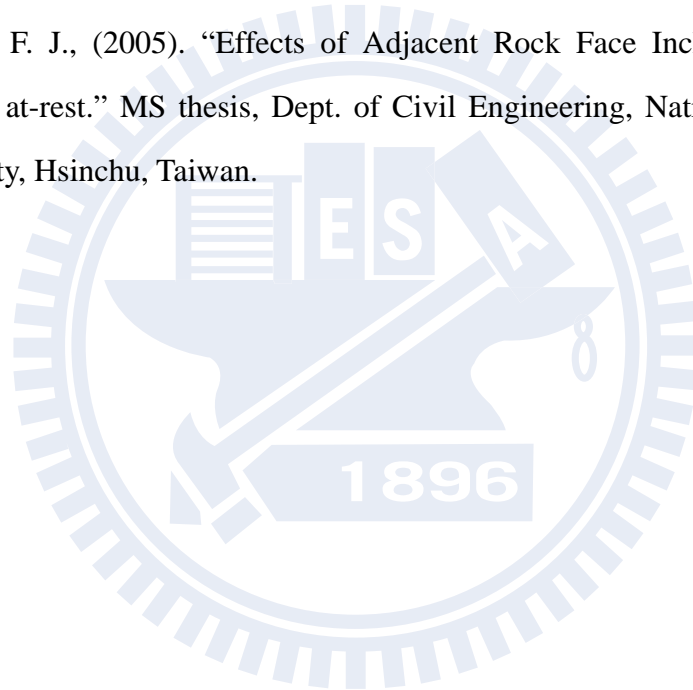
Table 3.1. Technical Information of the Eccentric Motor

Manufacture	Mikasa
Type	KJ75-2P
Power (Watt)	75
Voltage (Volt)	220
Frequency (Hz)	50/60
Vibration per Minute	3000/3600
Mass (kg)	6.2

Table 4.1. Properties of Ottawa Sand (after Chen, 2003)

Shape	Rounded
e_{max}	0.76
e_{min}	0.50
G_s	2.65
D_{60} (mm)	0.39
D_{10} (mm)	0.26
C_u	1.5
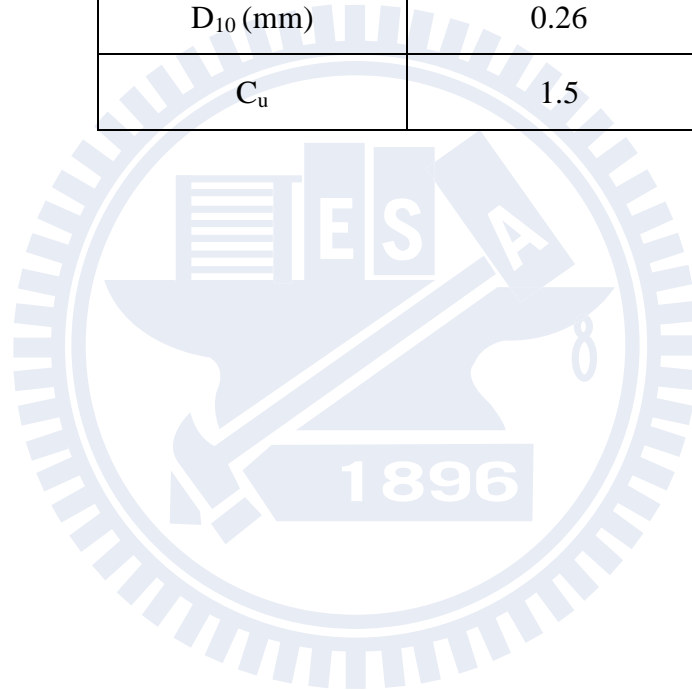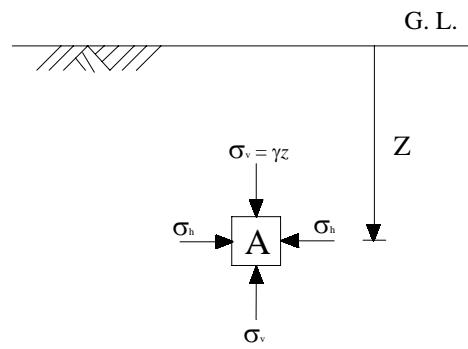
(a)
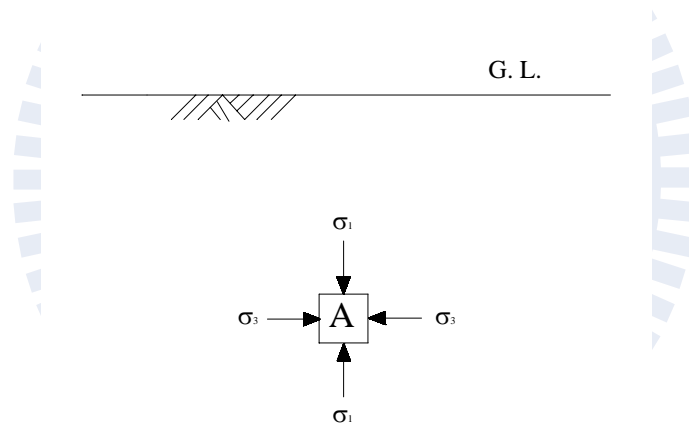
(b)

Fig. 2.1 Development of in-situ Stresses
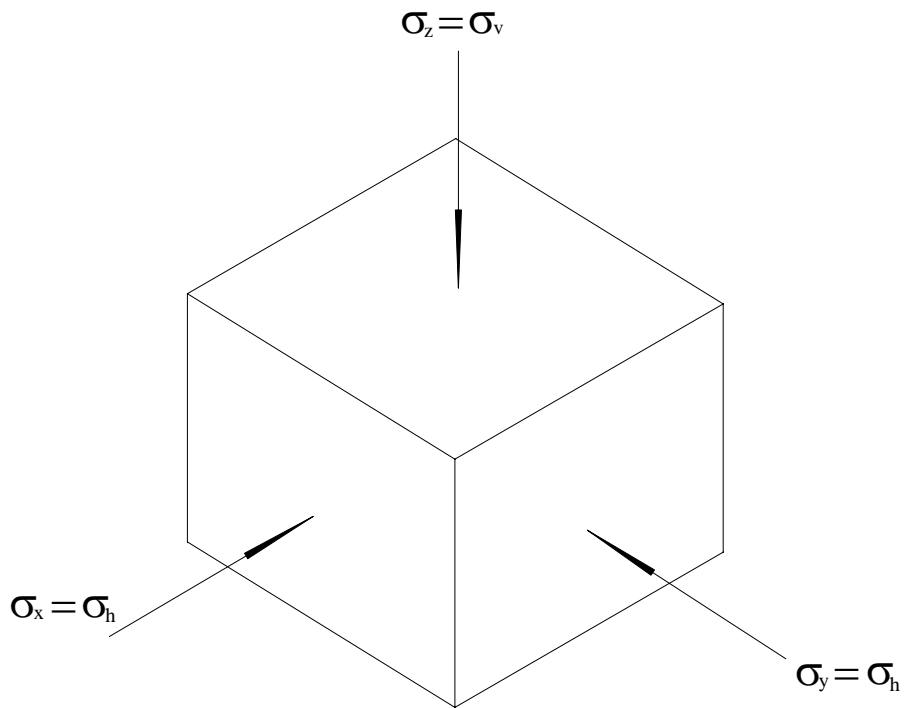
Fig. 2.2. Principal Stresses in a Soil Element
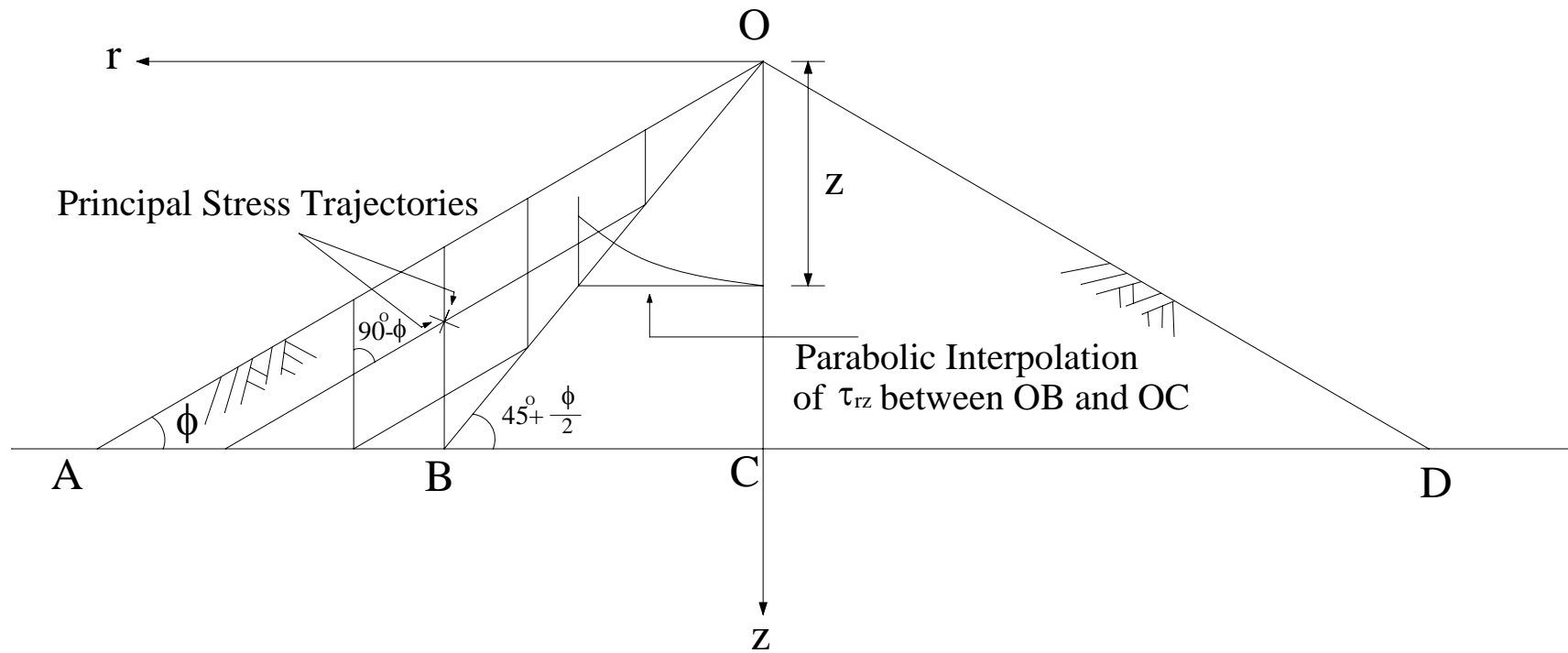
Fig. 2.3. Jaky's Formulation of the Relationship between K_o on OC and ϕ Mobilized in OAB
(after Mesri and Hayat, 1993)
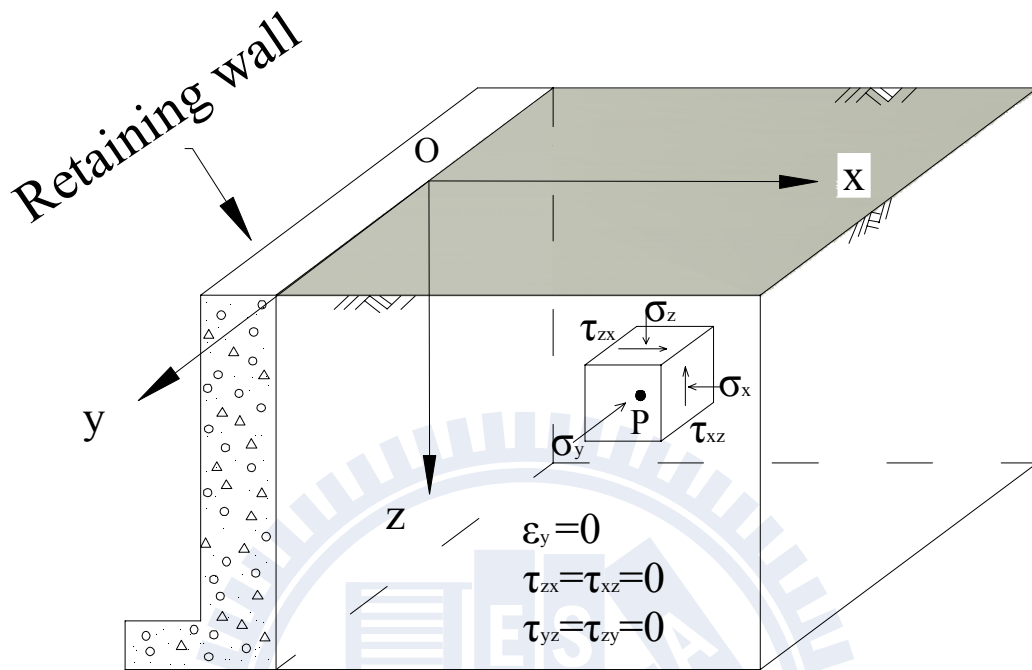
Fig. 2.4. Definition of plane strain state-of-stress

Applied load = q/unit area

Contact stress = q

Settlement
profile

(a)

Applied load = q/unit area

Contact stress

Settlement
profile
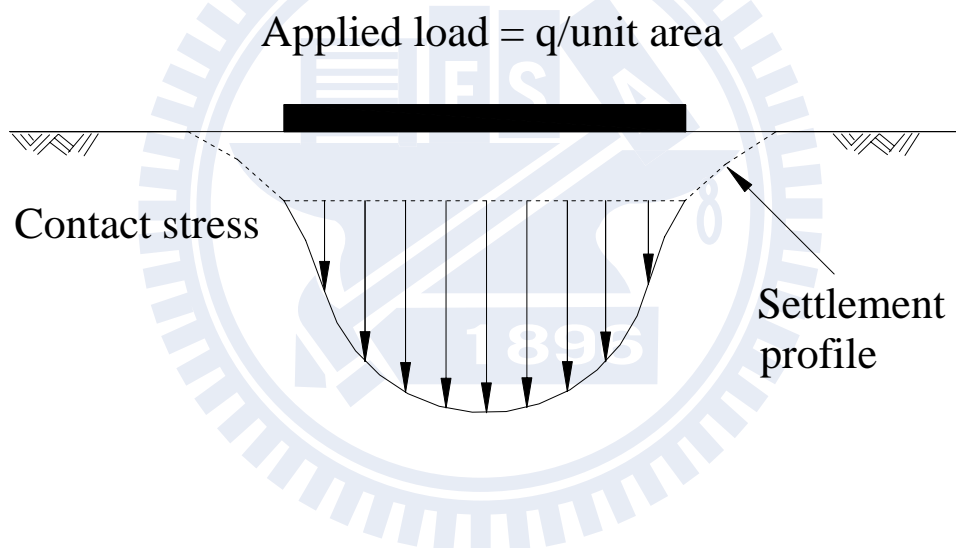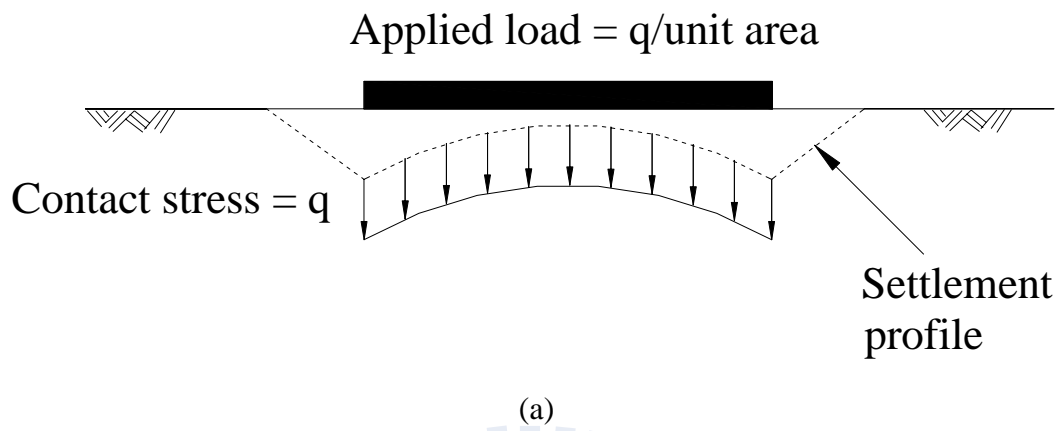
Fig. 2.5. Flexible (a) and Rigid (b) foundation on sand
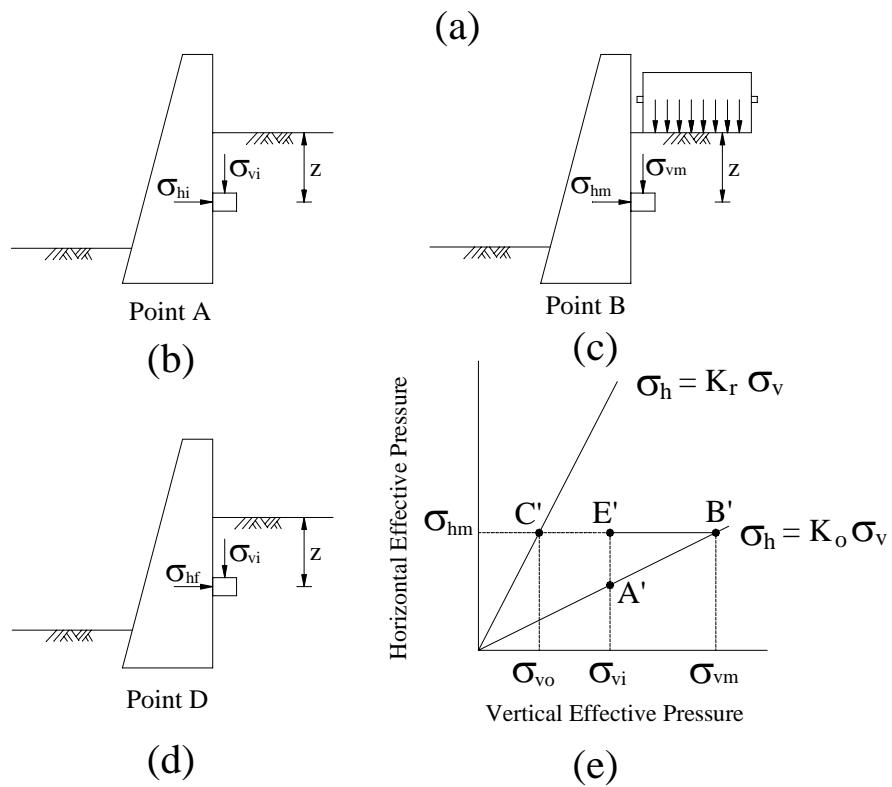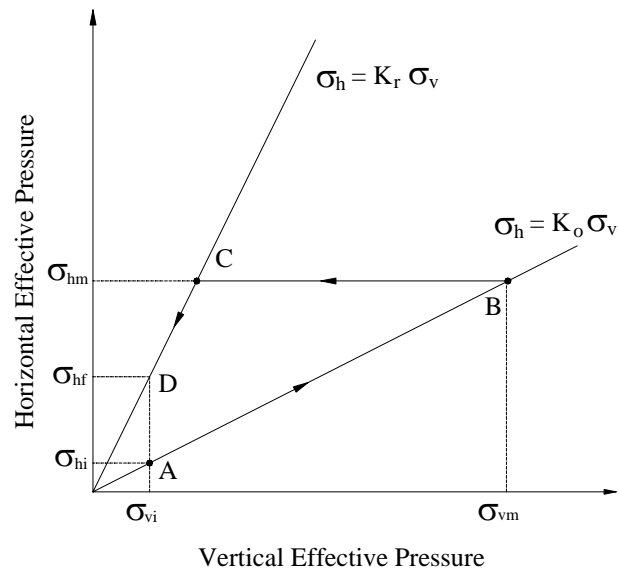
Fig. 2.6. Broms's simplified compaction pressure theory
(after Broms, 1971)
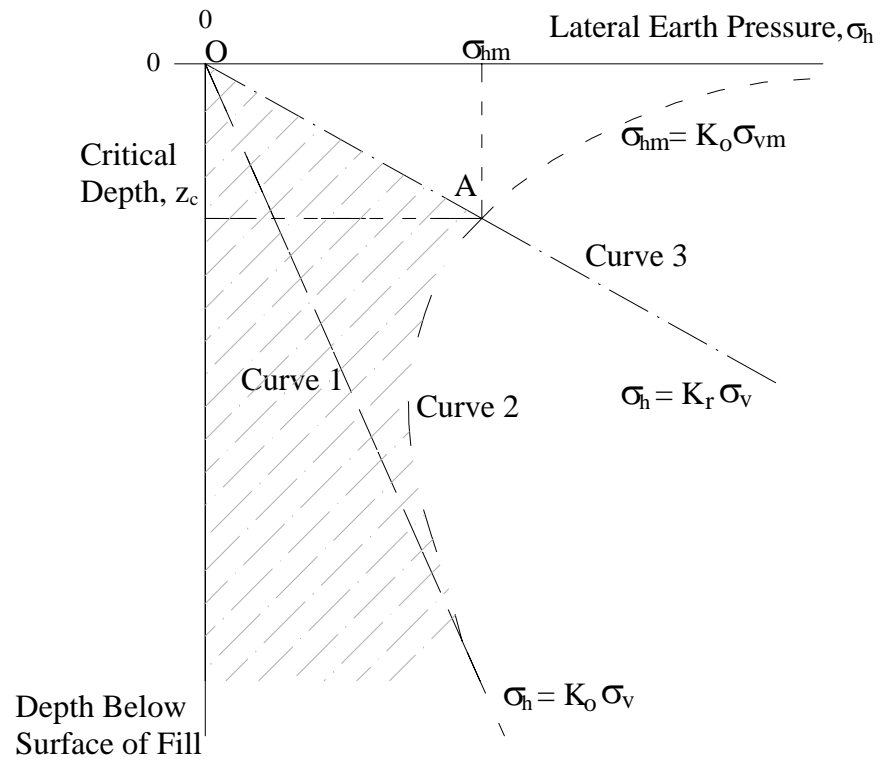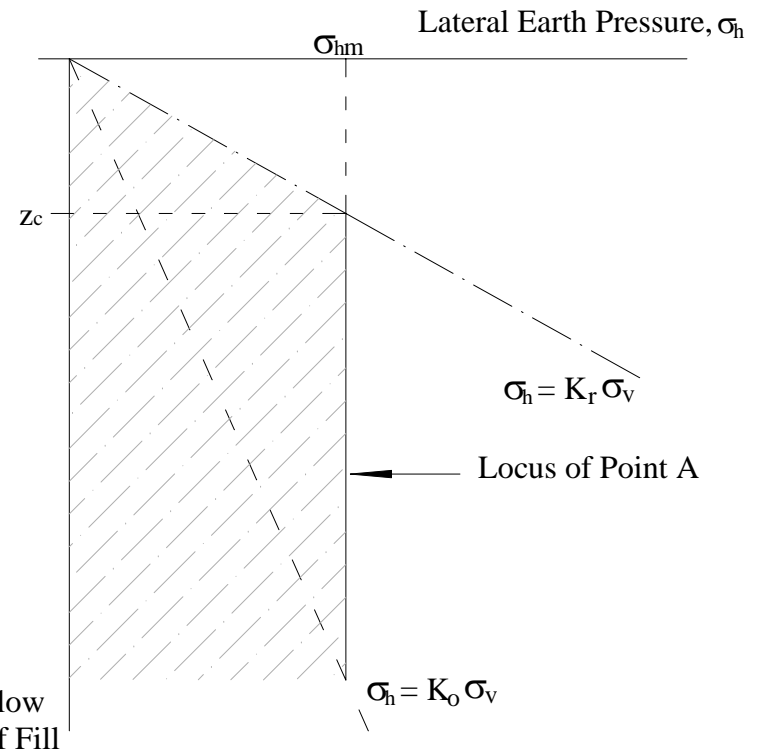
Fig. 2.7. Lateral pressure distribution due to compaction of fill
(after Broms, 1971)
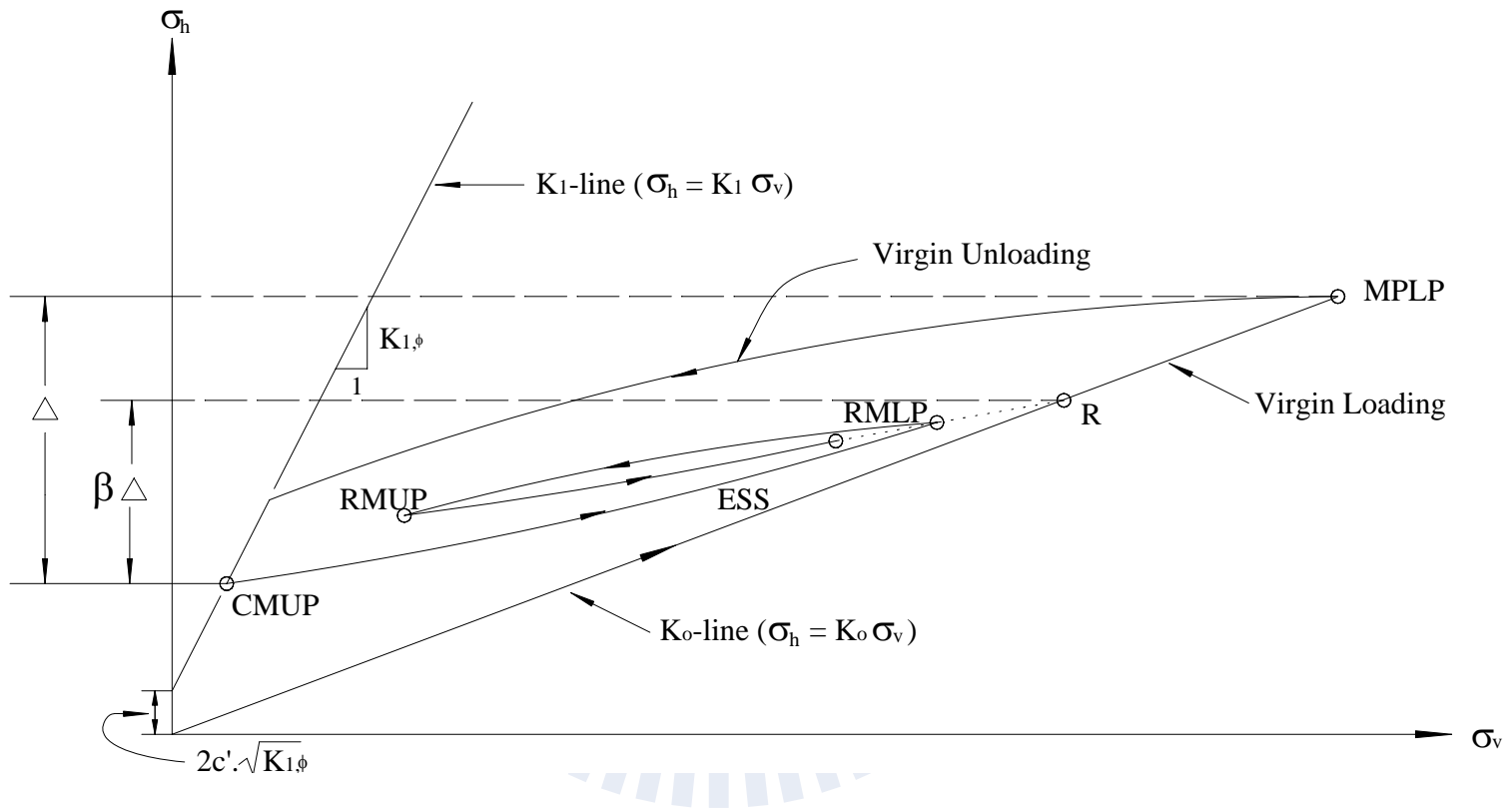
Fig. 2.8. Basic components of hysteretic K_o-loading/unloading model
(after Duncan and Seed, 1986)
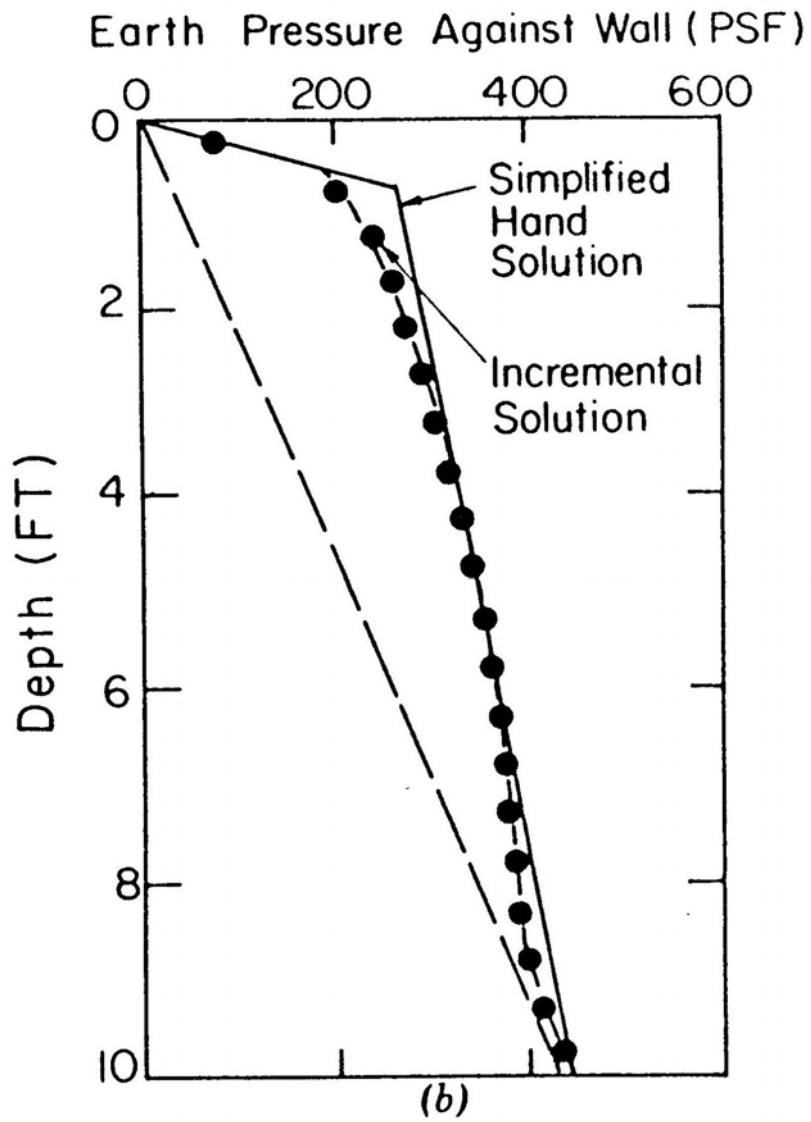
Fig. 2.9. Comparison between Final Pressure Distributions Based on Incremental Analysis and Hand Solution (after Duncan and Seed, 1983)
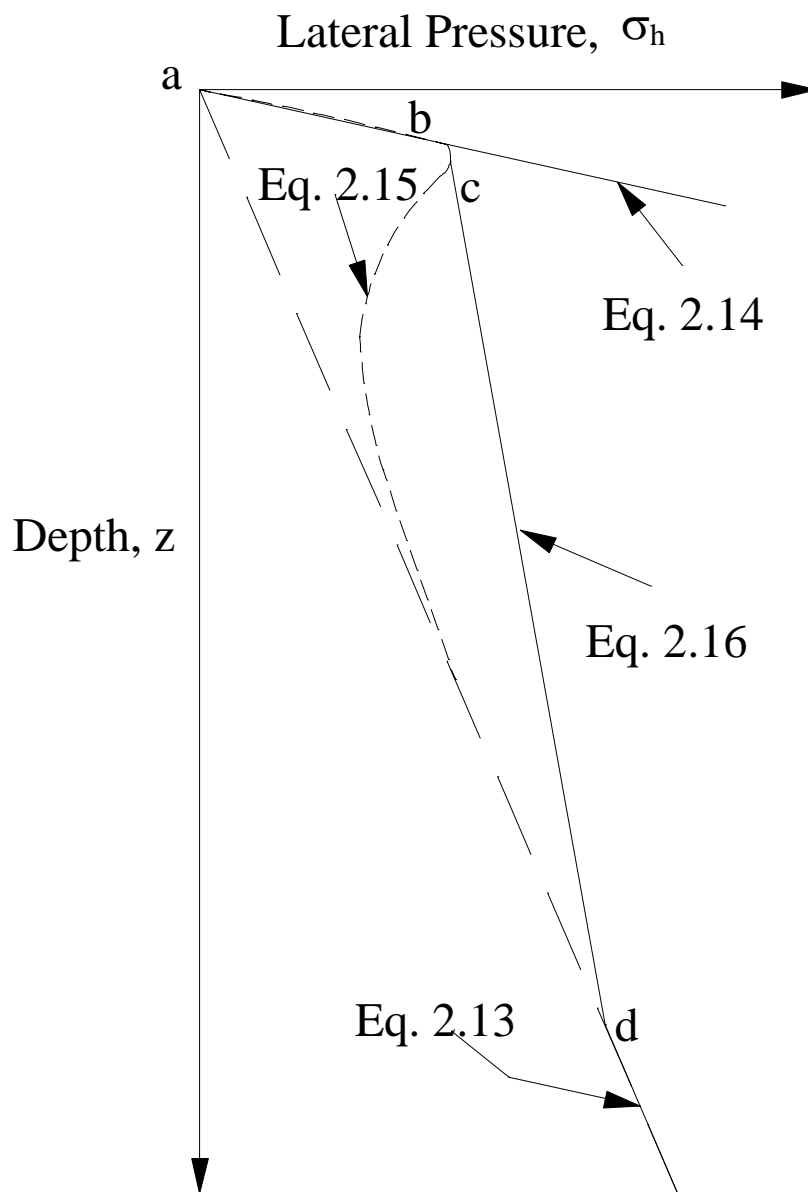
Fig. 2.10. Hand-calculation for estimating σ_h (after peck and Mesri, 1987)
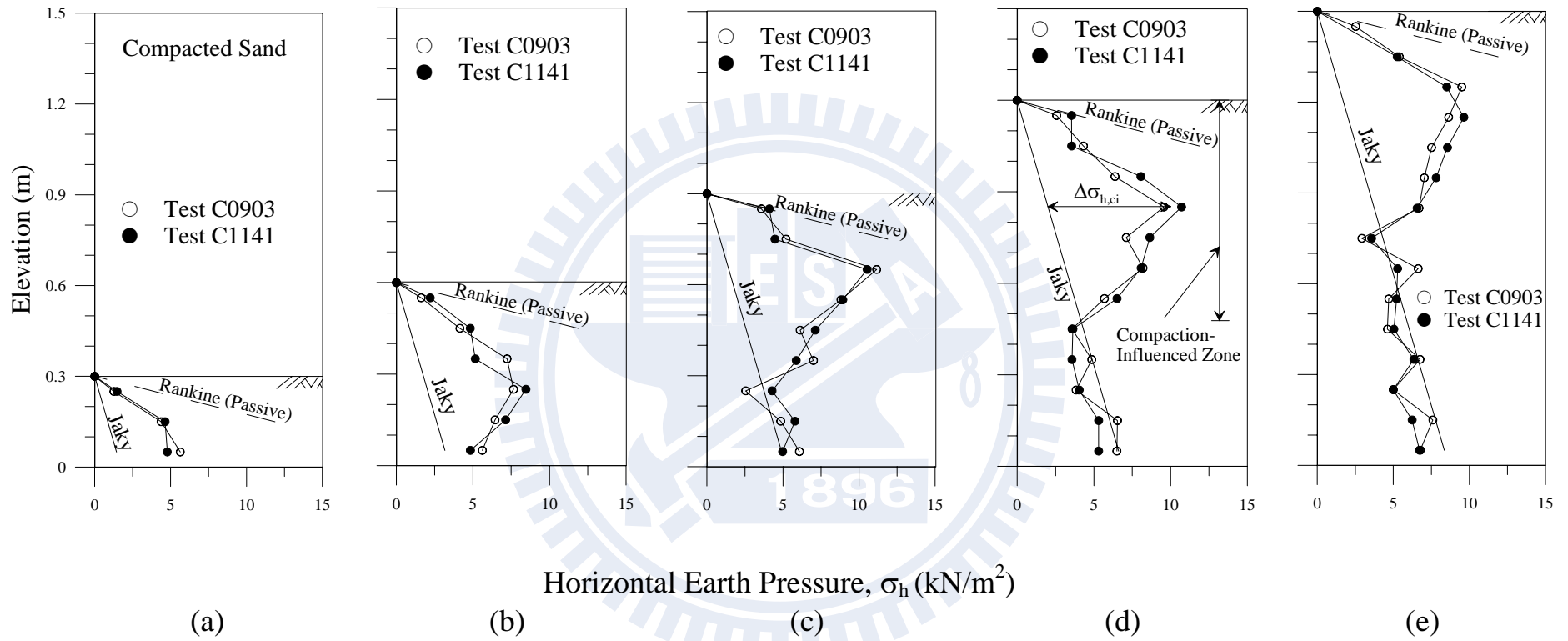
Fig. 2.11. Distribution of Horizontal Earth Pressure after Compaction (after Chen and Fang, 2008)

51
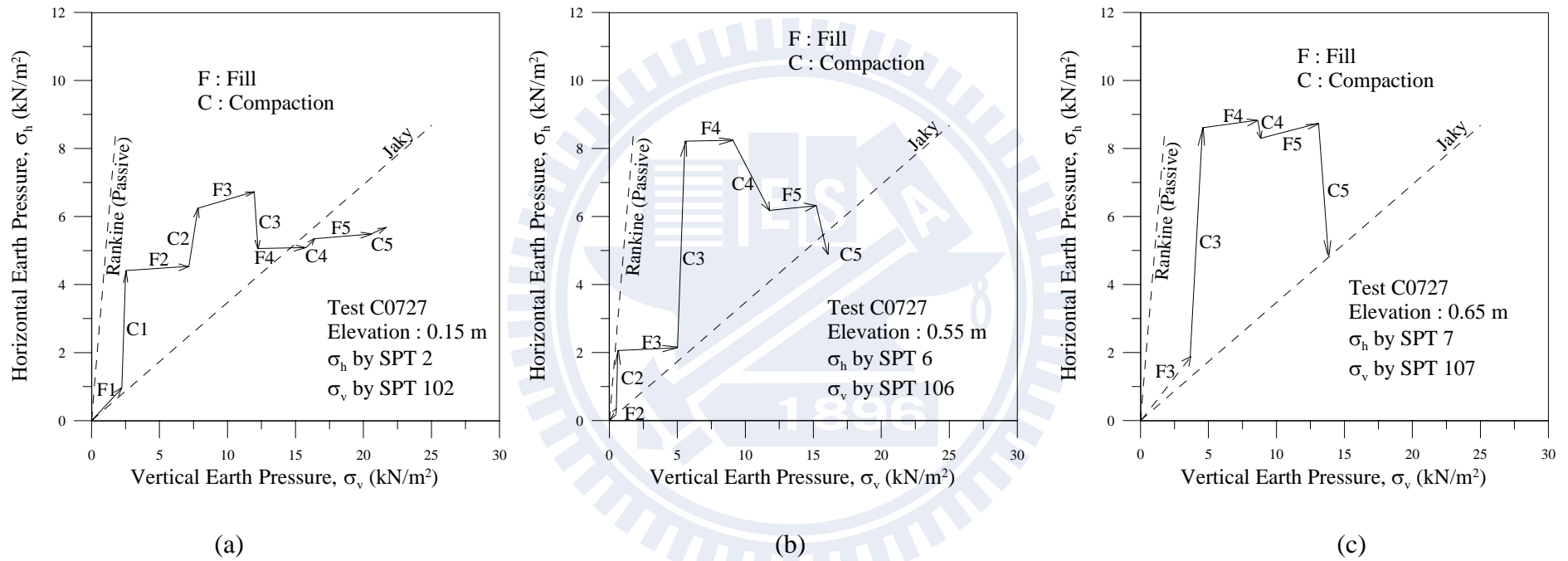
Fig. 2.12. Stress path of a soil element under compaction (after Chen and Fang, 2008)
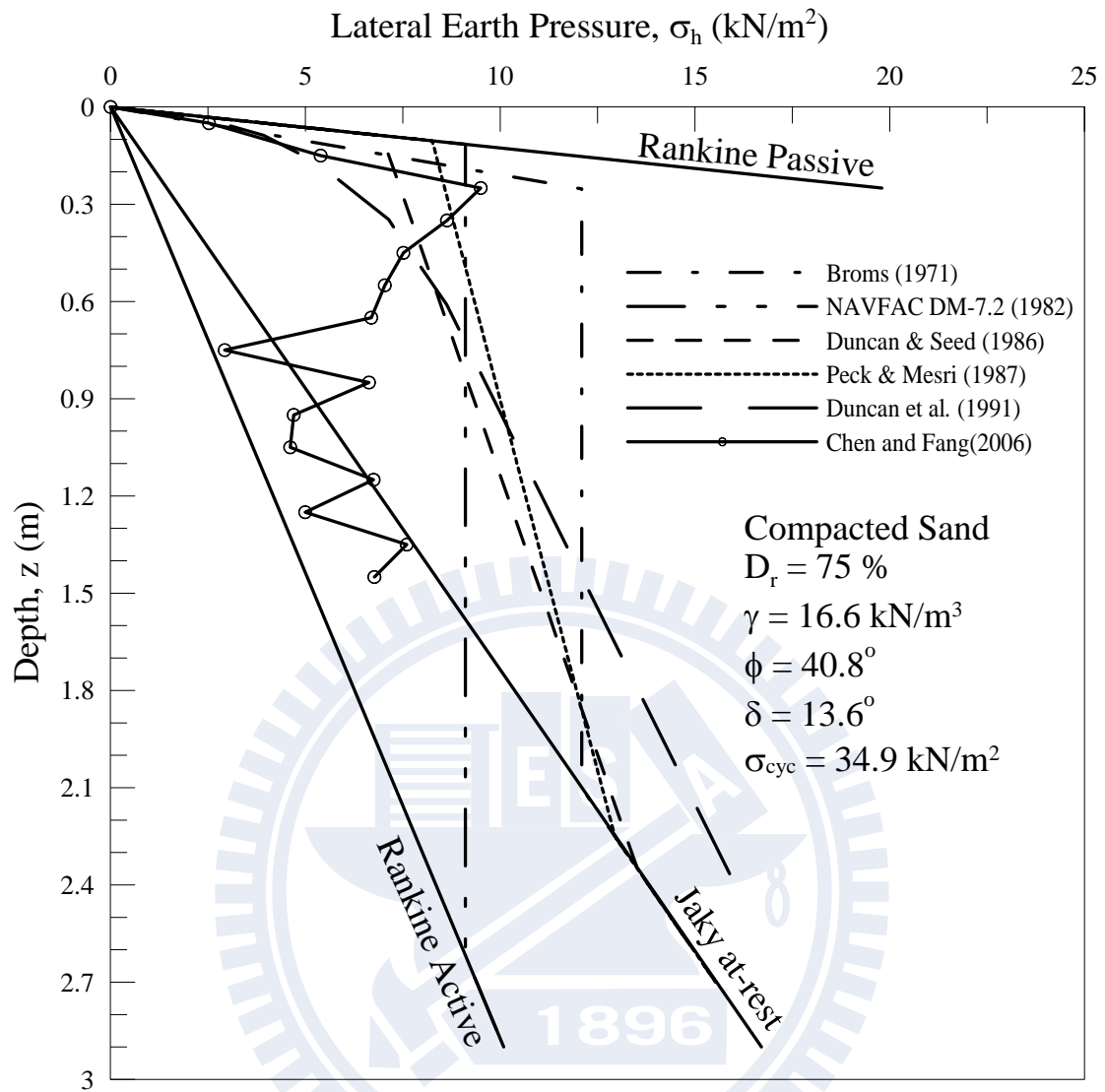
Fig. 2.13. Horizontal Earth Pressure Estimated with Various Methods after
Compaction (after Chen and Fang, 2008)

53
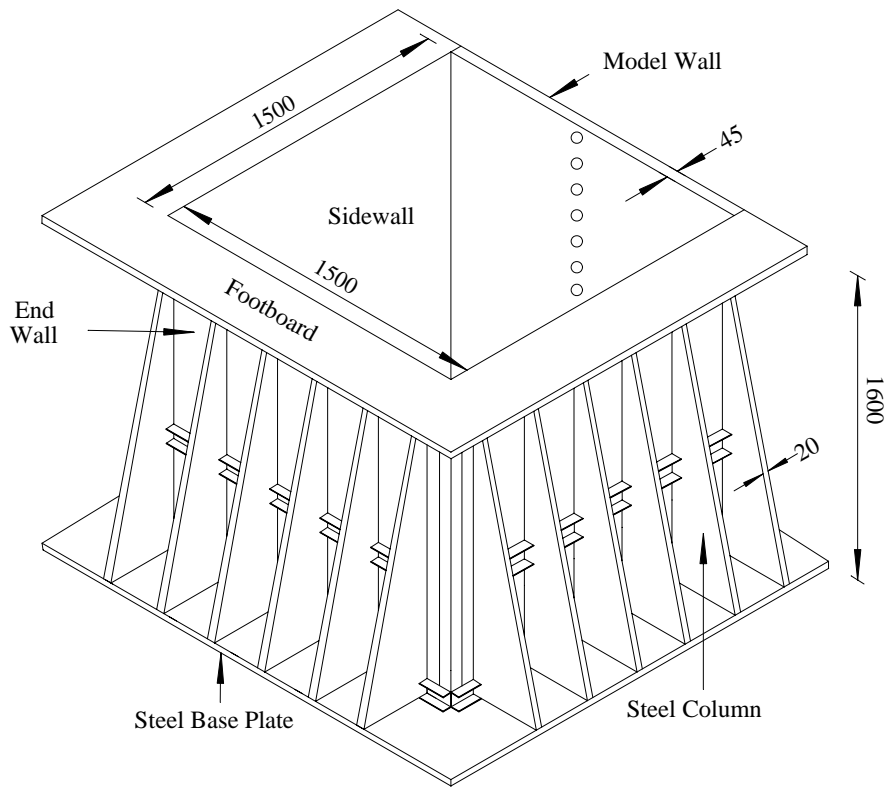
Unit : mm

Fig. 3.1. NCTU nonyielding Retaining-Wall Facility (after Chen and Fang, 2008)
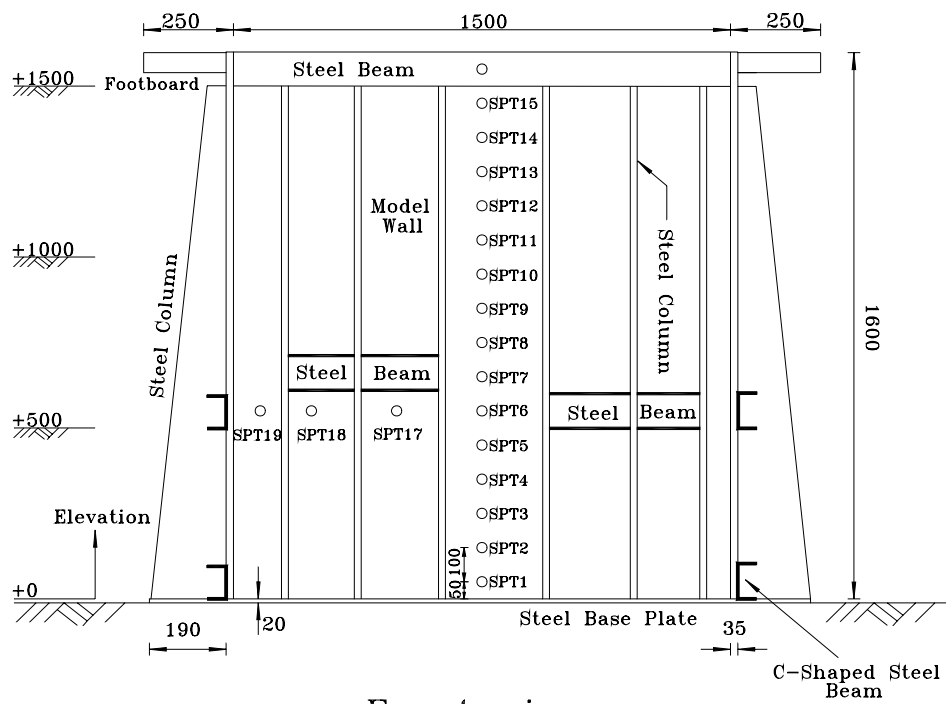
Front-view
Unit : mm

Fig. 3.2. Locations of soil-pressure transducers mounted on the wall
(after Chen, 2003)

Fig. 3.3. Soil-pressure transducer (Kyowa PGM-02KG) (after Chen, 2003)

Fig. 3.4. Soil-Pressure Transducer (Kyowa BE-2KCM17) (after Chen, 2003)

**Personal Computer
Labview Program**

**Dynamic Strain Amplifiers
(Kyowa: DPM601A and
DPM711B)**

**NI BNC – 2090
AD/DA Card**

Fig. 3.5. Data Acquisition System

Extension Cord
(5 m-Long)

Switch

Handle

20

1000

10

Eccentric
Motor

15

40

27

48

225

48

360
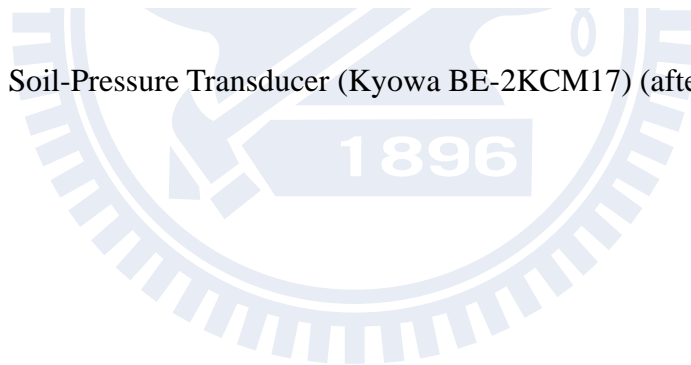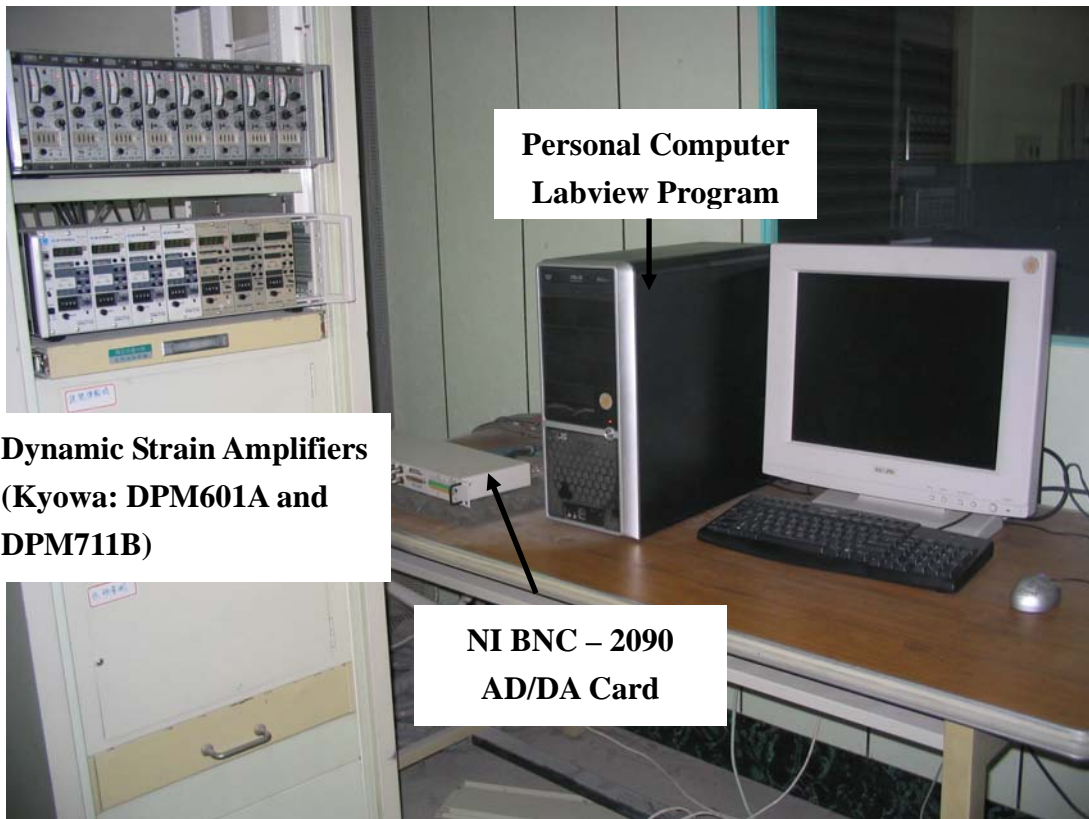
Unit : mm
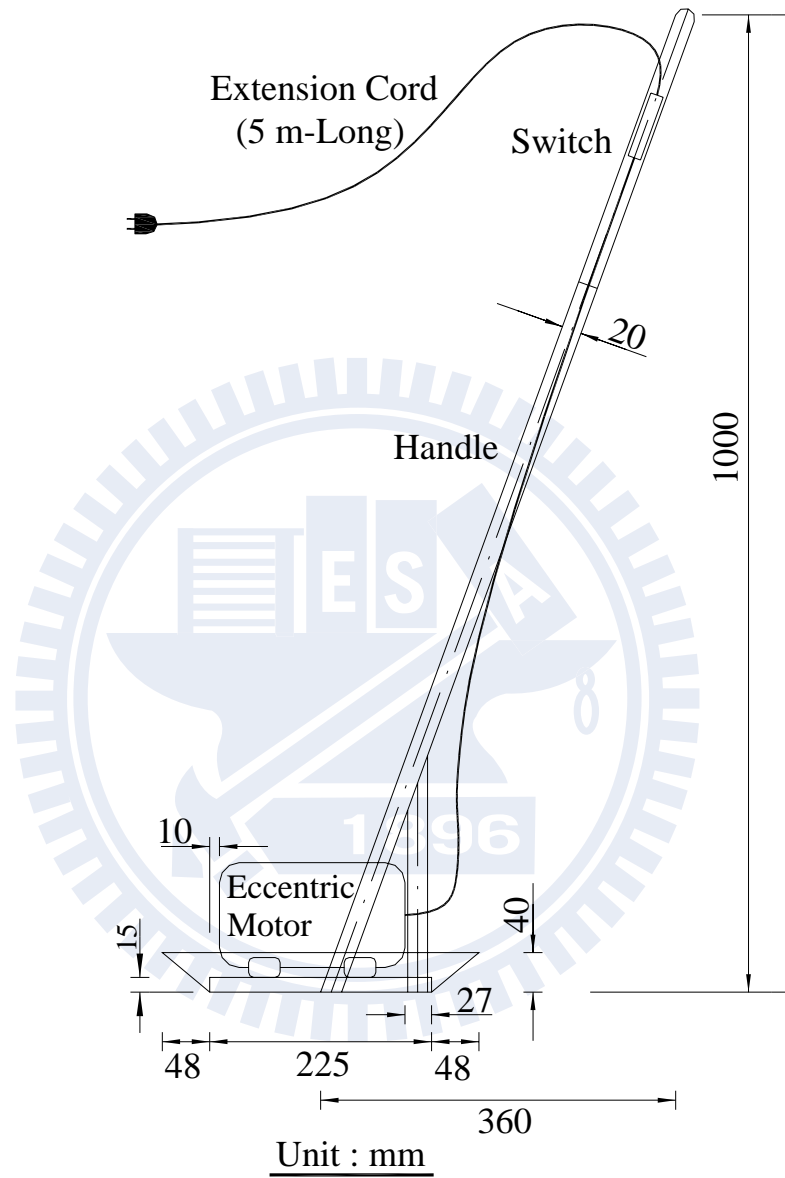
Fig. 3.6. Side-View of Vibratory Soil Compactor (after Chen, 2002)

Fig. 3.7. Vibratory Soil Compactor (after Chen, 2002)
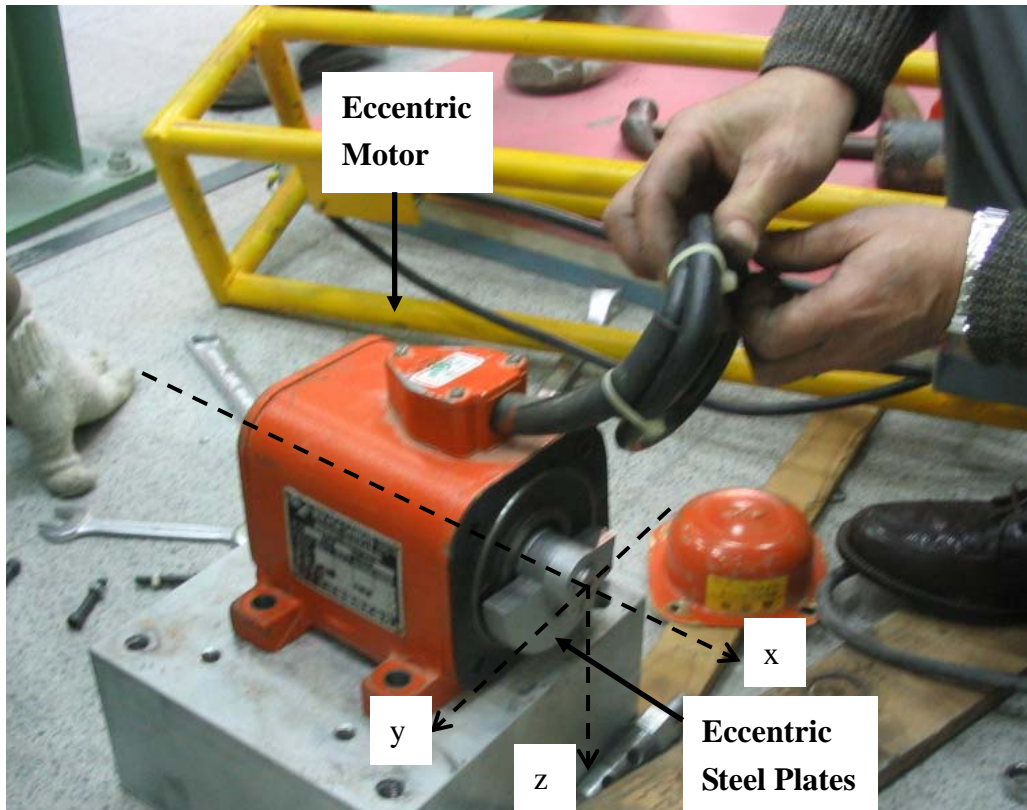
Fig. 3.8. Eccentric Motor with Eccentric Steel Plate (Mikasa KJ75)
(after Wang, 2005)
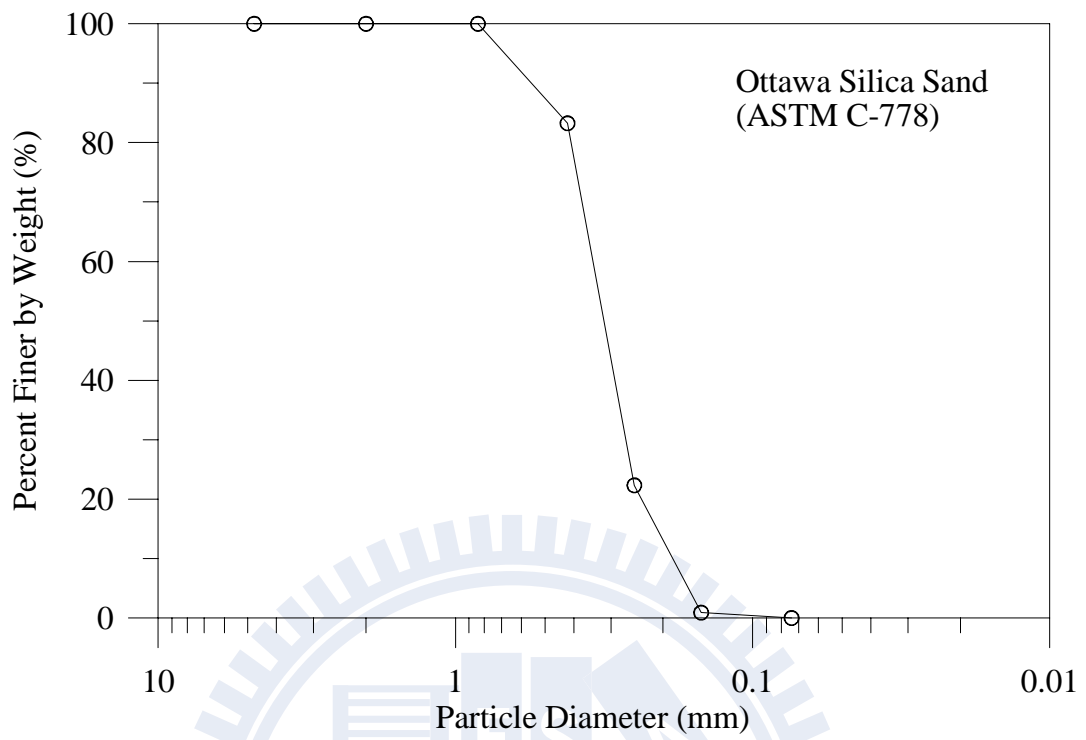
Fig. 4.1. Grain Size Distribution of Ottawa Sand (after Chen, 2003)
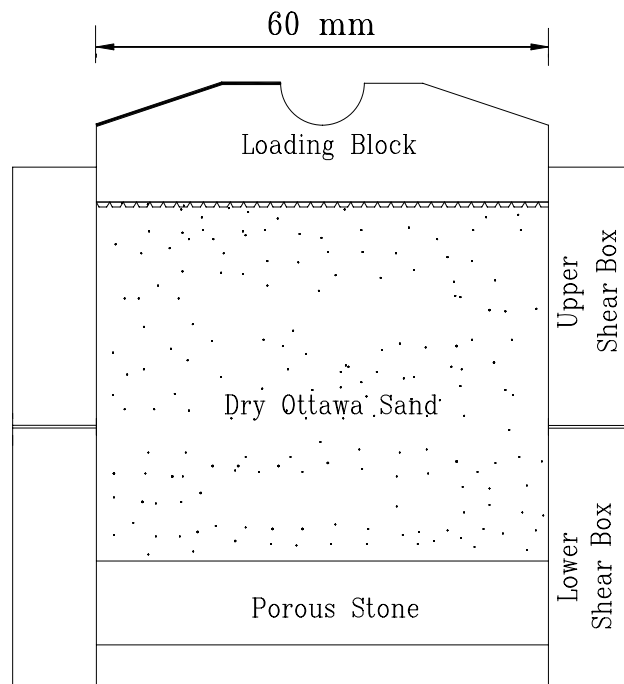
Fig. 4.2. Shear box of direct shear test device (after Wu, 1992)
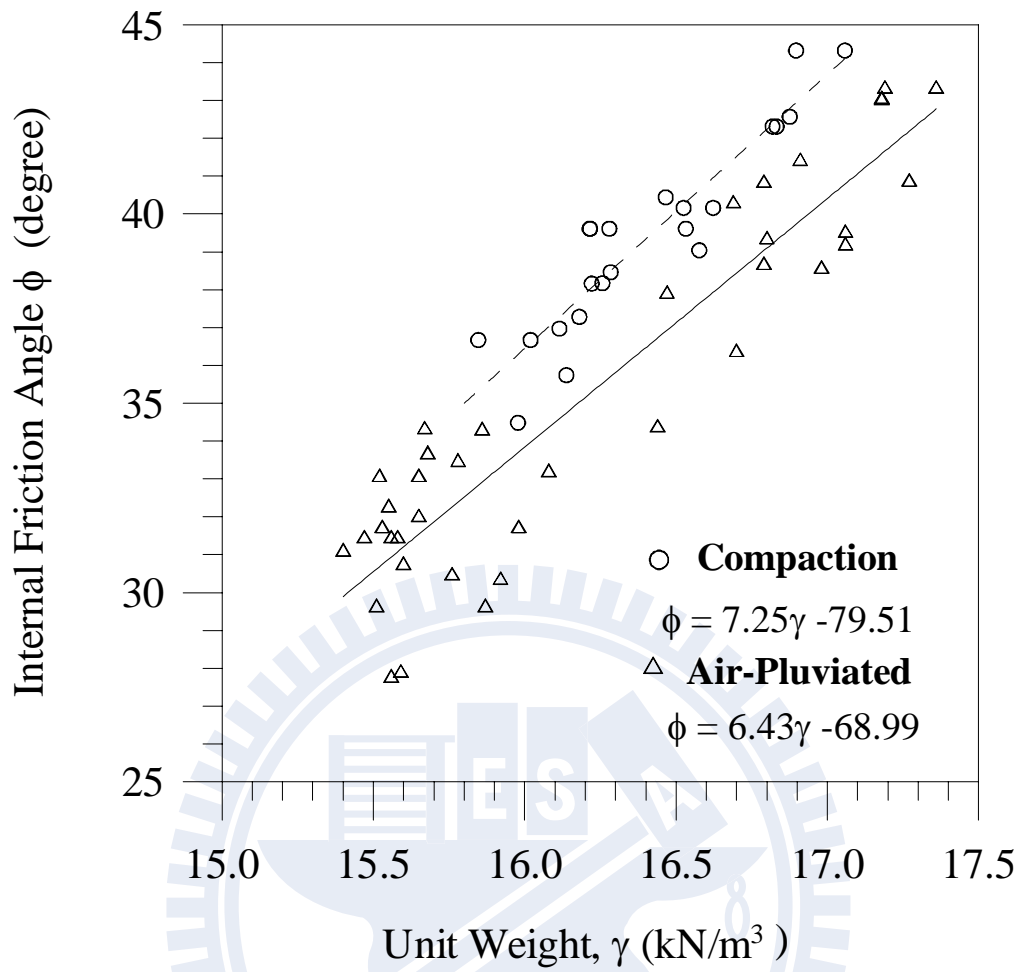
Fig. 4.3. Relationship between Unit Weight γ and Internal Friction Angle ϕ
(after Chang, 2000)
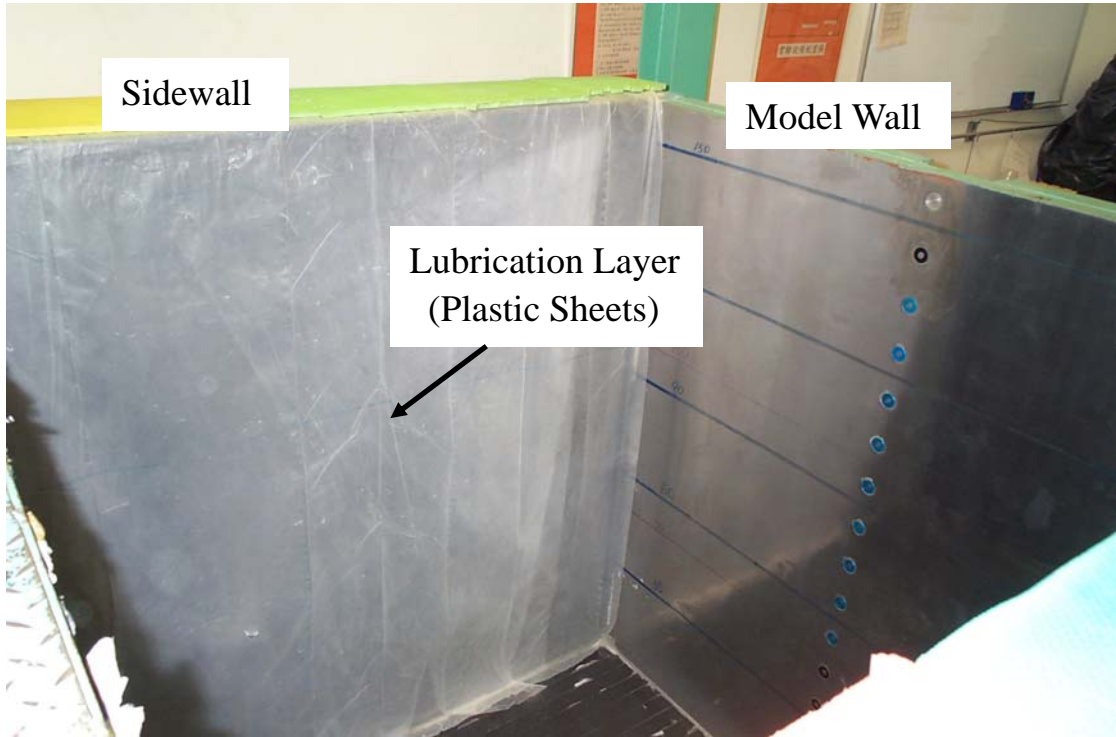
Fig. 4.4. Lubrication Layer on the side Wall
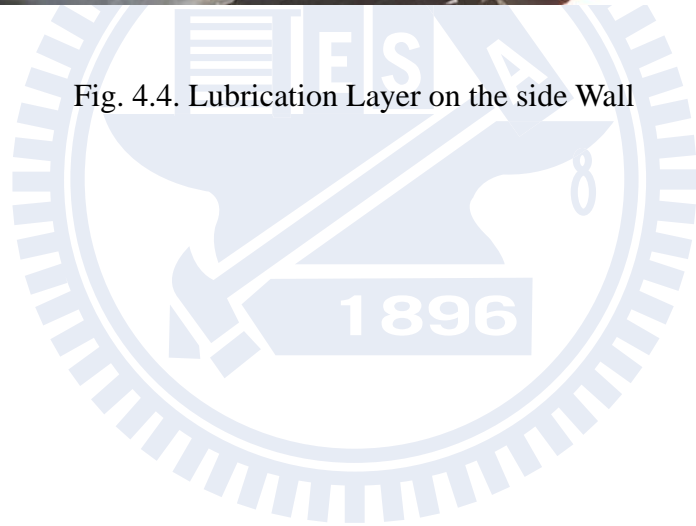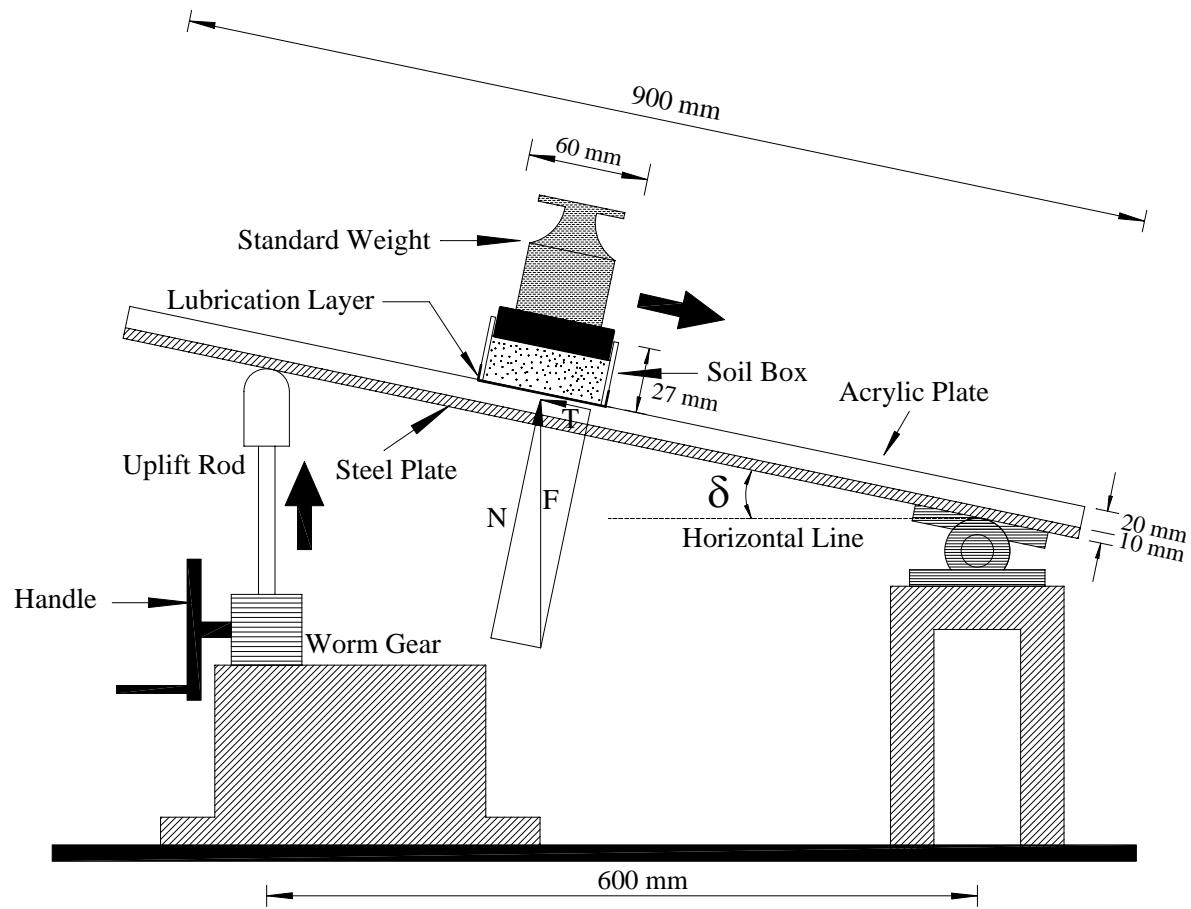
Fig. 4.5. Schematic Diagram of Sliding Block Test (after Fang et al., 2004)
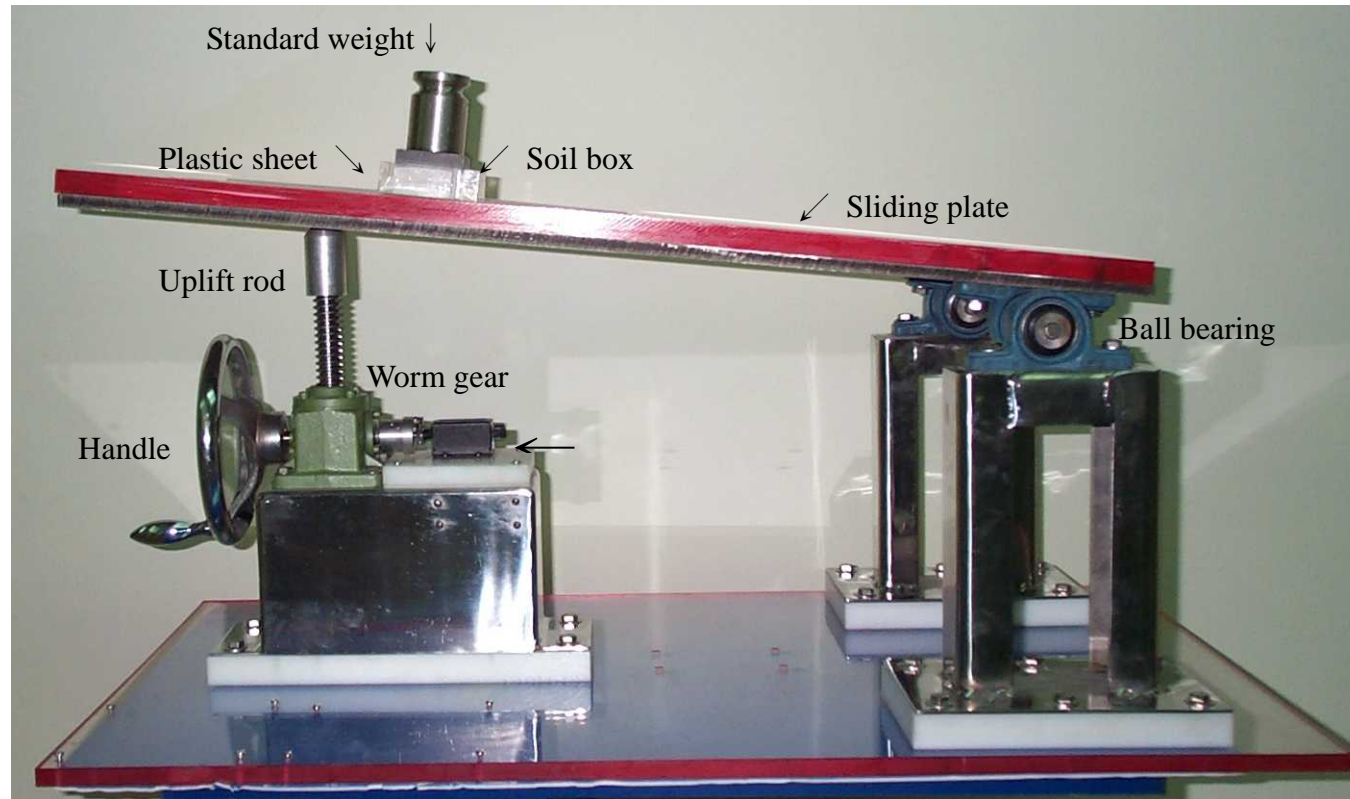
Fig. 4.6. Sliding Block Test Apparatus (after Fang et al., 2004)
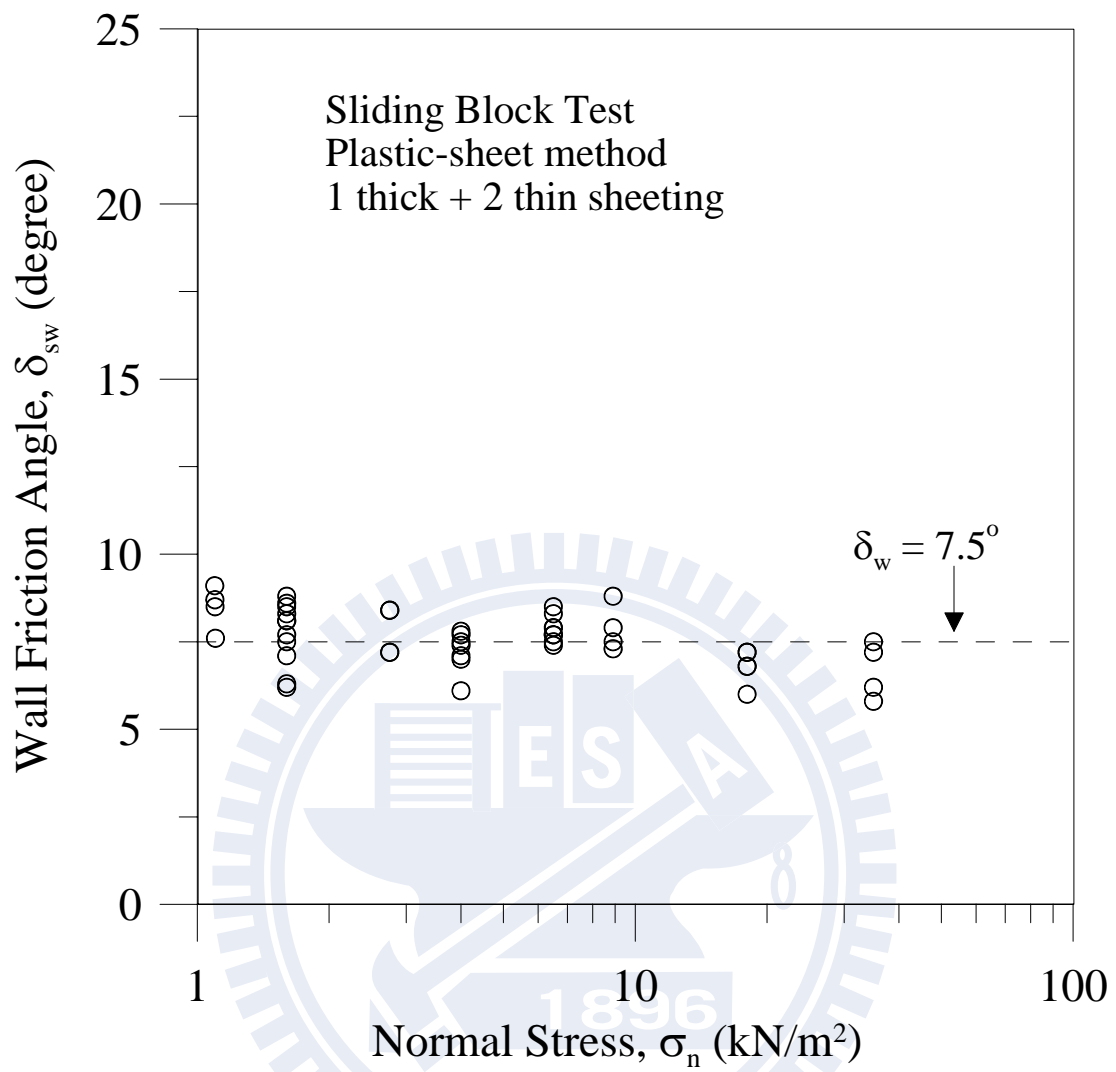
Fig. 4.7. Variation of frition Angle with Normal Stress

(after Fang et al., 2004)
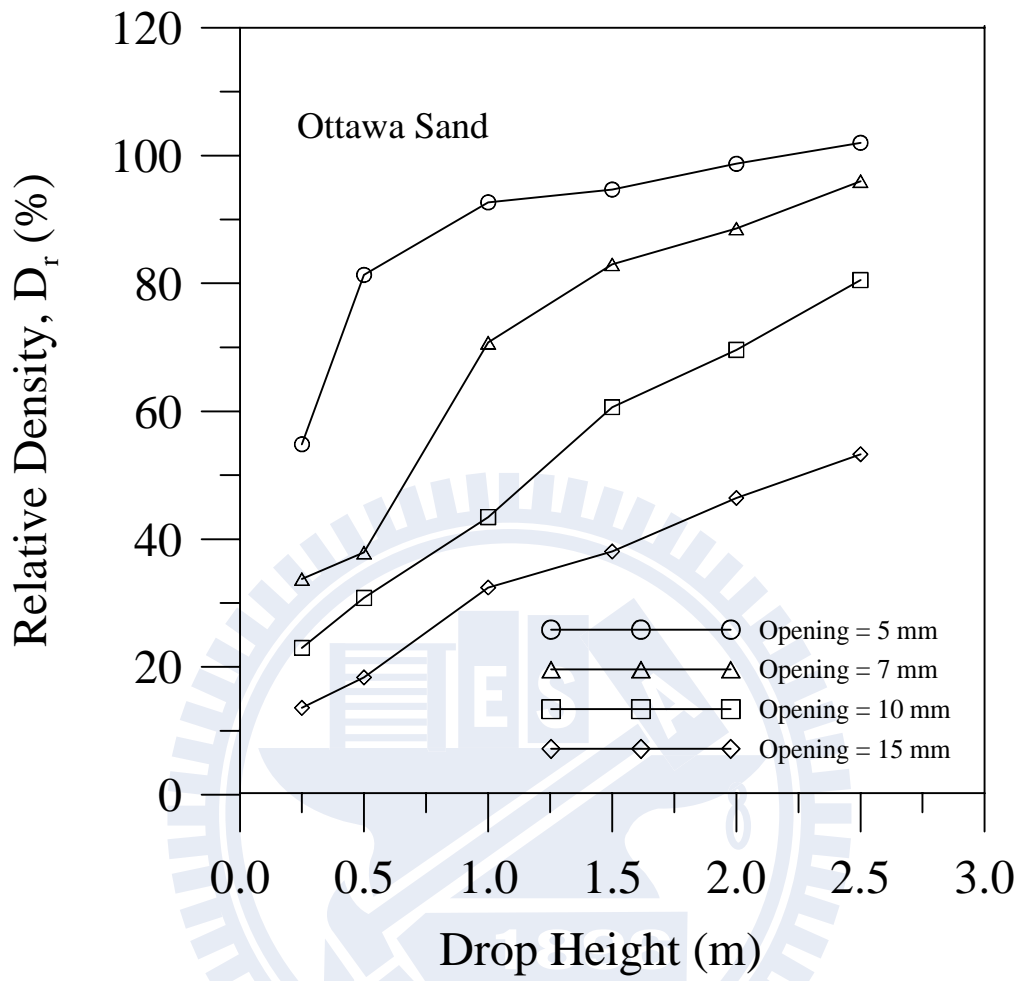
Fig. 4.8 Relationship among Slot Opening, Drop Height, and Relative Density
(after Ho, 1999)

Unit:mm

(b)
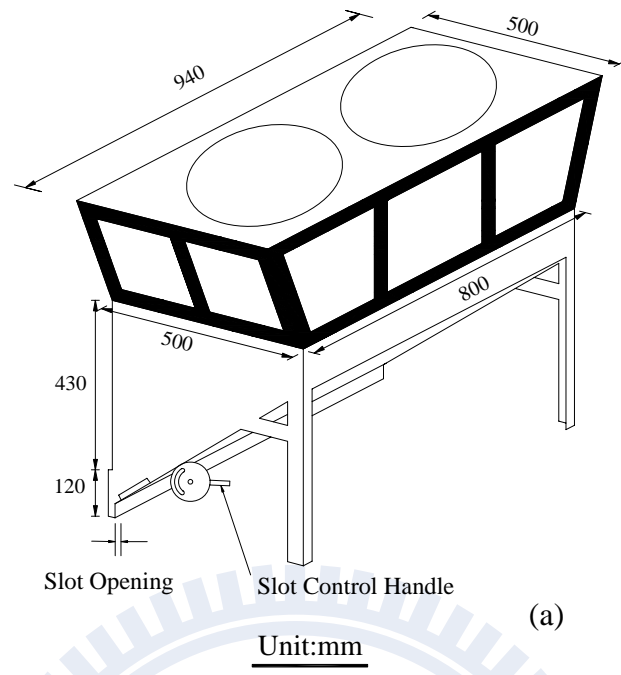
Fig. 4.9. Raining of sand from soil hopper
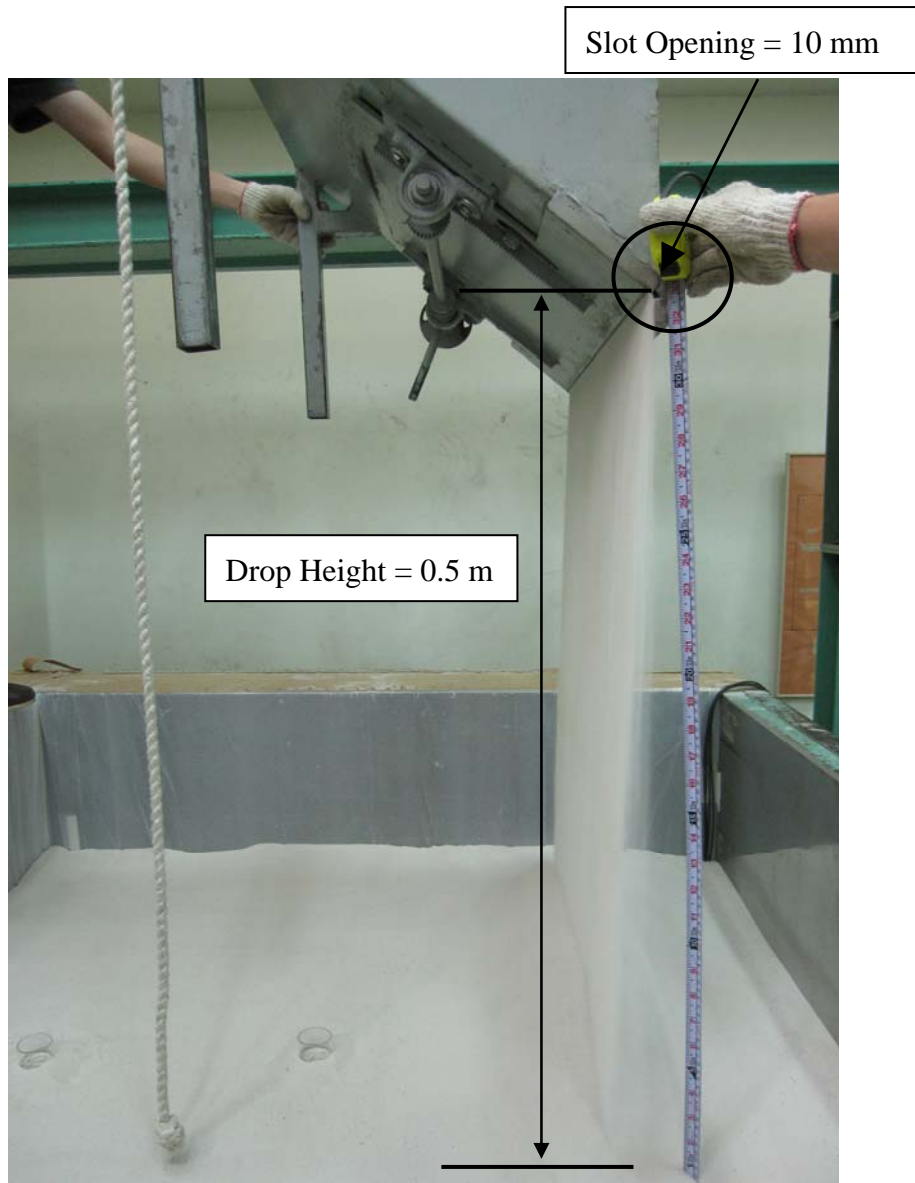
Fig. 4.10 Pluviation of Ottawa Sand into Soil Bin
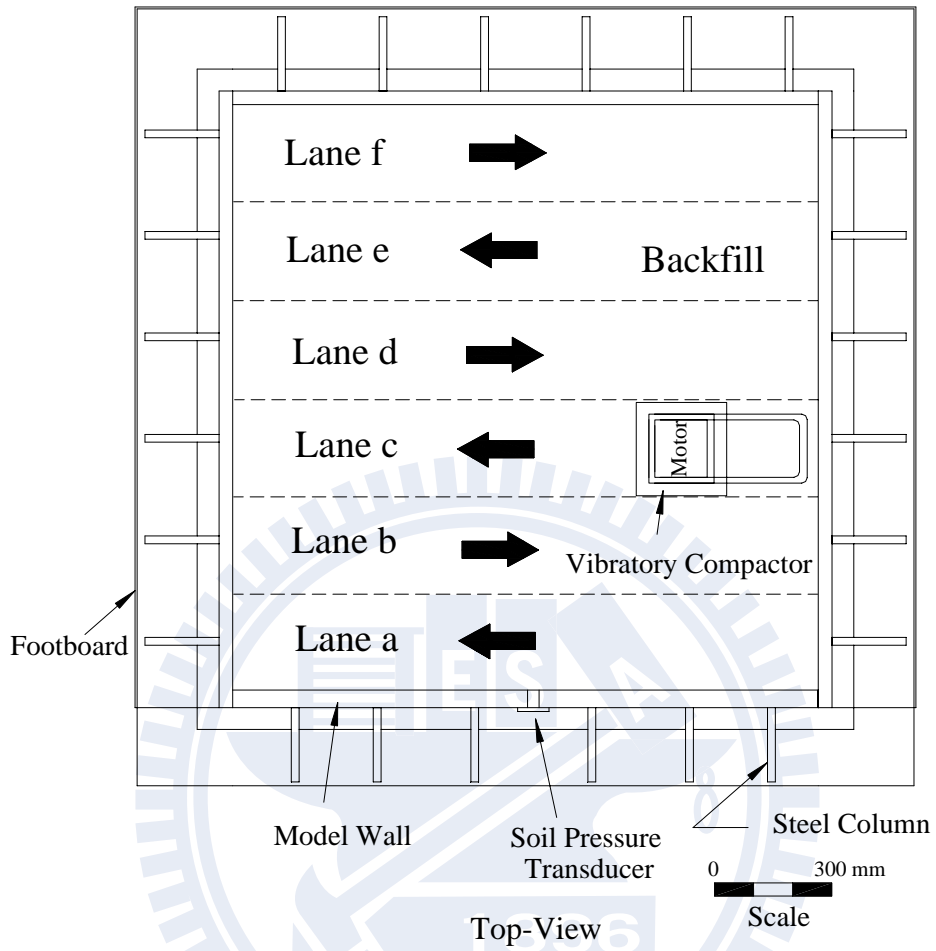
Fig. 4.11. Soil compaction procedure
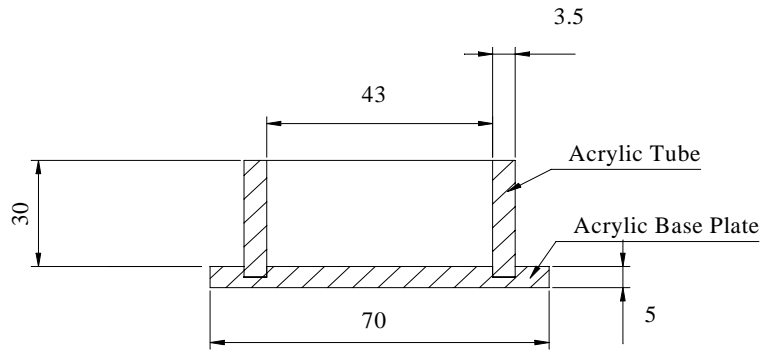
Side-view
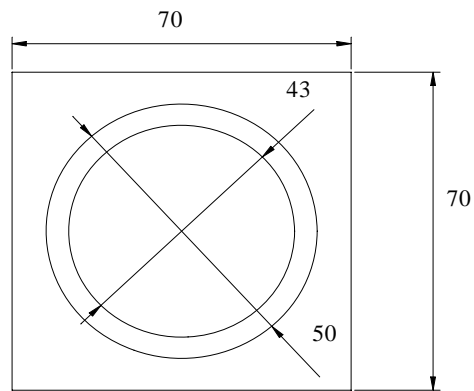
Top-view

unit : mm

Fig. 4.12 Dimensions of Soil Density Cup (after Ho, 1999)
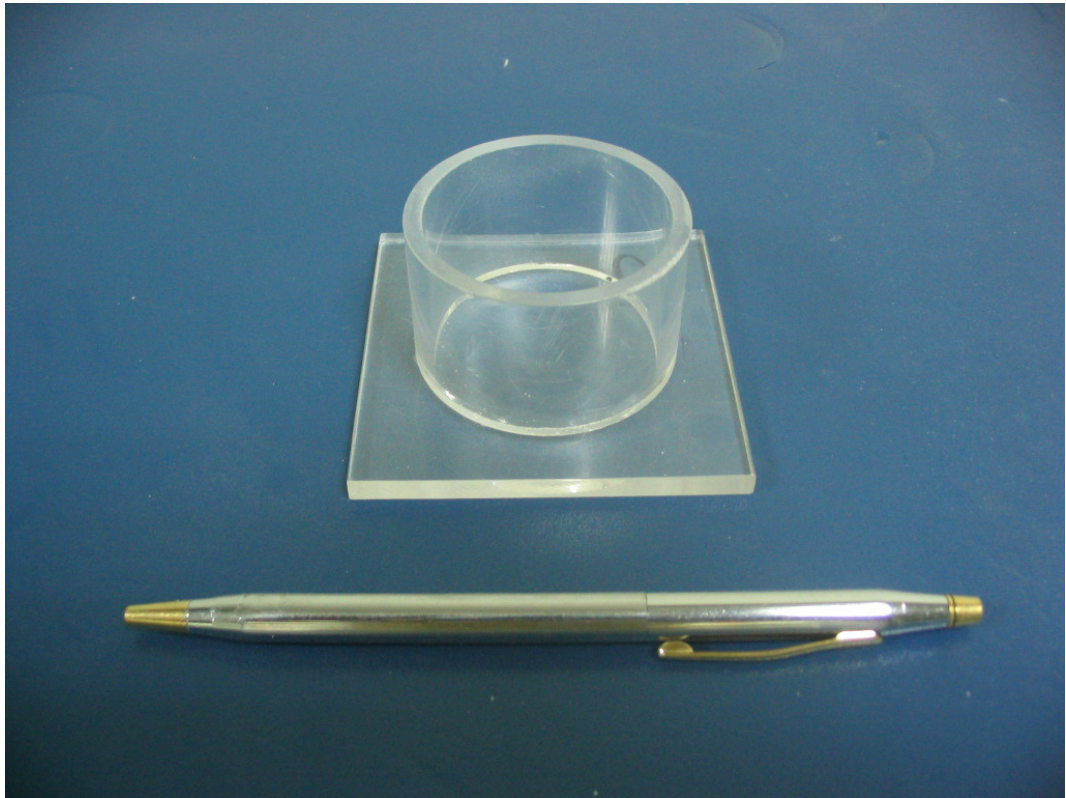
Fig. 4.13. Soil Density Cup (after Chen 2003)
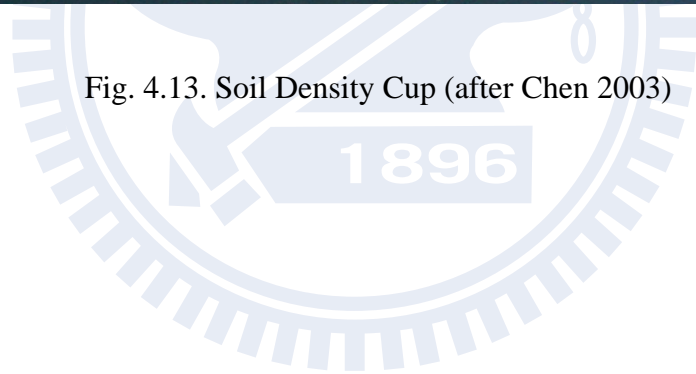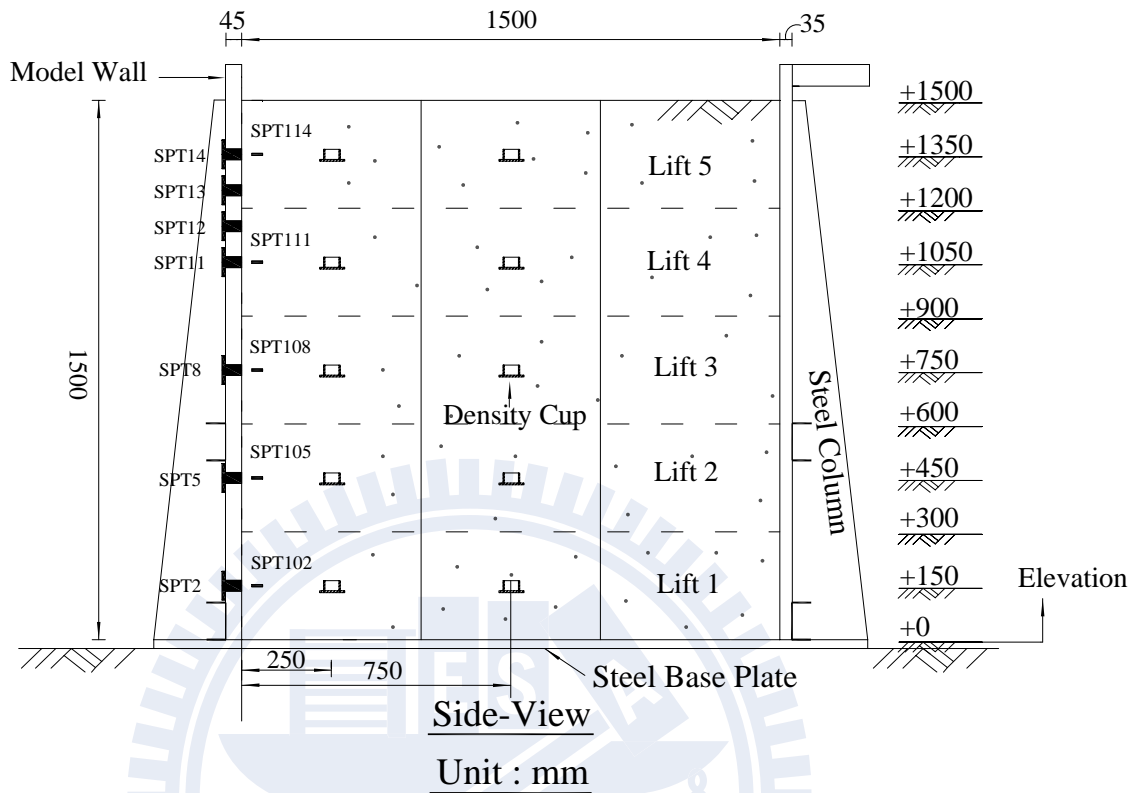
Fig. 4.14 Soil Density Cups Buried at Different Elevations

Top-View
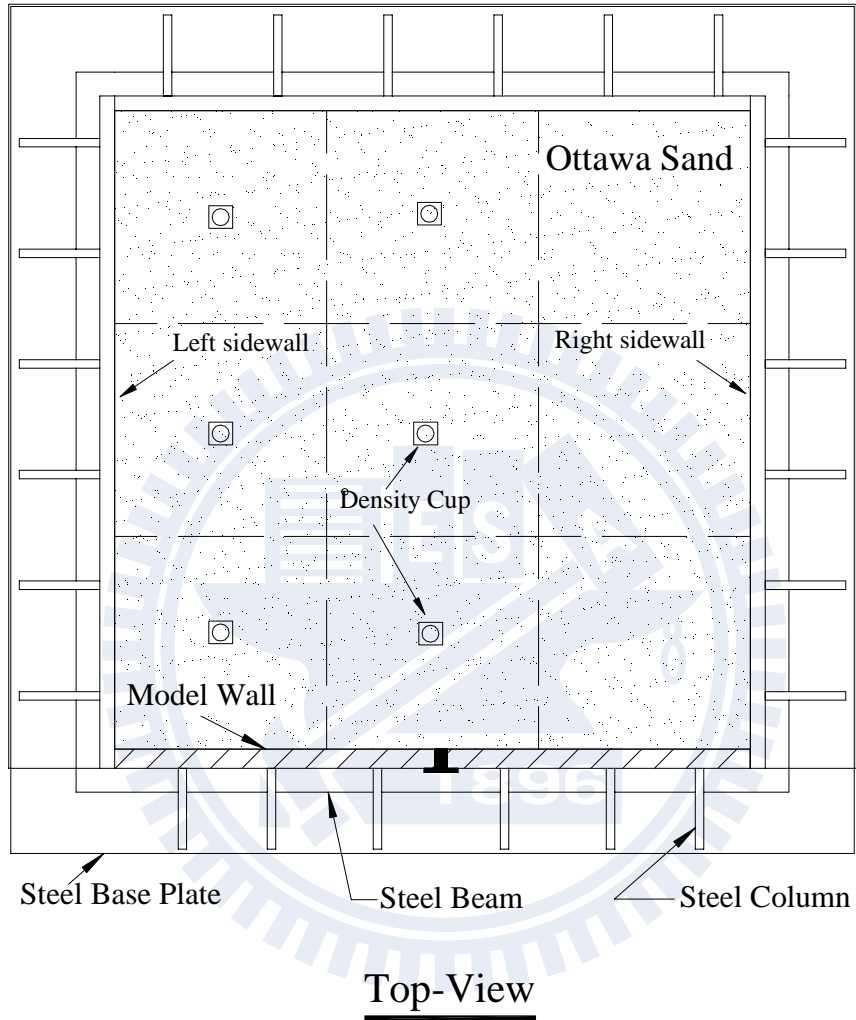
Fig. 4.15. Arrangement of Soil Density Cups at Same Elevation
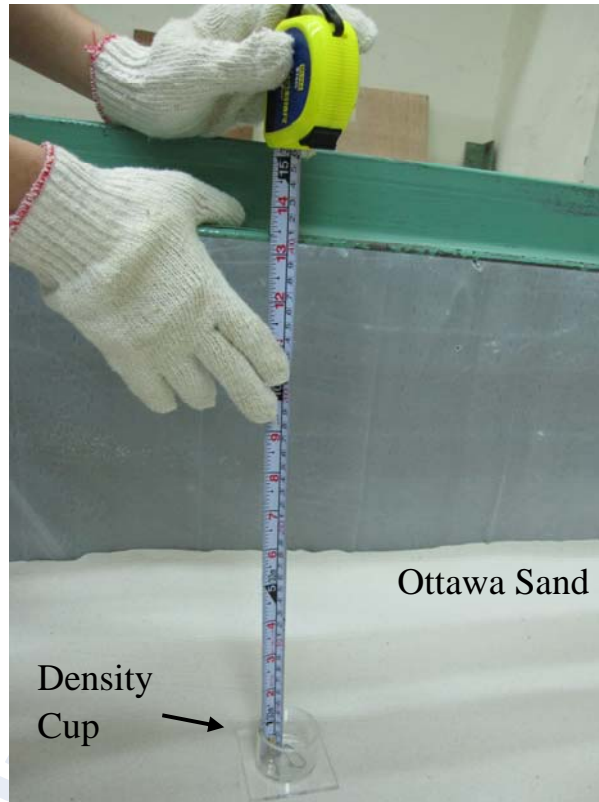
(a)

(b)

Fig. 4.16. Density Control Test (a) Placement of Density Cup;
(b) Measurement of Soil Mass in Cup
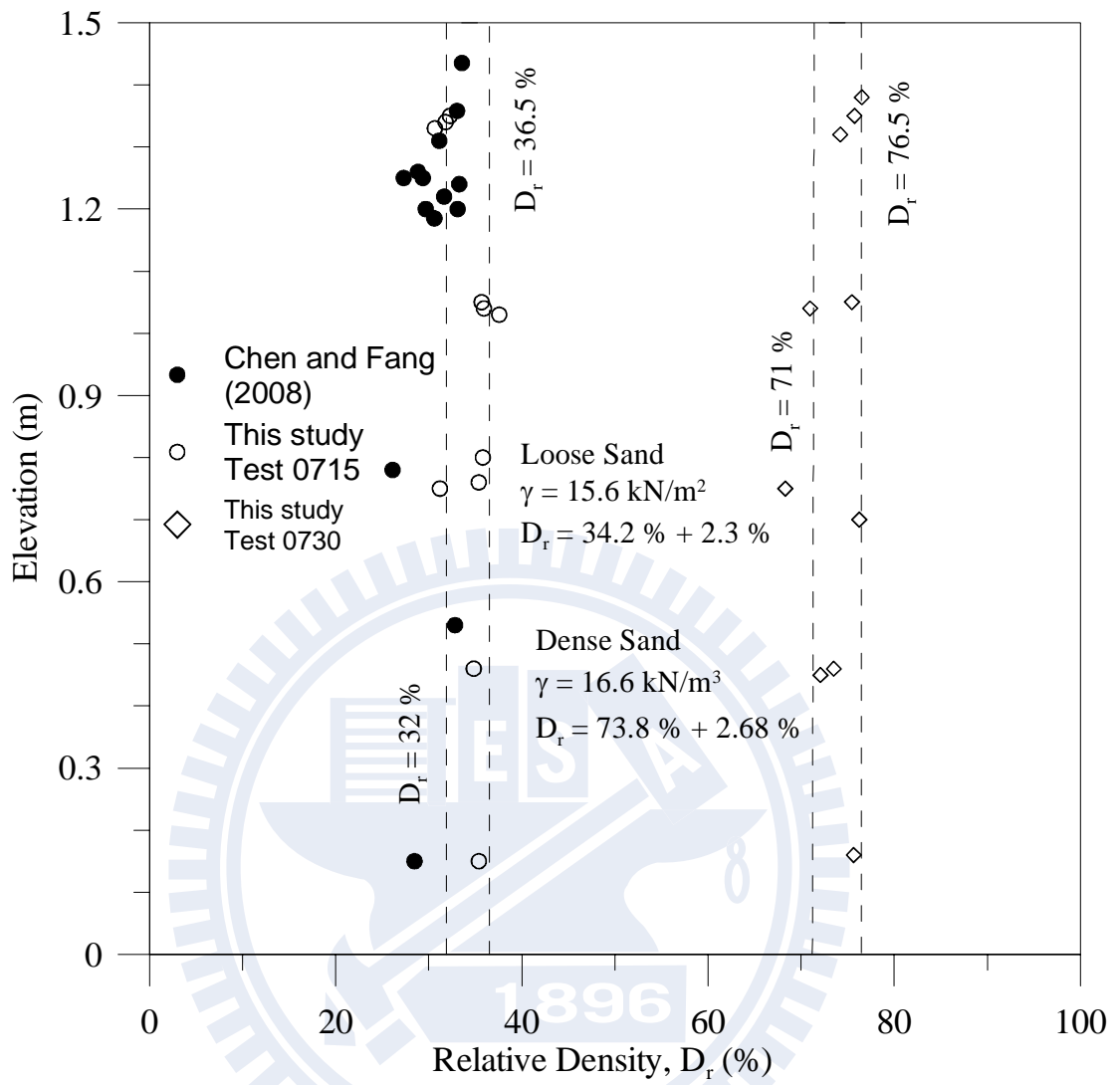
Fig. 4.17. Distribution of Soil Density
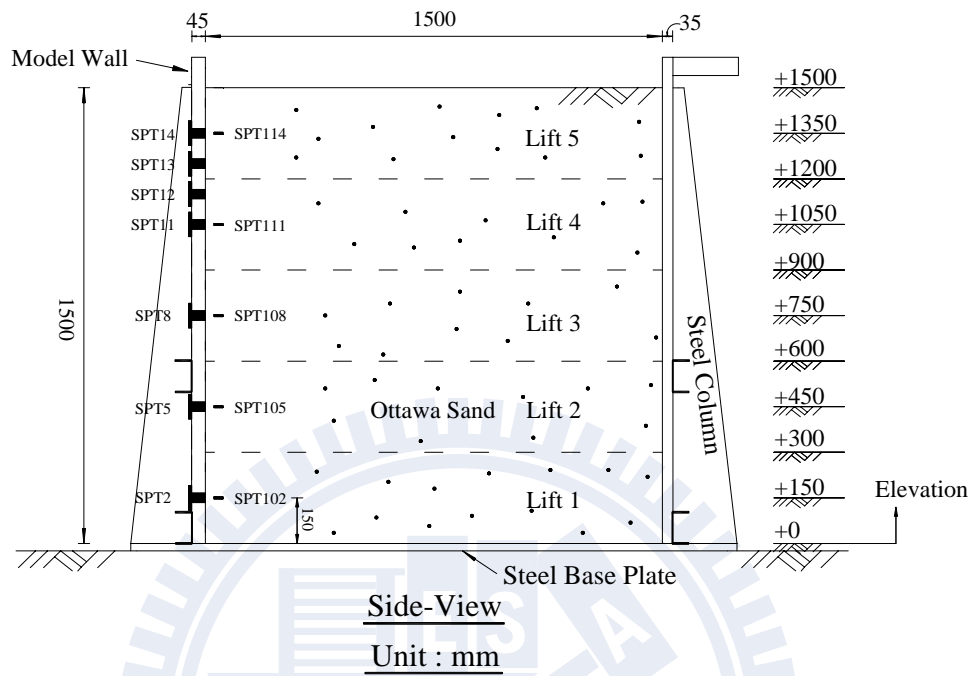
Fig. 5.1. Locations of SPT to Measure Distribution of Earth Pressure
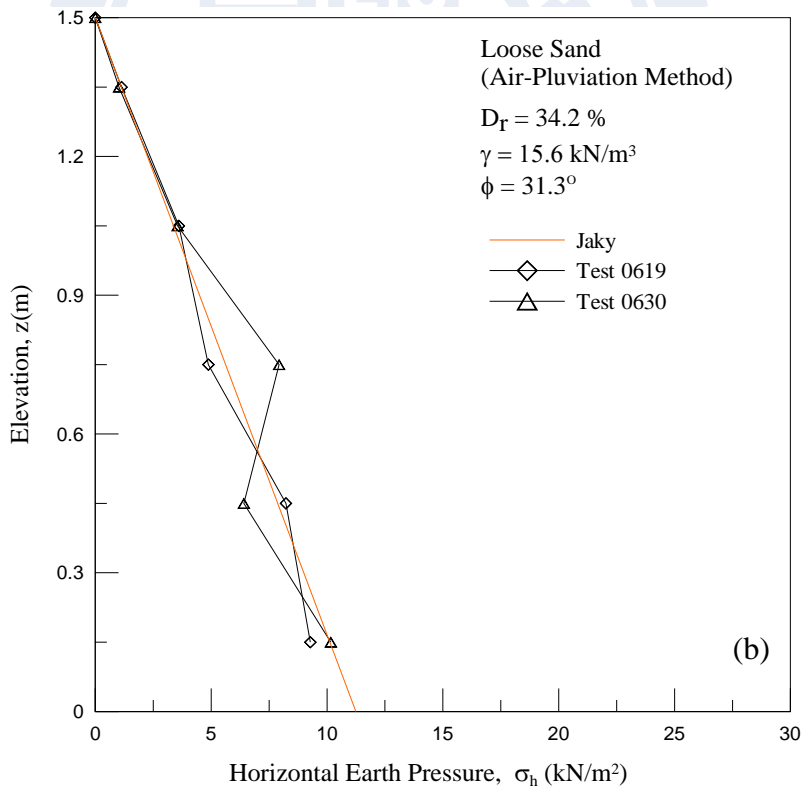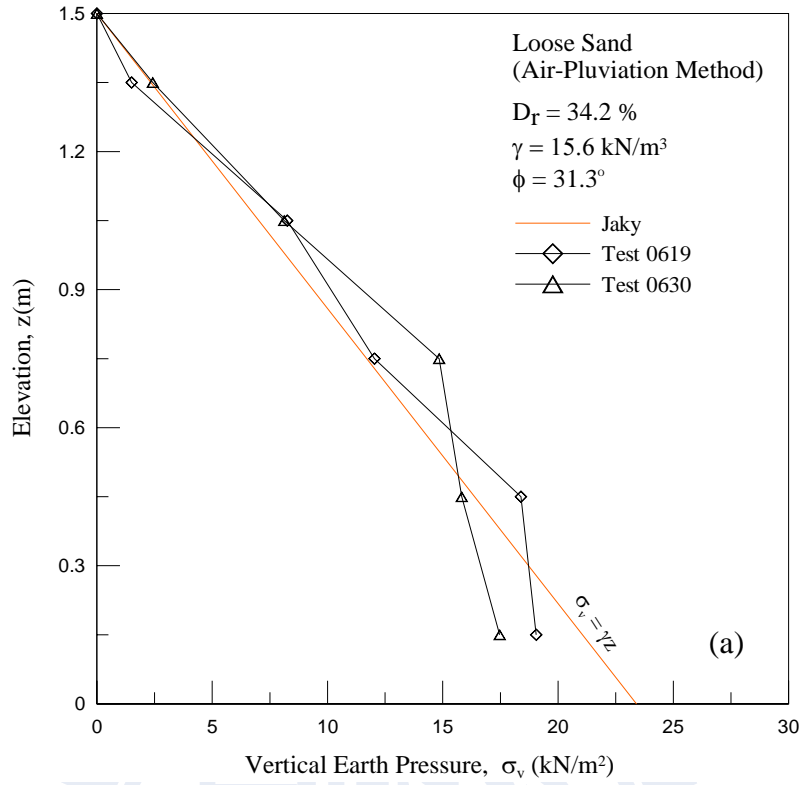
Fig. 5.2. (a) Distribution of vertical earth pressure with depth;
(b) Distribution of horizontal earth pressure
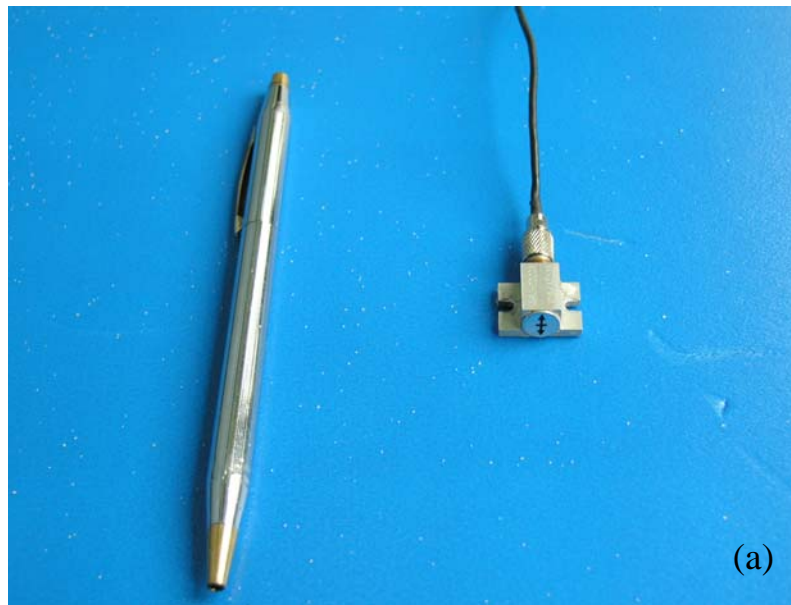
Fig. 5.3. Photograph of Accelerometer
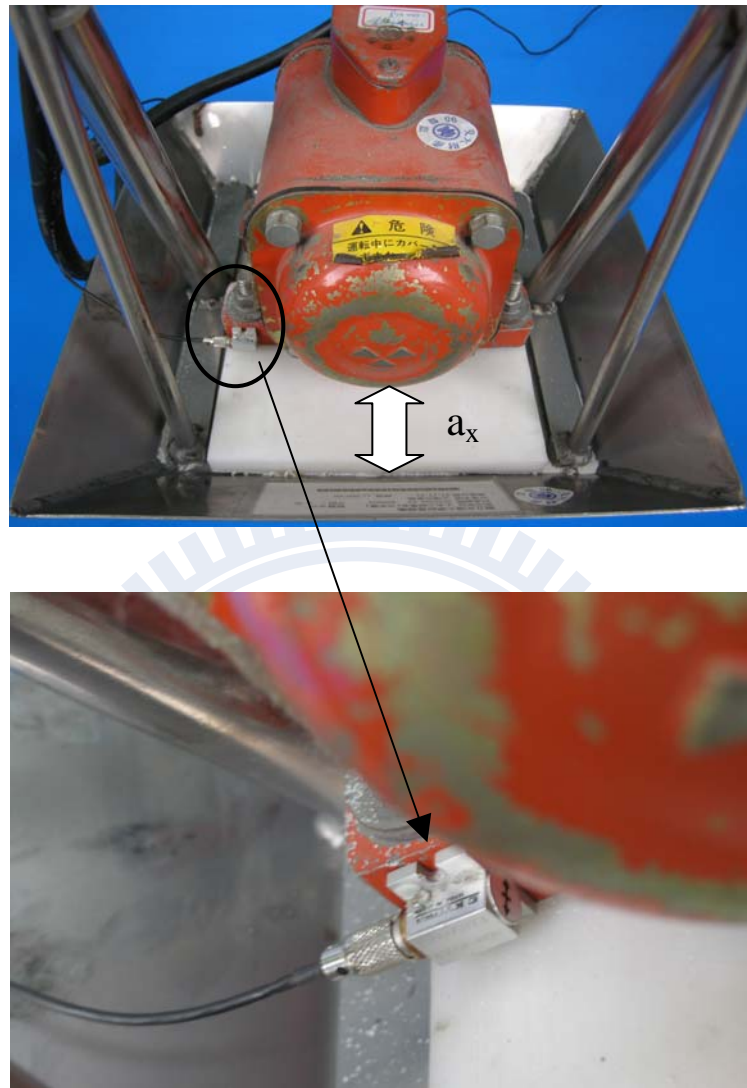
Fig. 5.4. Location of accelerometer to measure a_x (m/s^2)
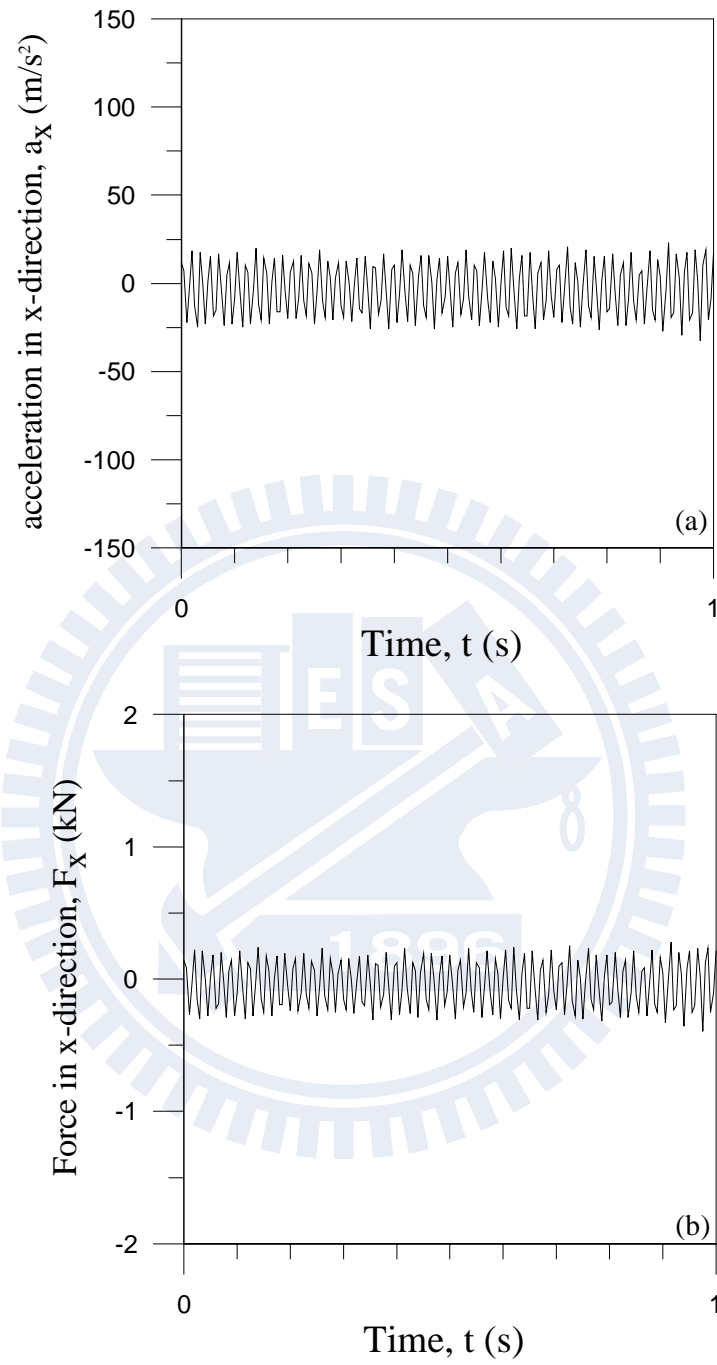
Fig. 5.5 (a) Acceleration in x-direction;
(b) Force in x-direction.
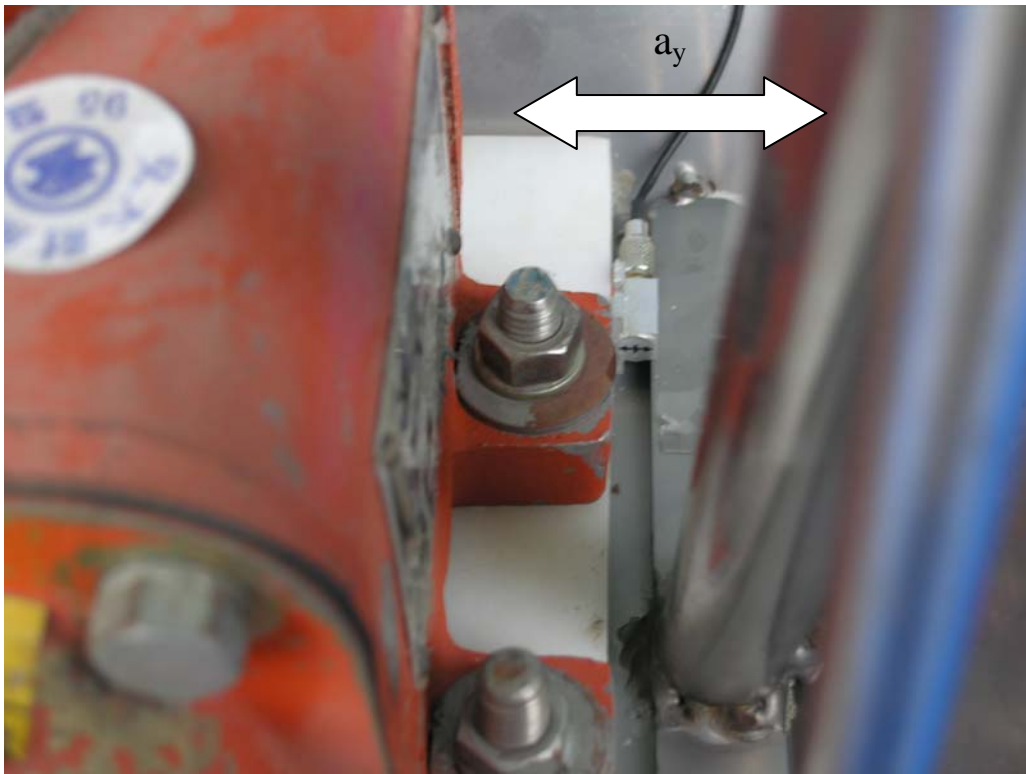
Fig. 5.6. Location of accelerometer to measure a_y (m/s^2)
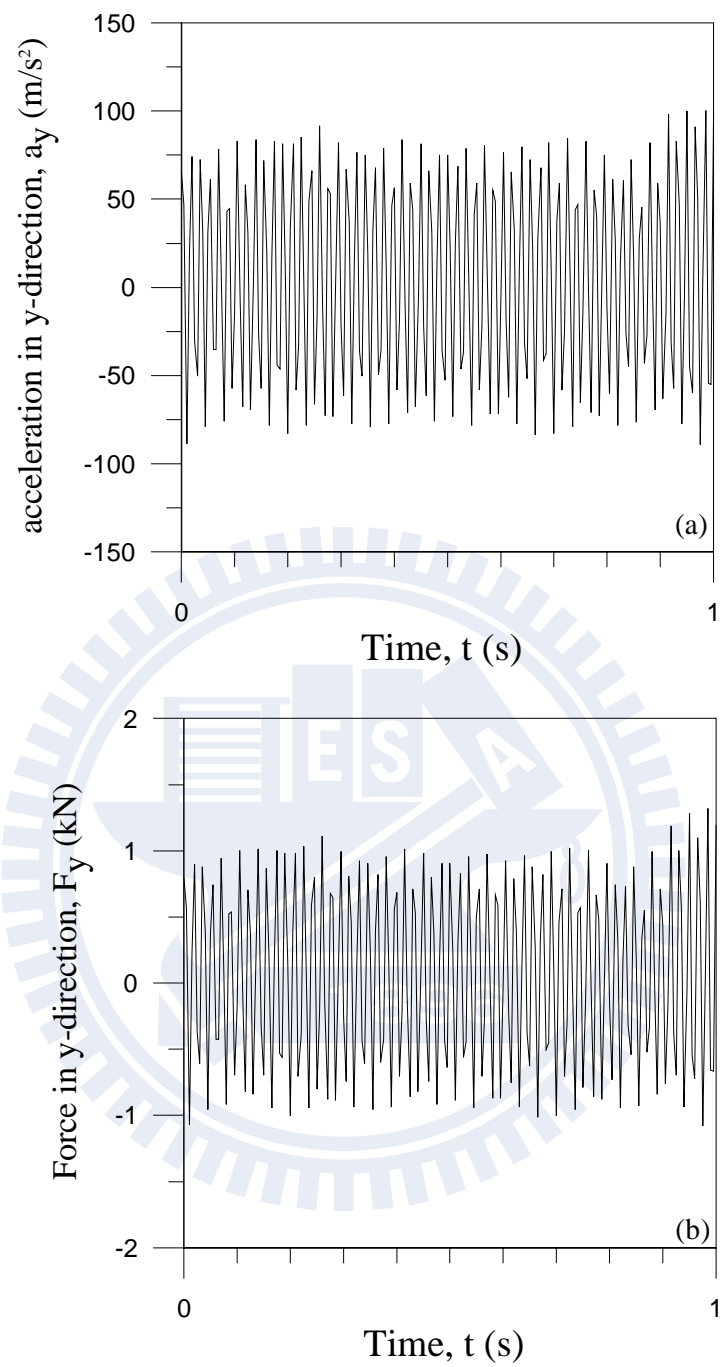
Fig. 5.7 (a) Acceleration in y-direction;
(b) Force in y-direction.

85

Fig. 5.8. Location of accelerometer to measure a_z
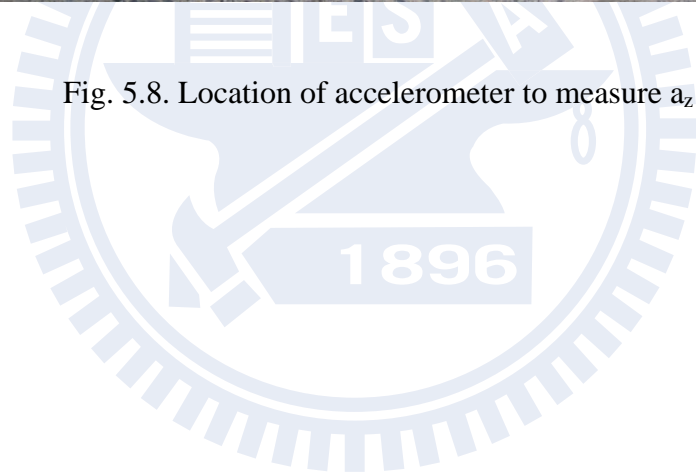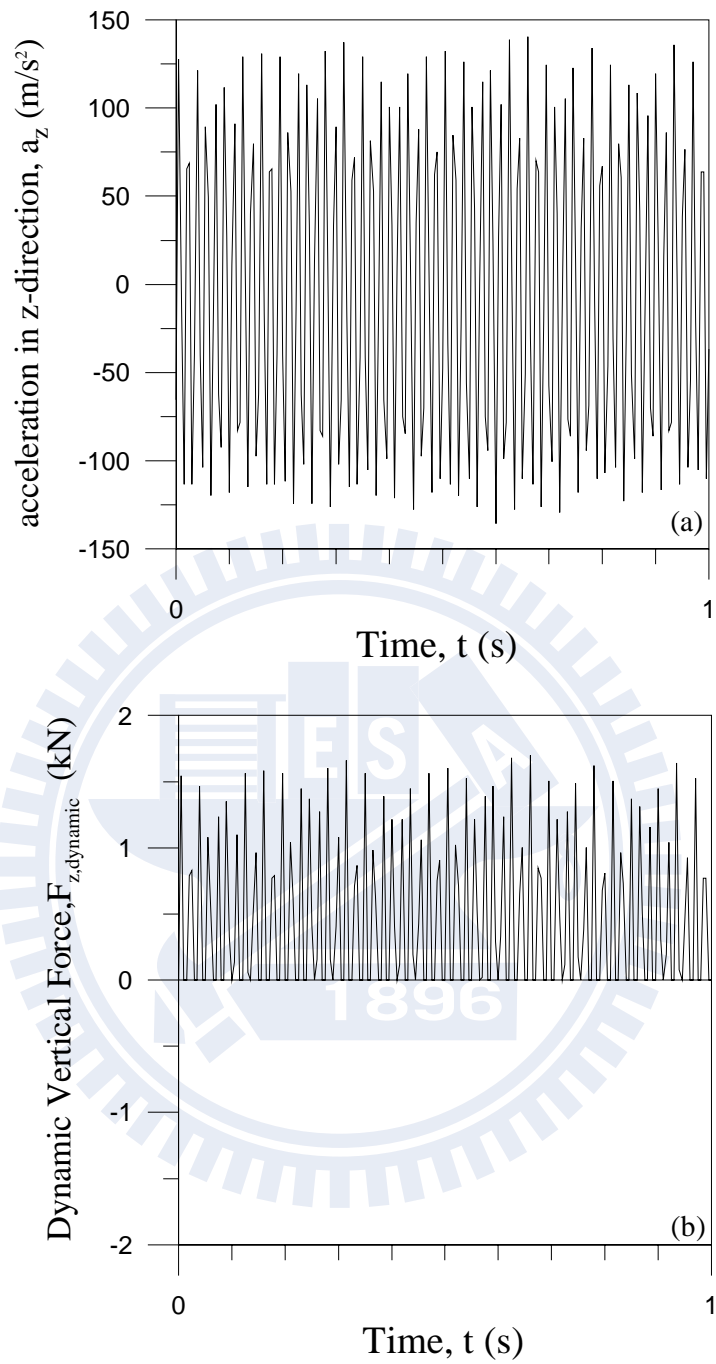
Fig. 5.9 (a) Acceleration in z-direction;
(b) Dynamic vertical force.

87
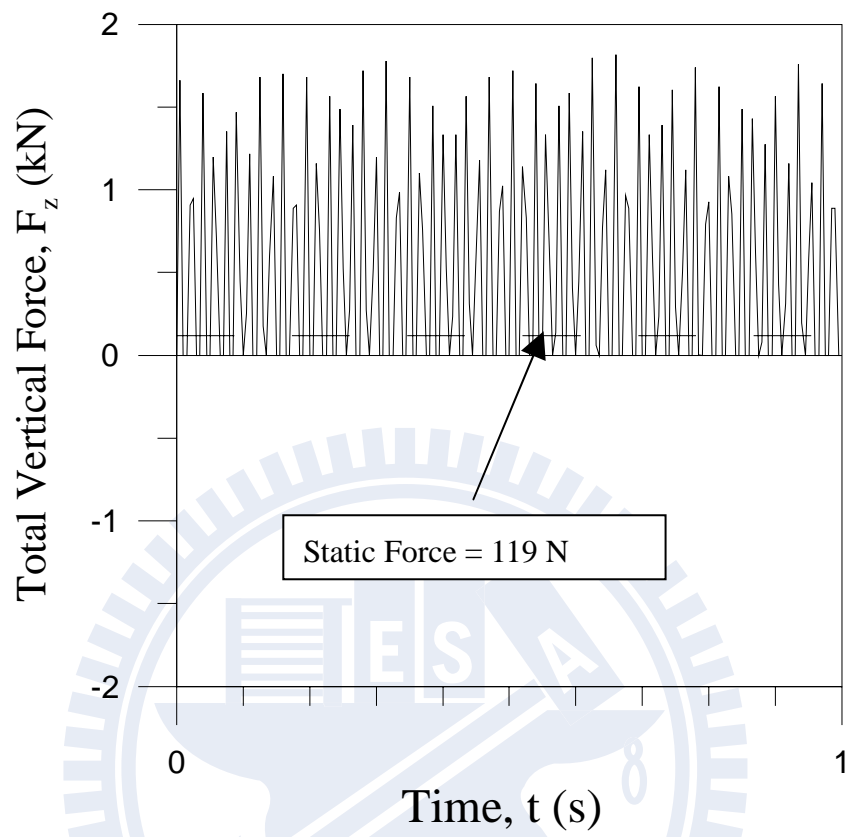
Fig. 5.10. Total force in vertical direction.
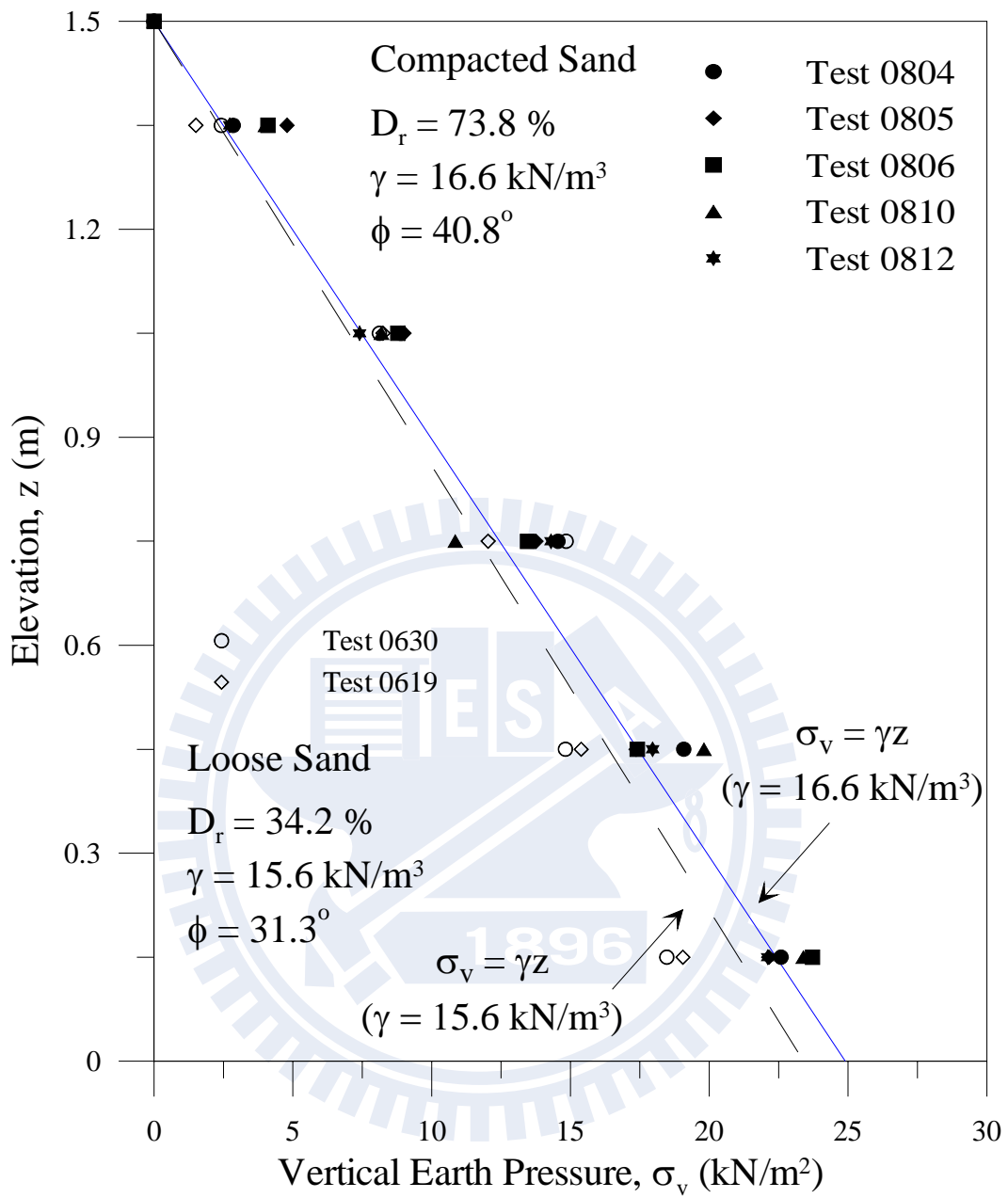
Fig. 5.11. Distribution of vertical earth pressure in soil mass.
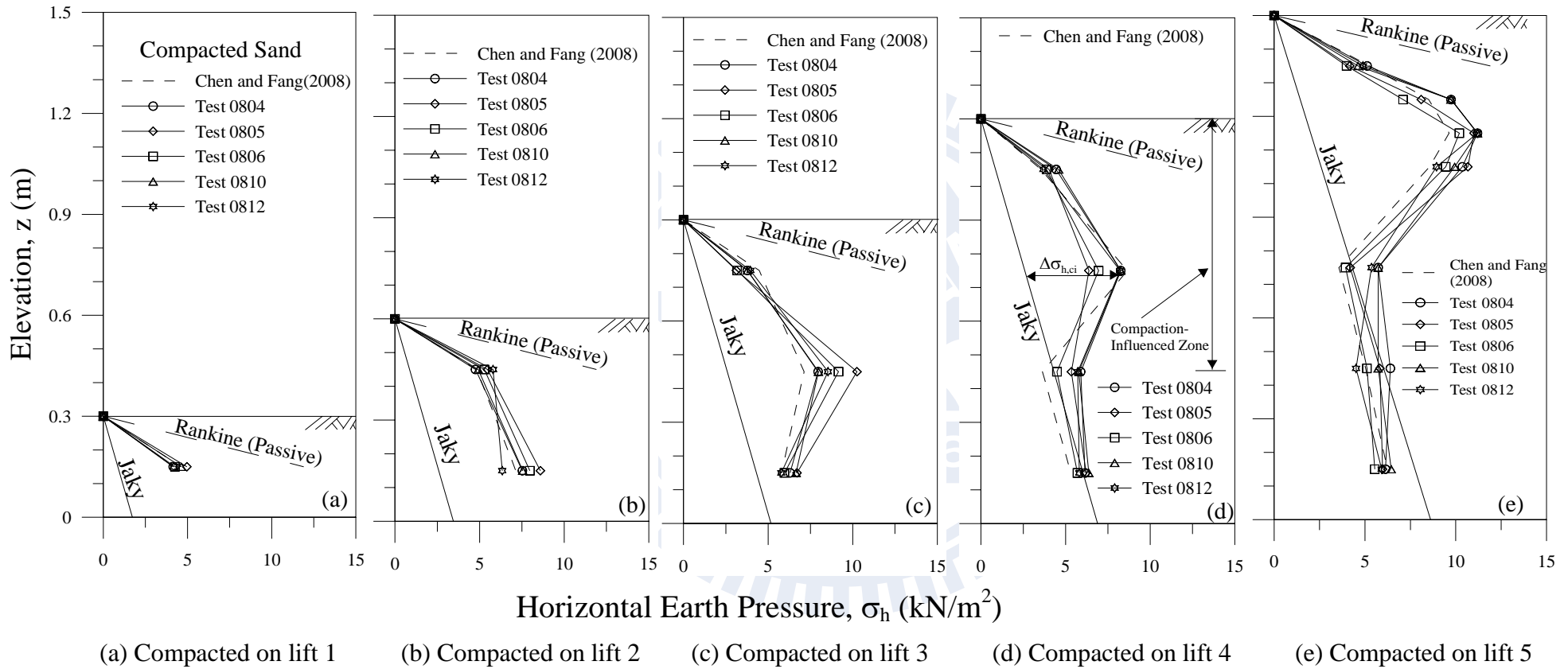
Fig. 5.12. Distribution of horizontal earth pressure in compacted sand

(a) Compacted on lift 1 (b) Compacted on lift 2 (c) Compacted on lift 3 (d) Compacted on lift 4 (e) Compacted on lift 5
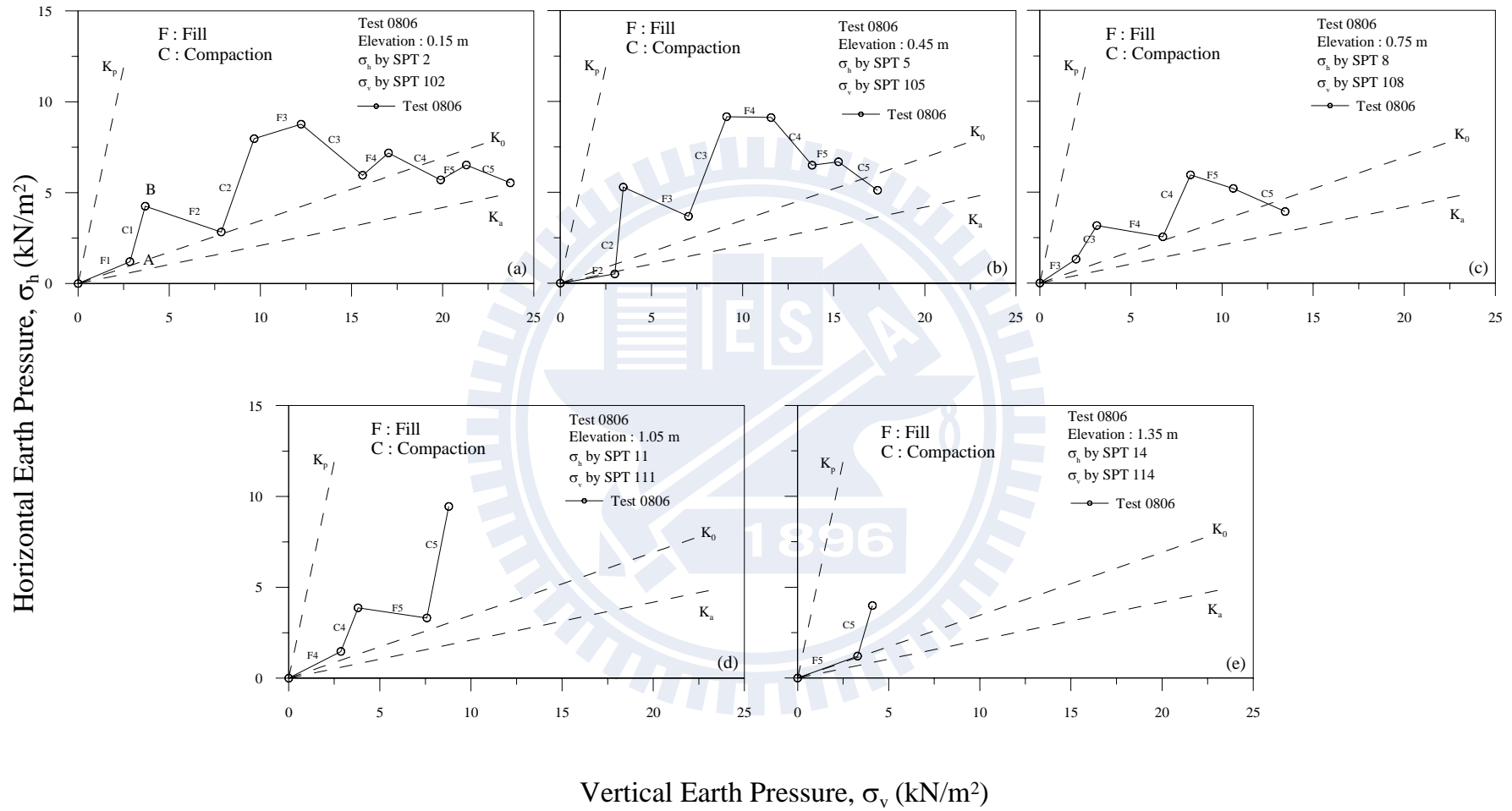
Fig.5.13. Static stress paths for soil element under filling and compaction of backfill (Test 0806)
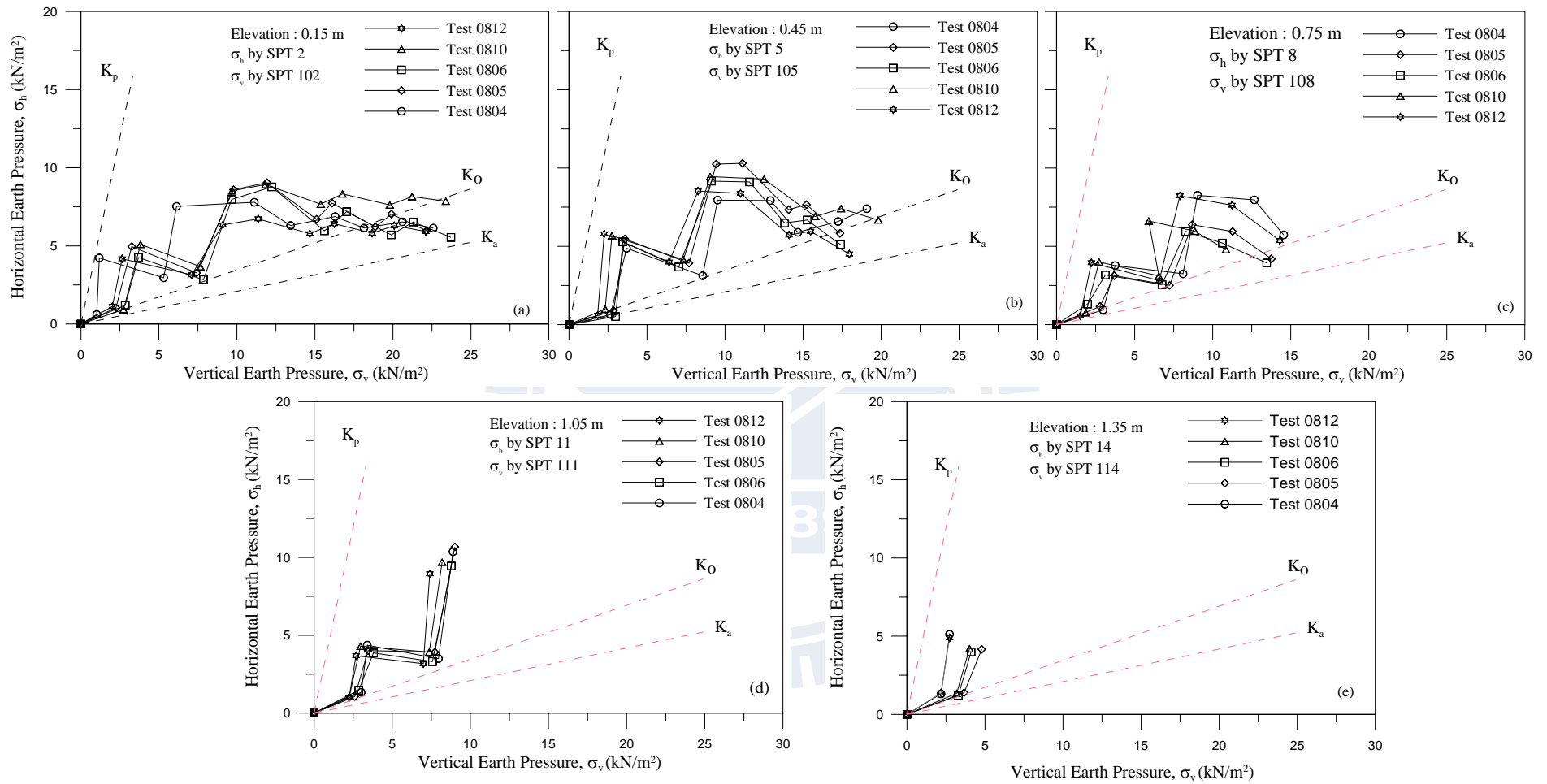
Fig.5.14. Comparison of stress paths for soil element under filling and compaction of backfill

92
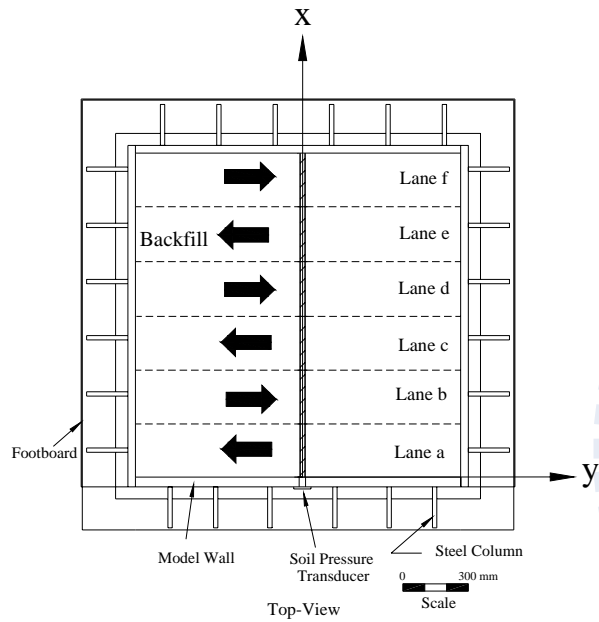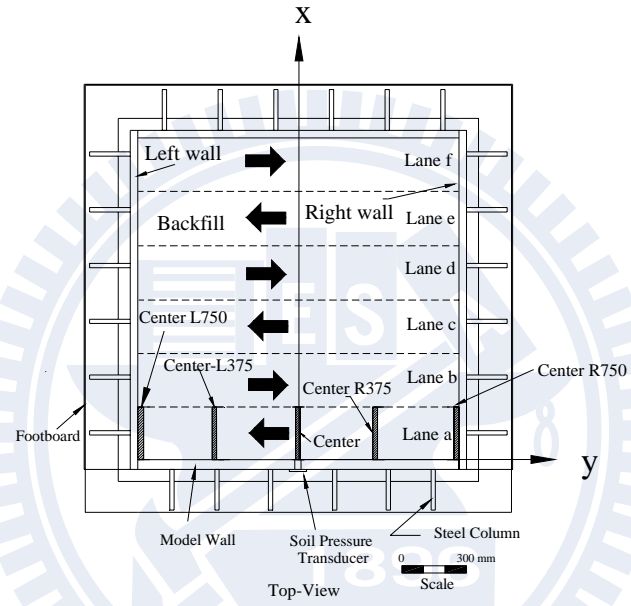
(a) Compaction approaching SPT in x-direction (b) Compaction passing SPT in y-direction (c) Compaction rising in z-direction
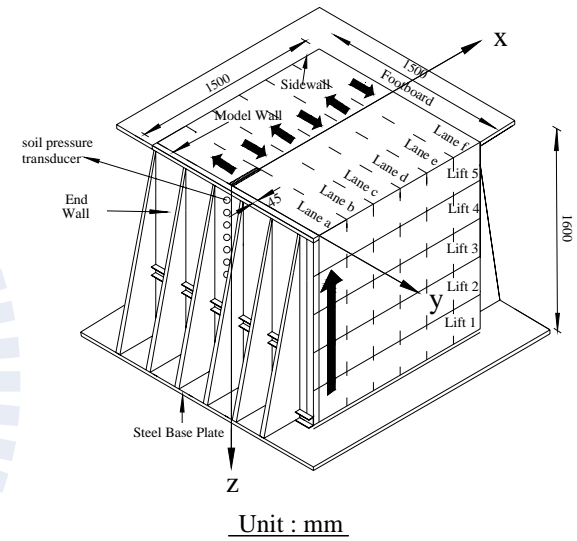
Fig. 5.15 Different direction for consider compaction-induced stress paths
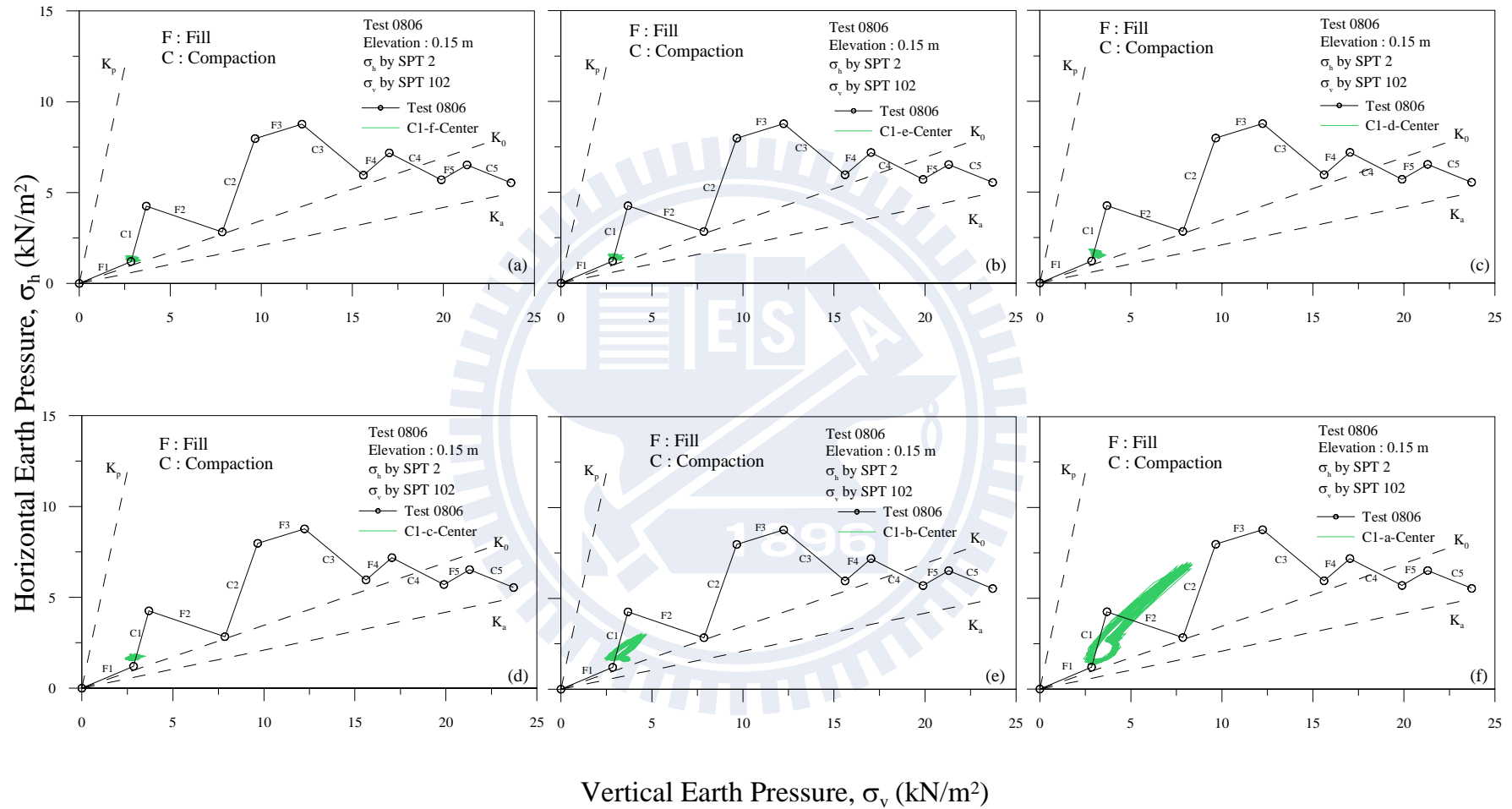
Fig. 5.16. Stress paths measured at center part of the model wall by SPT2 and SPT102 due to compaction on lift 1 from Lane f to Lane a
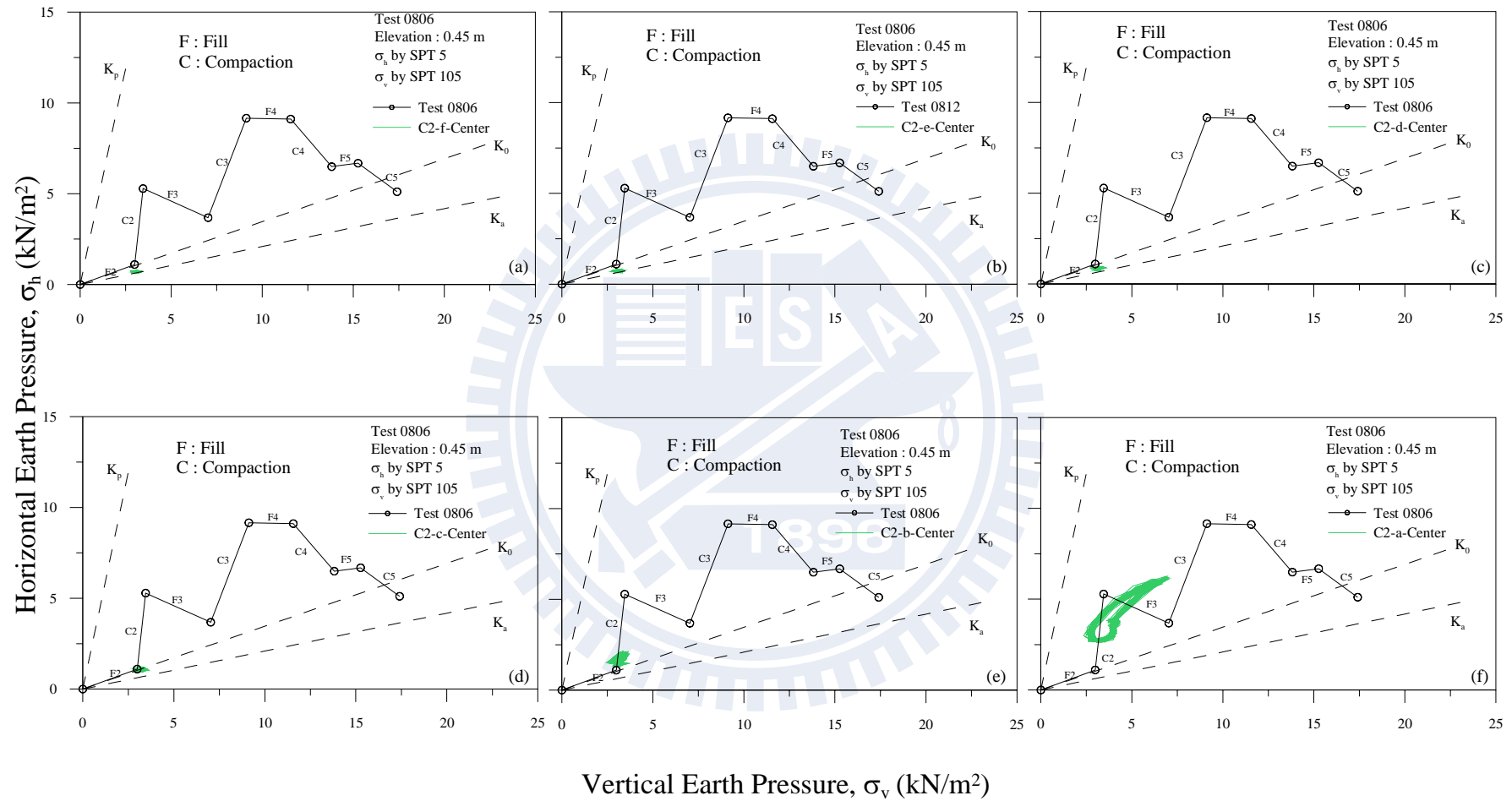
Fig. 5.17. Stress paths measured at center part of the model wall by SPT5 and SPT105 due to compaction on lift 2 from Lane f to Lane a
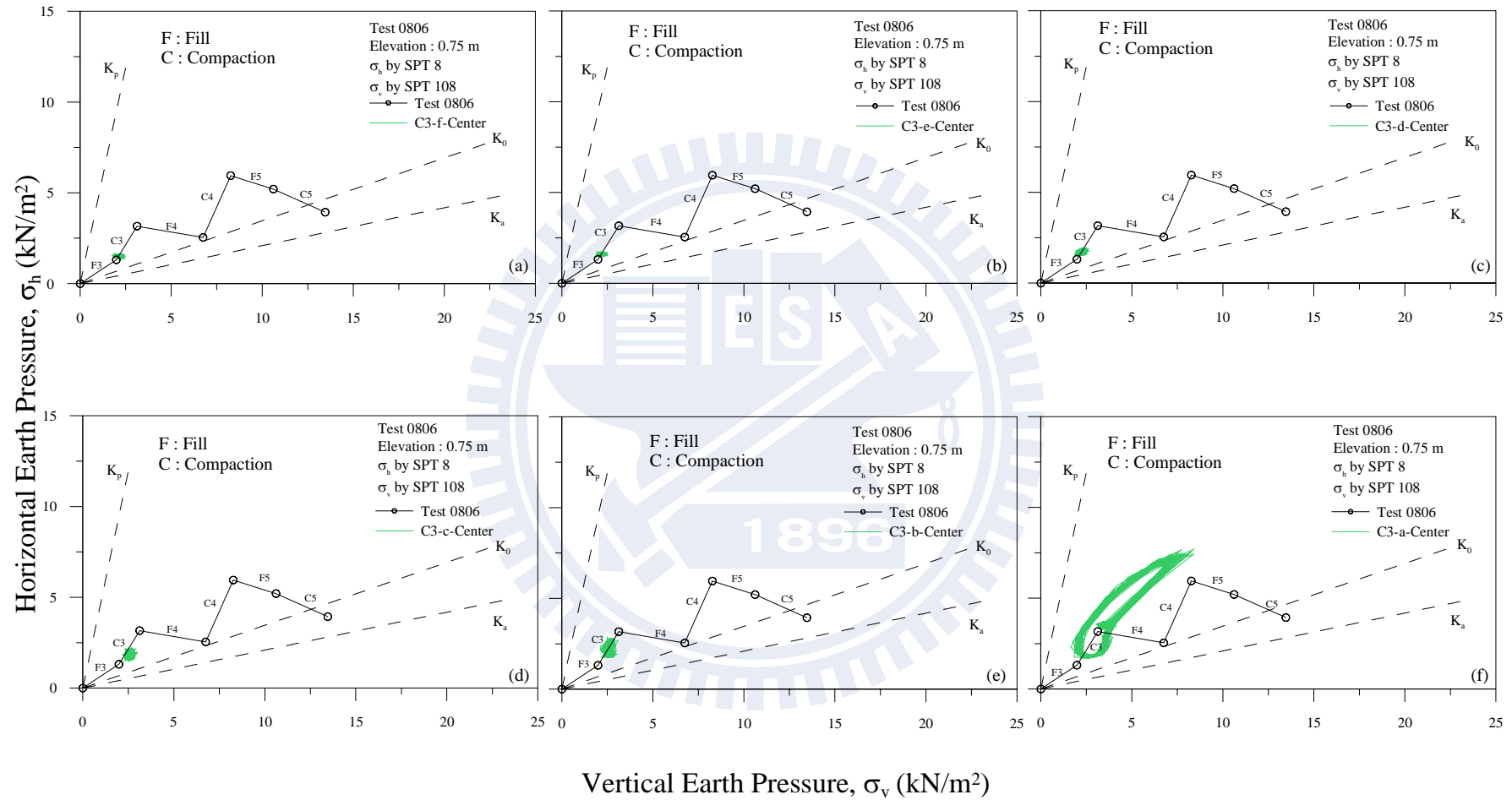
Fig. 5.18. Stress paths measured at center part of the model by SPT8 and SPT108wall due to compaction on lift 3 from Lane f to Lane a
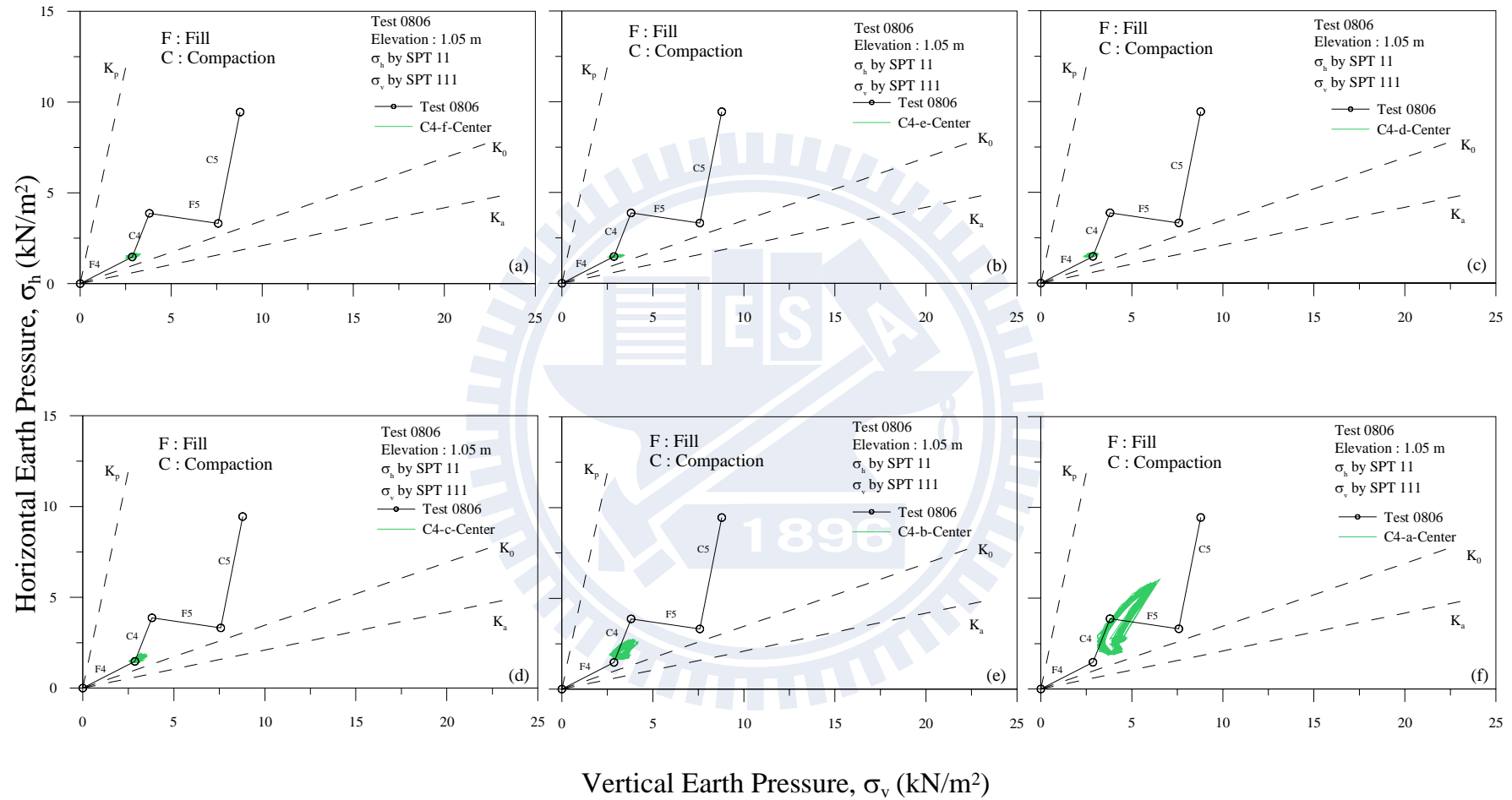
Fig. 5.19. Stress paths measured at center part of the model wall by SPT11 and SPT111 due to compaction on lift 4 from Lane f to Lane a
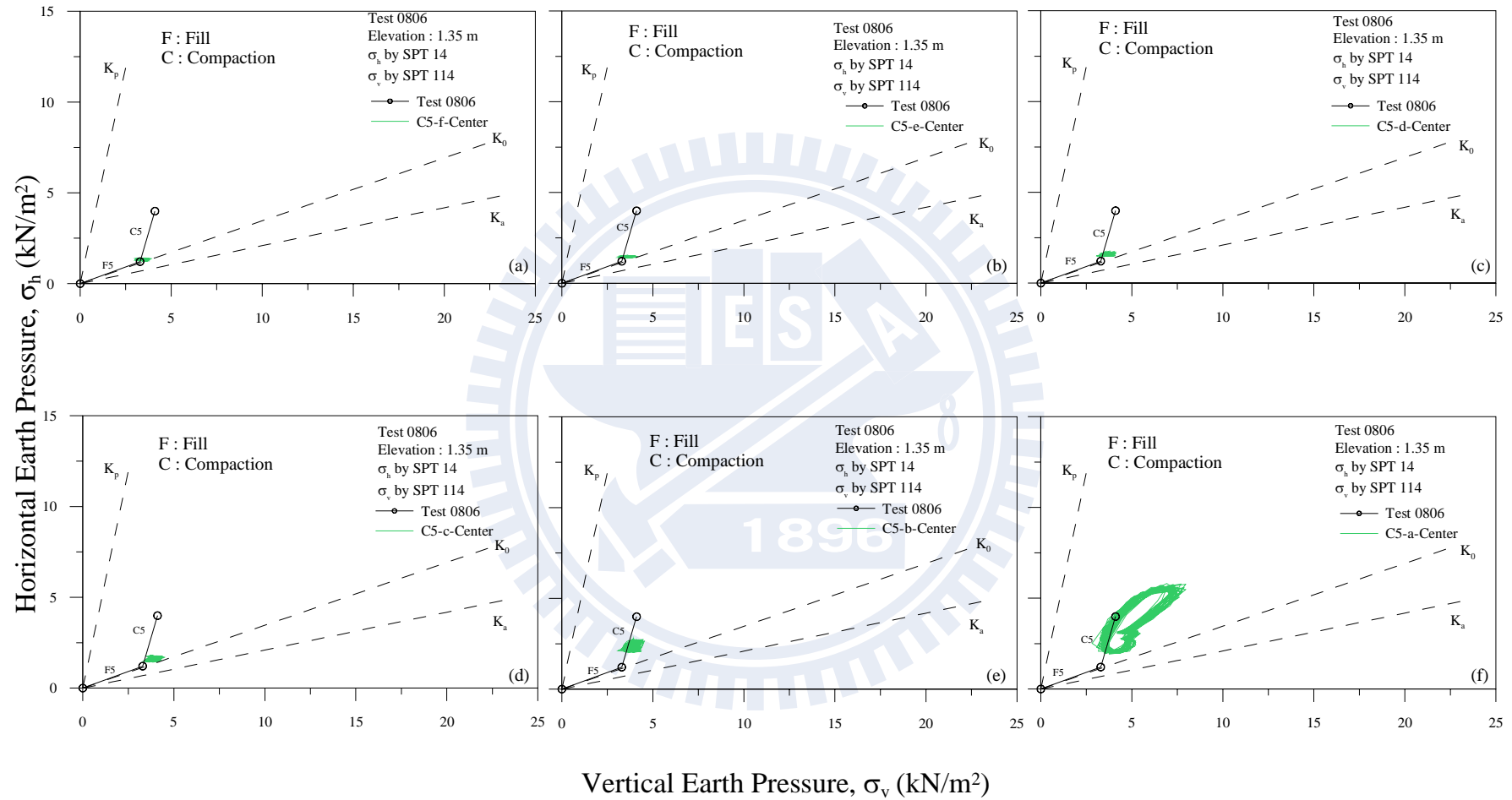
Fig. 5.20. Stress paths measured at center part of the model wall by SPT14 and SPT114 due to compaction on lift 5 from Lane f to Lane a
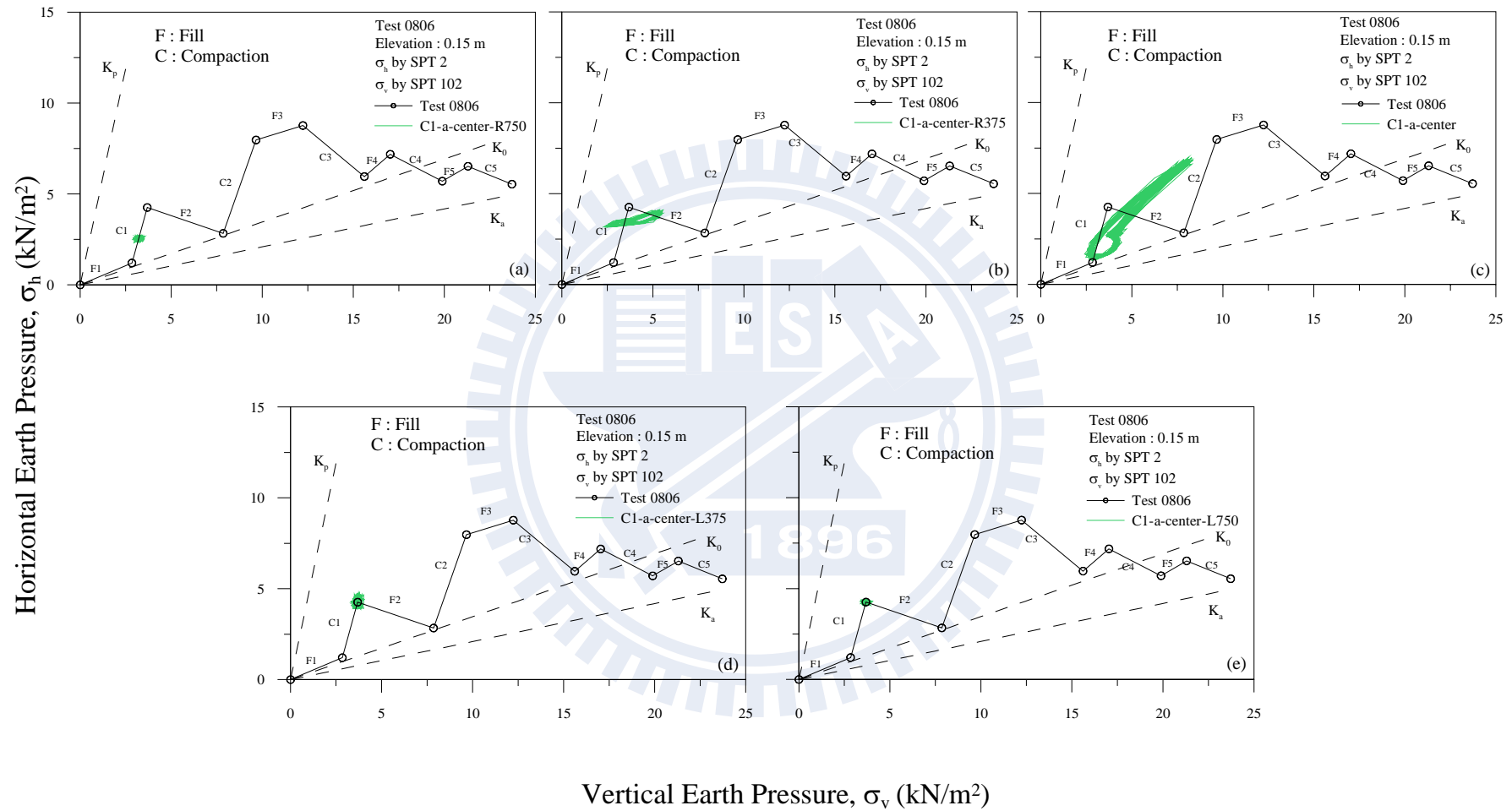
Fig. 5.21. Stress paths measure at SPT2 and SPT102 due to compaction on Lane (near the wall) of Lift 1 from R750 to L750
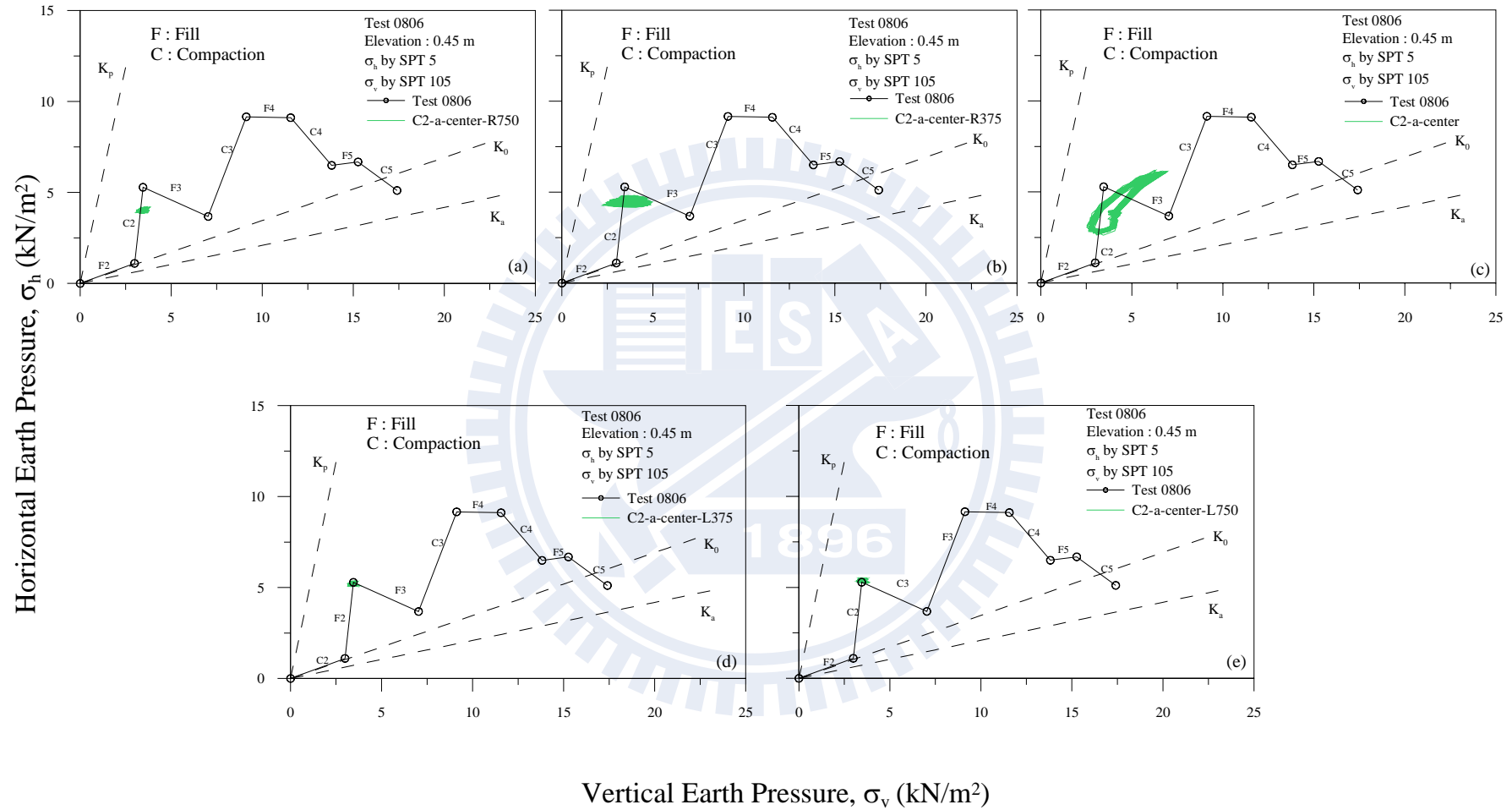
Fig. 5.22. Stress paths measure at SPT5 and SPT105 due to compaction on Lane (near the wall) of Lift 2 from R750 to L750
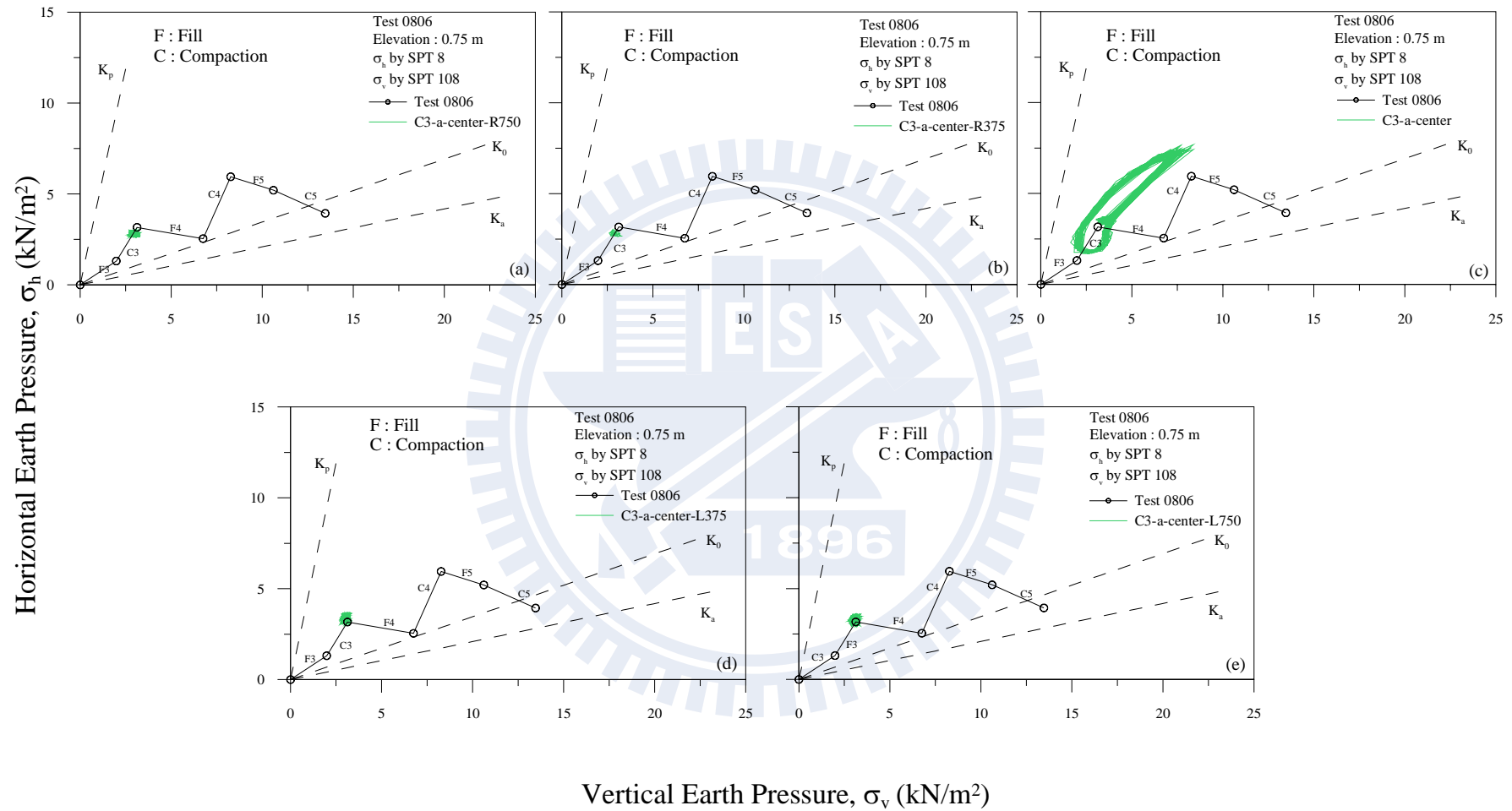
Fig. 5.23. Stress paths measure at SPT8 and SPT108 due to compaction on Lane (near the wall) of Lift 3 from R750 to L750
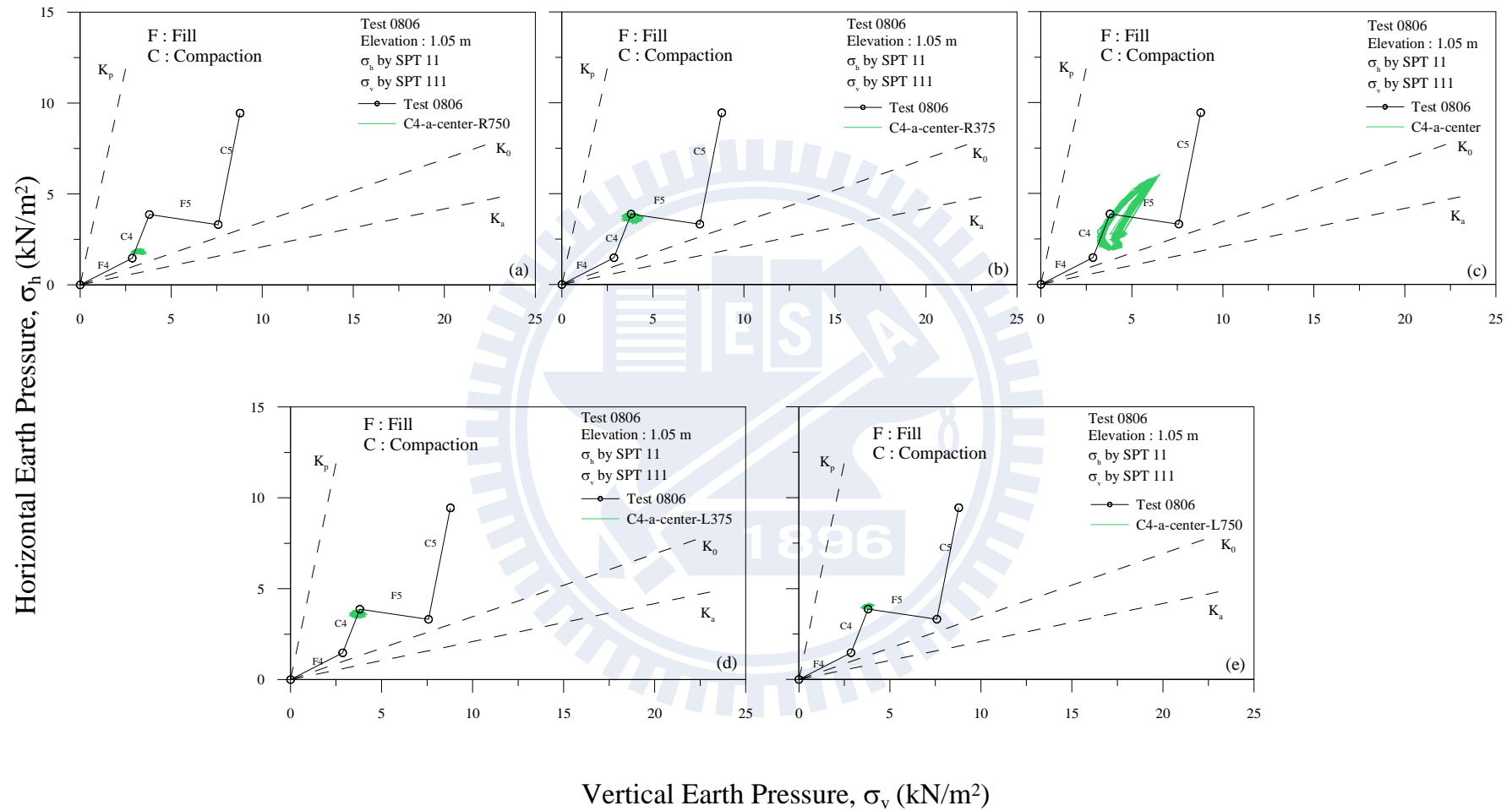
Fig. 5.24. Stress paths measure at SPT11 and SPT111 due to compaction on Lane (near the wall) of Lift 4 from R750 to L750
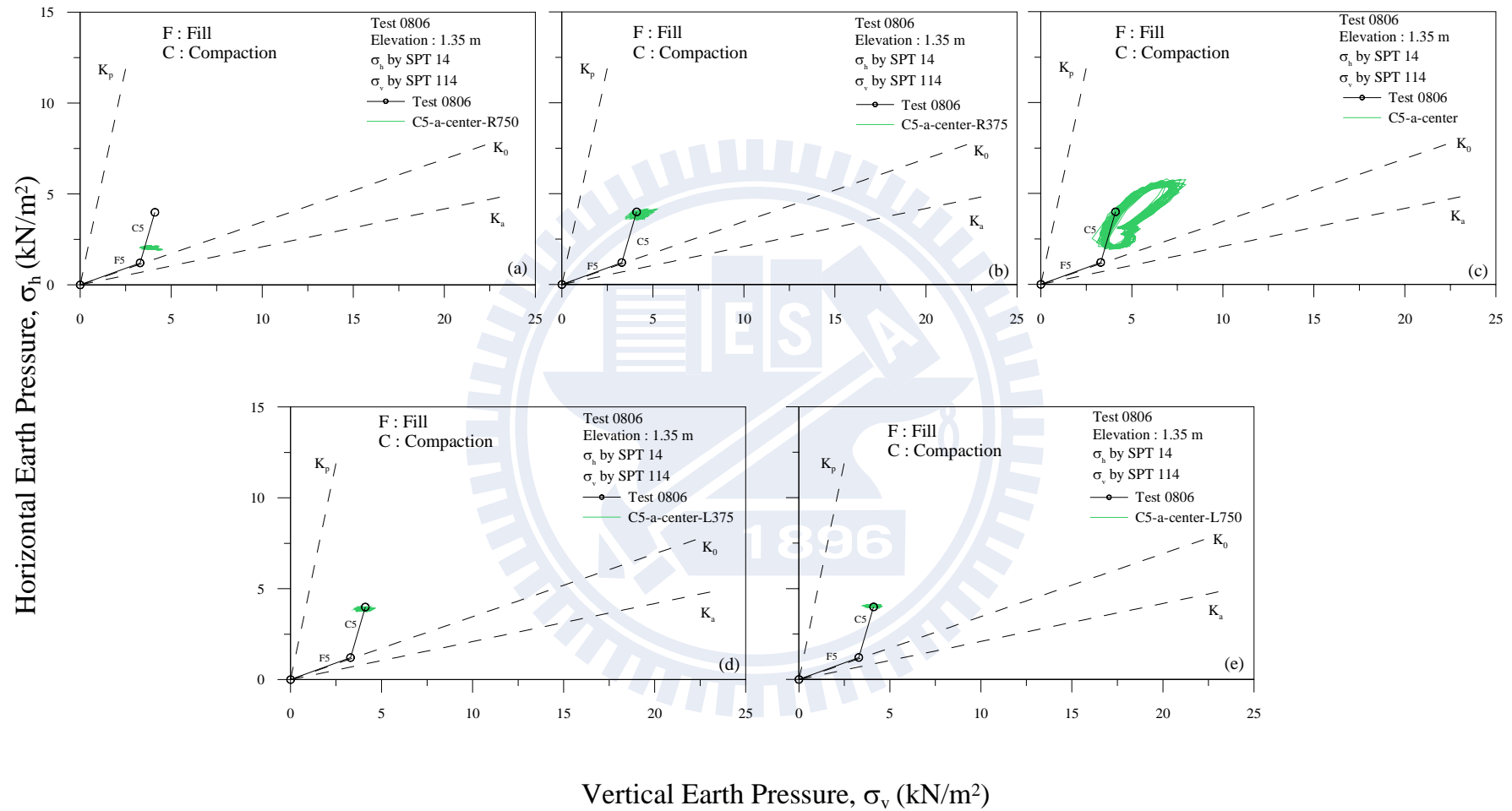
Fig. 5.25. Stress paths measure at SPT14 and SPT114 due to compaction on Lane (near the wall) of Lift 5 from R750 to L750
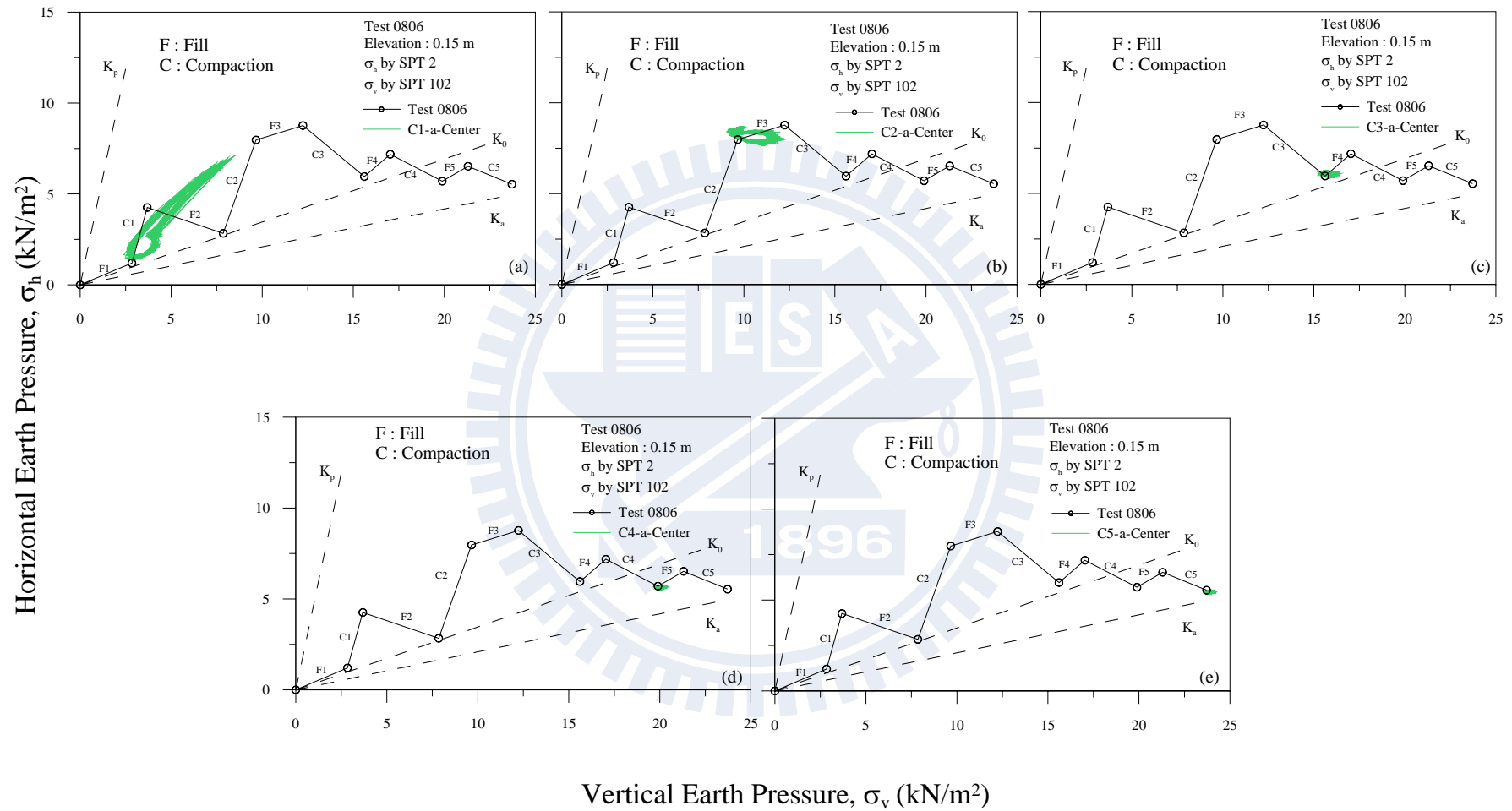
Fig. 5.26. Stress paths measure at SPT2 and SPT102 due to compaction on center part of Lane a (near the wall) of Lift 1 to Lift 5
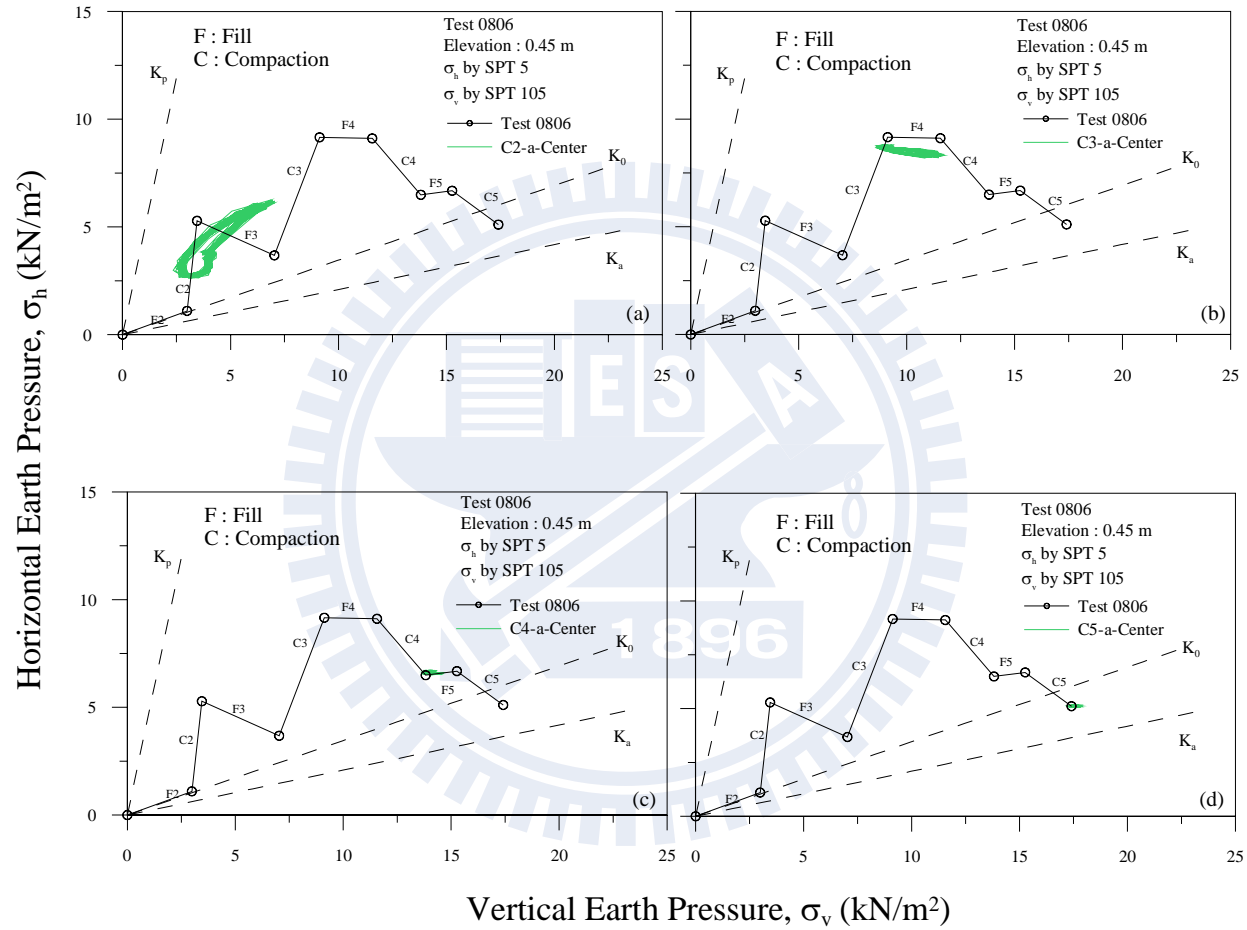
Fig. 5.27. Stress paths measure at SPT5 and SPT105 due to compaction on center part of Lane a (near the wall) of Lift 2 to Lift 5
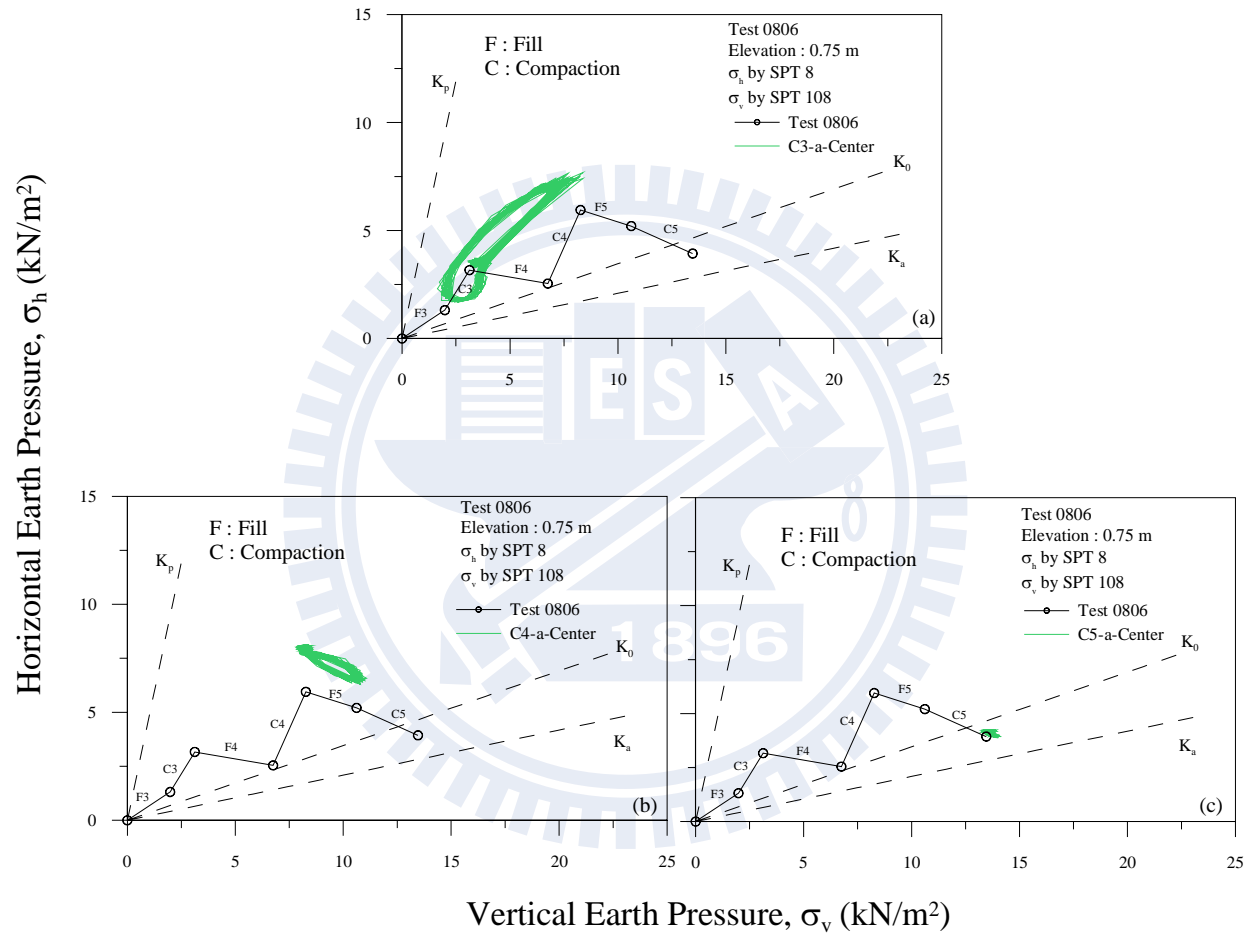
Fig. 5.28. Stress paths measure at SPT8 and SPT108 due to compaction on center part of Lane a (near the wall) of Lift 3 to Lift 5
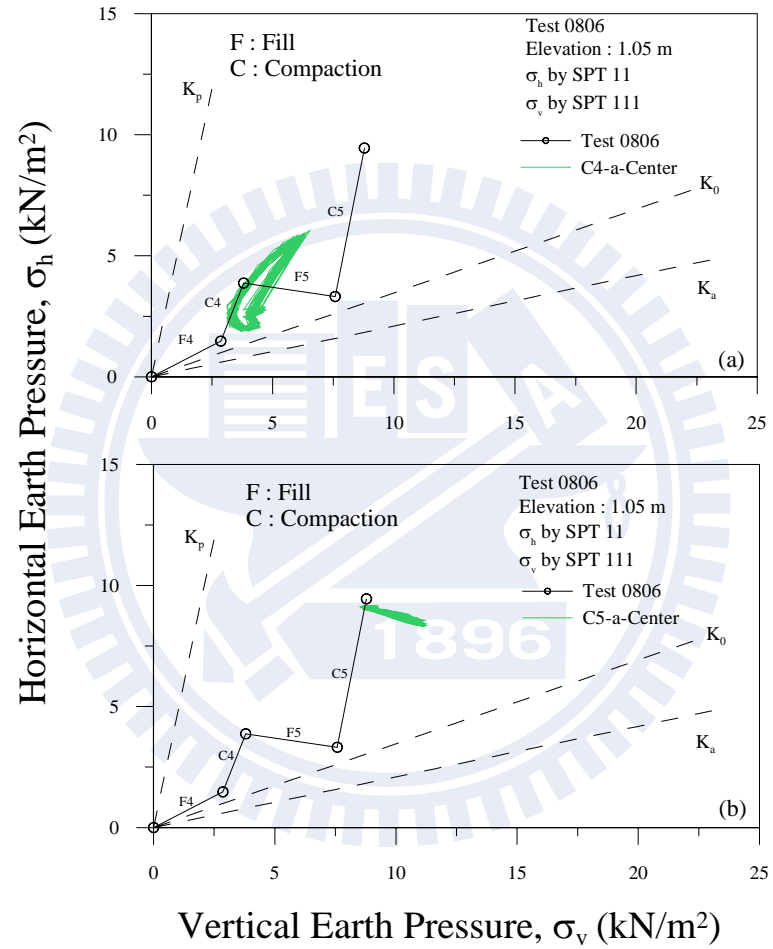
Fig. 5.29. Stress paths measure at SPT11 and SPT111 due to compaction on center part of Lane a (near the wall) of Lift 4 to Lift 5
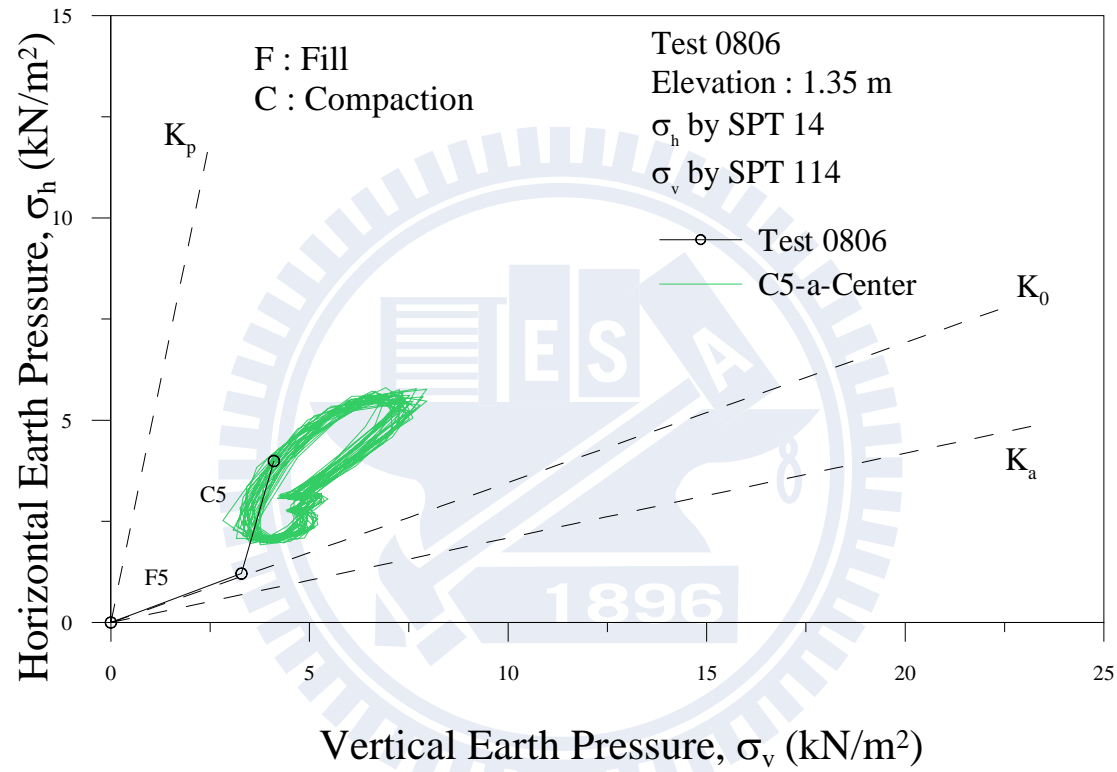
Fig. 5.30. Stress paths measure at SPT14 and SPT114 due to compaction on center part of Lane a (near the wall) of Lift 5
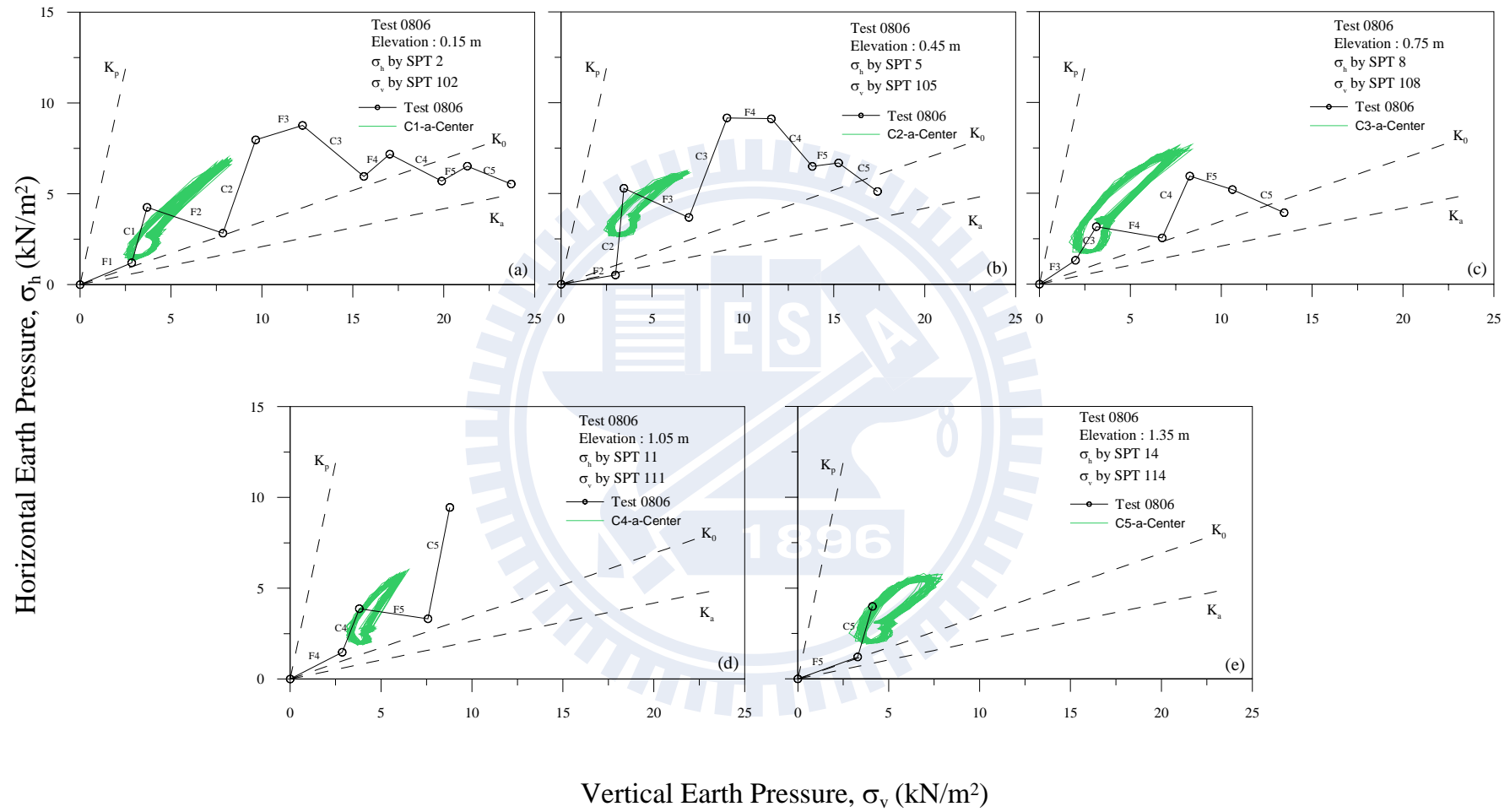
Fig. 5.31. Stress paths due to compaction at center of Lane a (near the wall) for Lift 1 to Lift 5 (Test 0806)
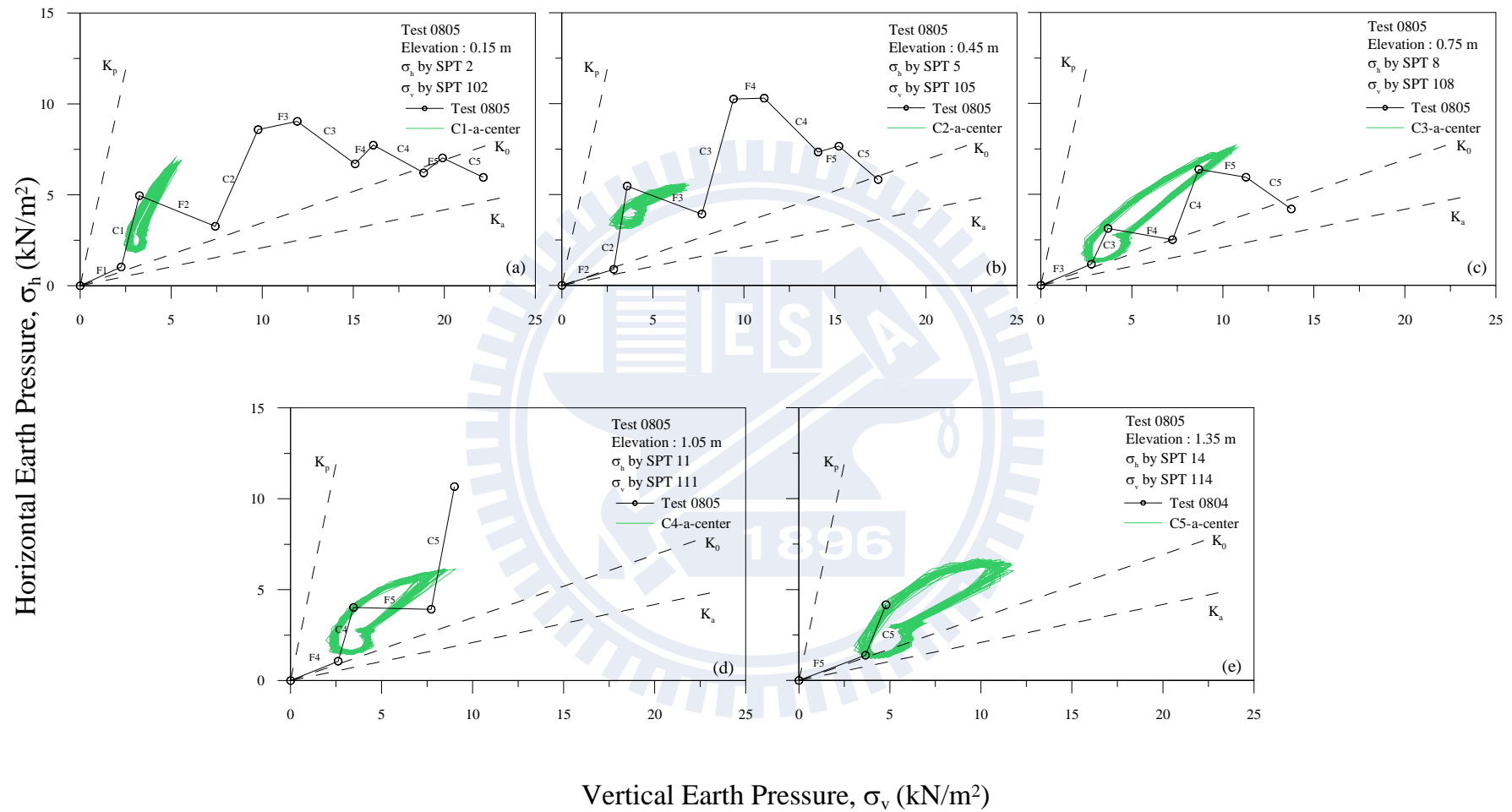
Fig. 5.32. Stress paths due to compaction at center of Lane a (near the wall) for Lift 1 to Lift 5 (Test 0805)
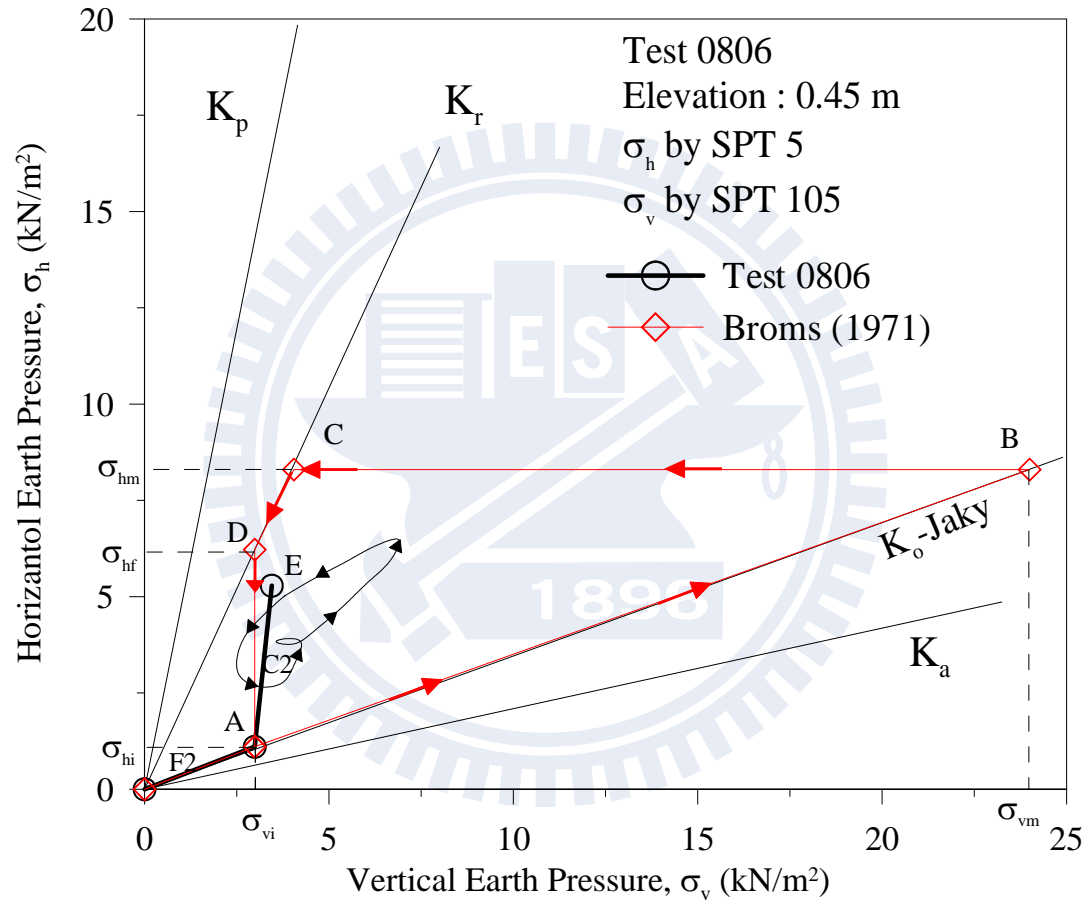
Fig. 5.33. Comparison of theoretical and experimental stress paths

Appendix A

CALIBRATION OF SOIL PRESSURE TRANSDUCERS

To investigate the vertical and horizontal earth pressure in the backfill, two types of strain-gage type soil pressure transducers (SPT) were used. The transducers BE-2KCM17, PGM-02KG manufactured by KYOWA has effective diameter of 22 mm for type BE-2KCM17 and 12 mm for PGM-02KG. The type BE-2KCM17 was embedded in the backfill to monitor the earth pressure variation in the soil mass. Since the pressure acts between soil particles and the transducer is quite different from the pressure that acts between liquid and transducer, it is necessary to calibrate the transducer in an environment similar to that for the actual testing condition. Two systems were designed for the calibration of the on-wall and in soil transducers. These systems consist of the calibration device, air-pressure control system, signal conditioner, and data acquisition system, as indicated in Fig. A1 and Fig. A2. The typical photograph of the system is shown in Fig. A3.

The calibration devices shown in Fig.A3 is a shallow cylindrical chamber with an inner diameter of 400 mm and a height of 30 mm and is made of a solid steel plate, which is the same material as the model retaining wall. As shown in Fig. A1, it is important that the surface of the sensor was installed flush with the upper face of the chamber. To calibrate the in-soil transducer, as indicated in Fig. A2, a thin layer of sand was placed into the chamber to form a sand bed then the soil pressure transducer was placed on the sand bed. On top of the transducer, a 10 mm-thick sand layer was placed

in the calibration device. Then the 0.2 mm-thick rubber membrane was placed over the sandy layer. As indicated in Fig. A1 and Fig. A2, a uniformly distributed air-pressure was applied on the membrane, carried-over through the soil particles, and transmitted to the transducer.

In Fig. A1 and Fig. A2, rubber O-rings were arranged to prevent air leakage between the chamber and the cap. It should be noted that the air pressure applied for the calibration of transducer should be consistent with the operating pressure range for model wall experiments. For this study, the transducers were calibrated for the pressure range of 0 ~ 9.81 kN/m^2 or 0 ~ 98.1 kN/m^2 depending on the type of soil pressure transducer. To reduce the effect of sidewall friction, the thickness of sand layer in the chamber should be limited, so that the side-friction between the sand the sidewall of the chamber could be minimized.
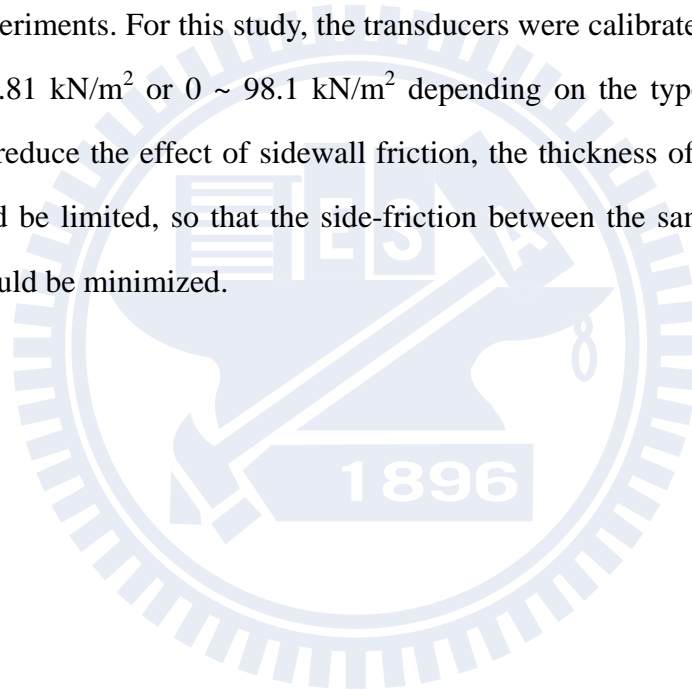
Table A.1. Soil Pressure Transducer Calibration Factors

Type	Transducer No.	Dynamic Strain Amplifer		Capacity (kN/m^2)	Calibration Function P=[Factor]*V (kN/m^2)
		No.	Calibration Setter($\mu\xi$)		
BE-2KCM17	090170006	8	289	98.1	P=40.167V
BE-2KCM17	090170007	9	300	98.1	P=39.739V
BE-2KCM17	090170008	10	269	98.1	P=39.419V
BE-2KCM17	9Z0080001	11	305	98.1	P=39.844V
BE-2KCM17	9Z0080002	12	340	98.1	P=41.552V

Calibration pressure range：0~98.1 kN/m^2

Table A.2. Soil Pressure Transducer Calibration Factors

Type	Transducer No.	Dynamic Strain Amplifer		Capacity (kN/m^2)	Calibration Function P=[Factor]*V (kN/m^2)
		No.	Calibration Setter($\mu\xi$)		
PGM-02KG	EE2450023	1	1984	19.62	P=3.1683V
PGM-02KG	EX3270002	2	2014	19.62	P=3.4484 V
PGM-02KG	EZ0660017	3	2014	19.62	P=3.495V
PGM-02KG	EZ0660029	4	2090	19.62	P= 3.4464V
PGM-02KG	FL8550010	5	1880	20	P= 3.931V
PGM-02KG	FL8550011	6	2047	20	P= 4.0769V
PGM-02KG	FG6900006	7	1815	20	P=3.889V

Calibration pressure range：0~9.81 kN/m^2
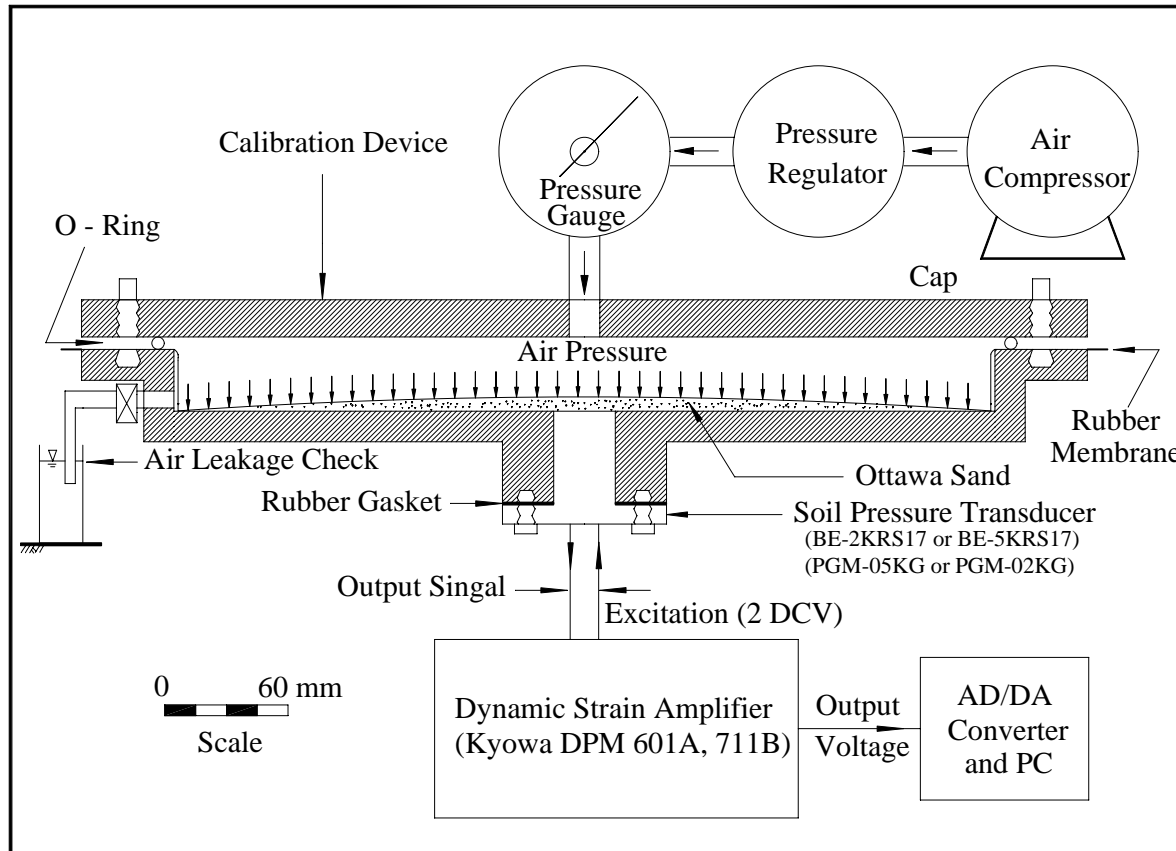
Fig. A1. Schematic diagram of on-wall soil pressure transducer calibration system
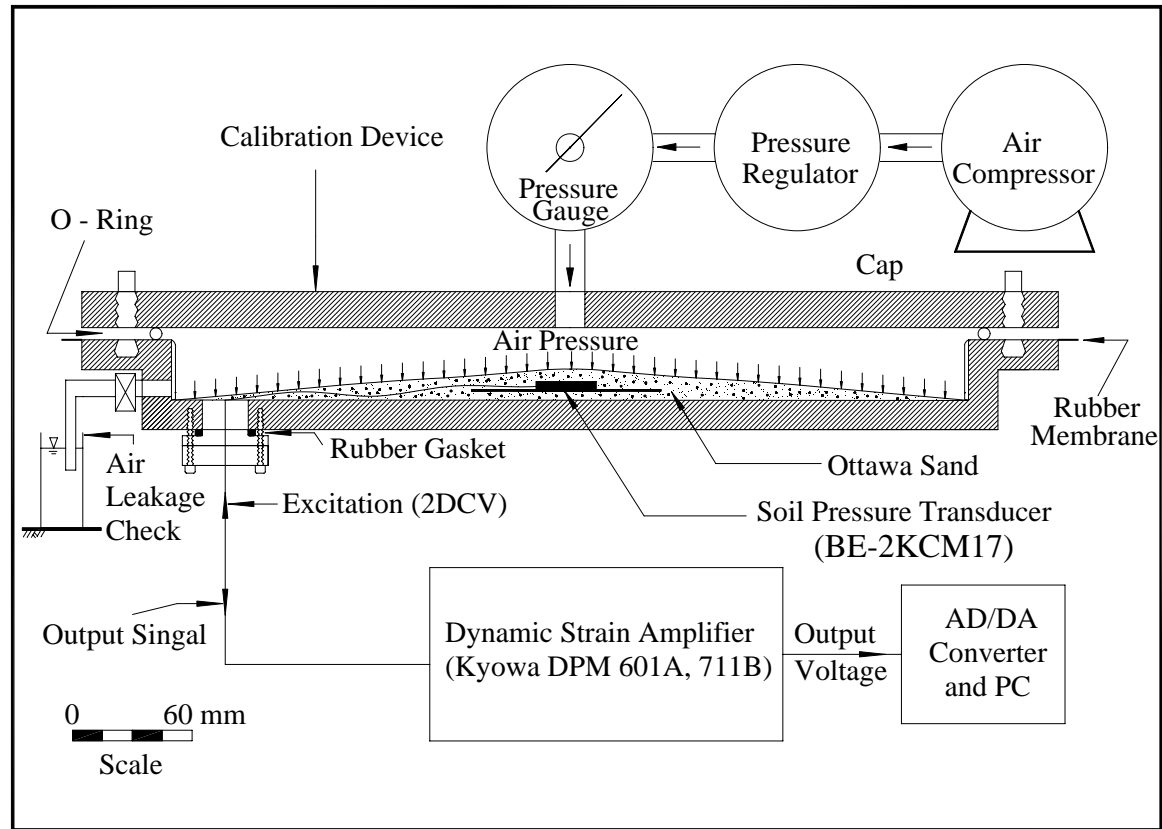
Fig. A2. Schematic diagram of in-soil soil pressure transducer calibration system
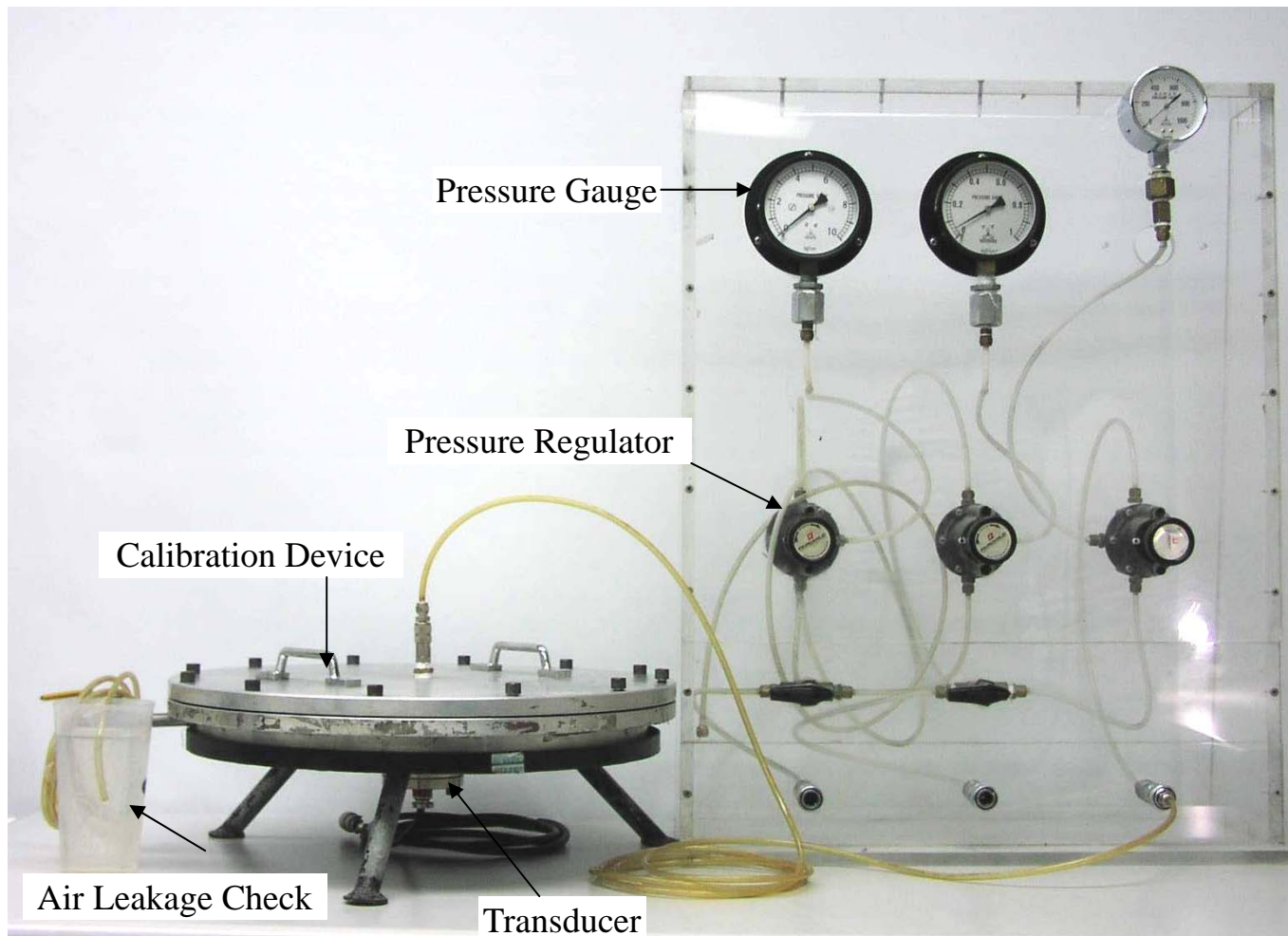
Fig. A3. Soil pressure transducer calibration system

Appendix B

Test Results of Dynamic Stress Path

Appendix B shows the values of test results of dynamic stress path in Test 0805.
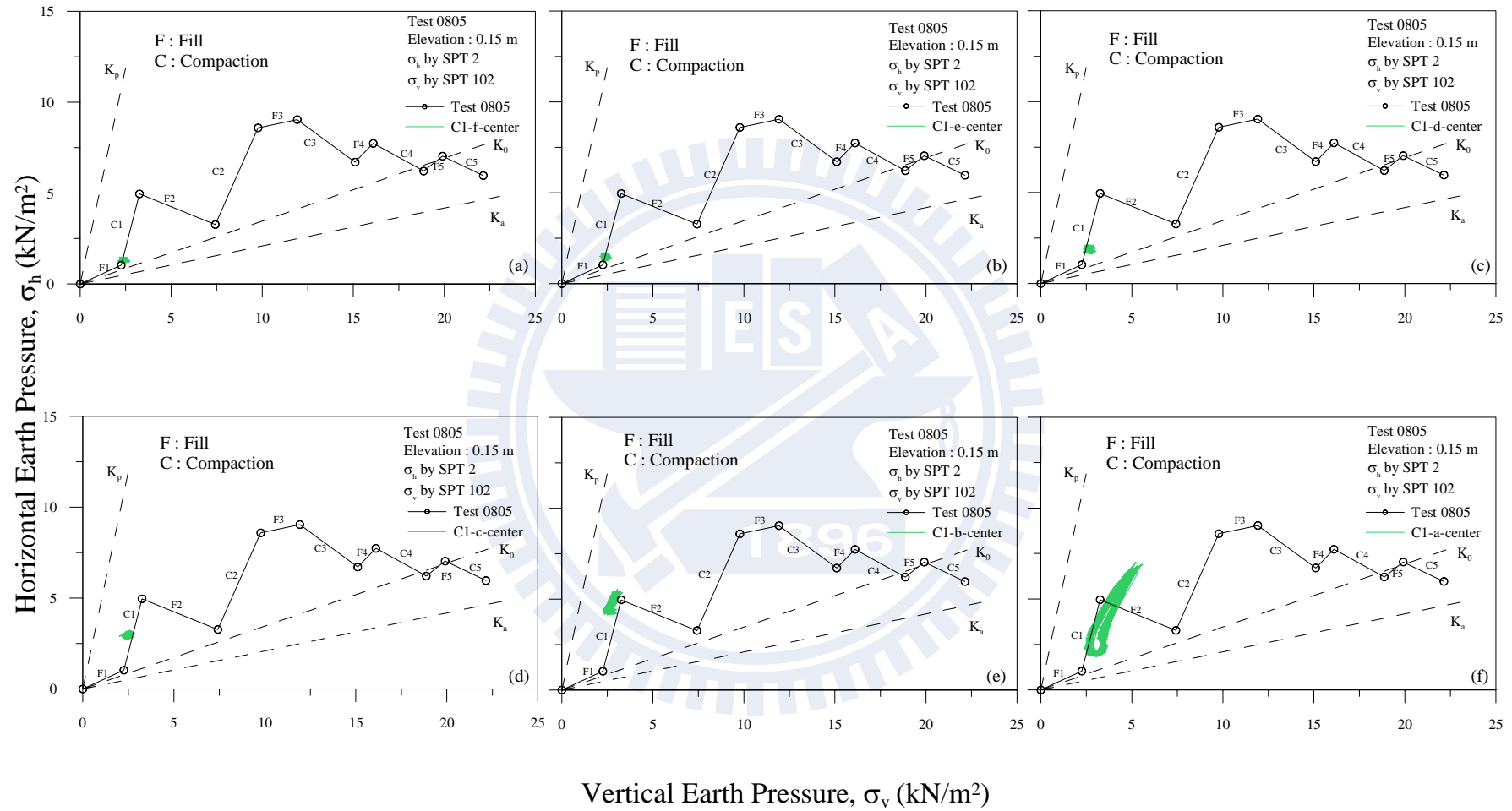
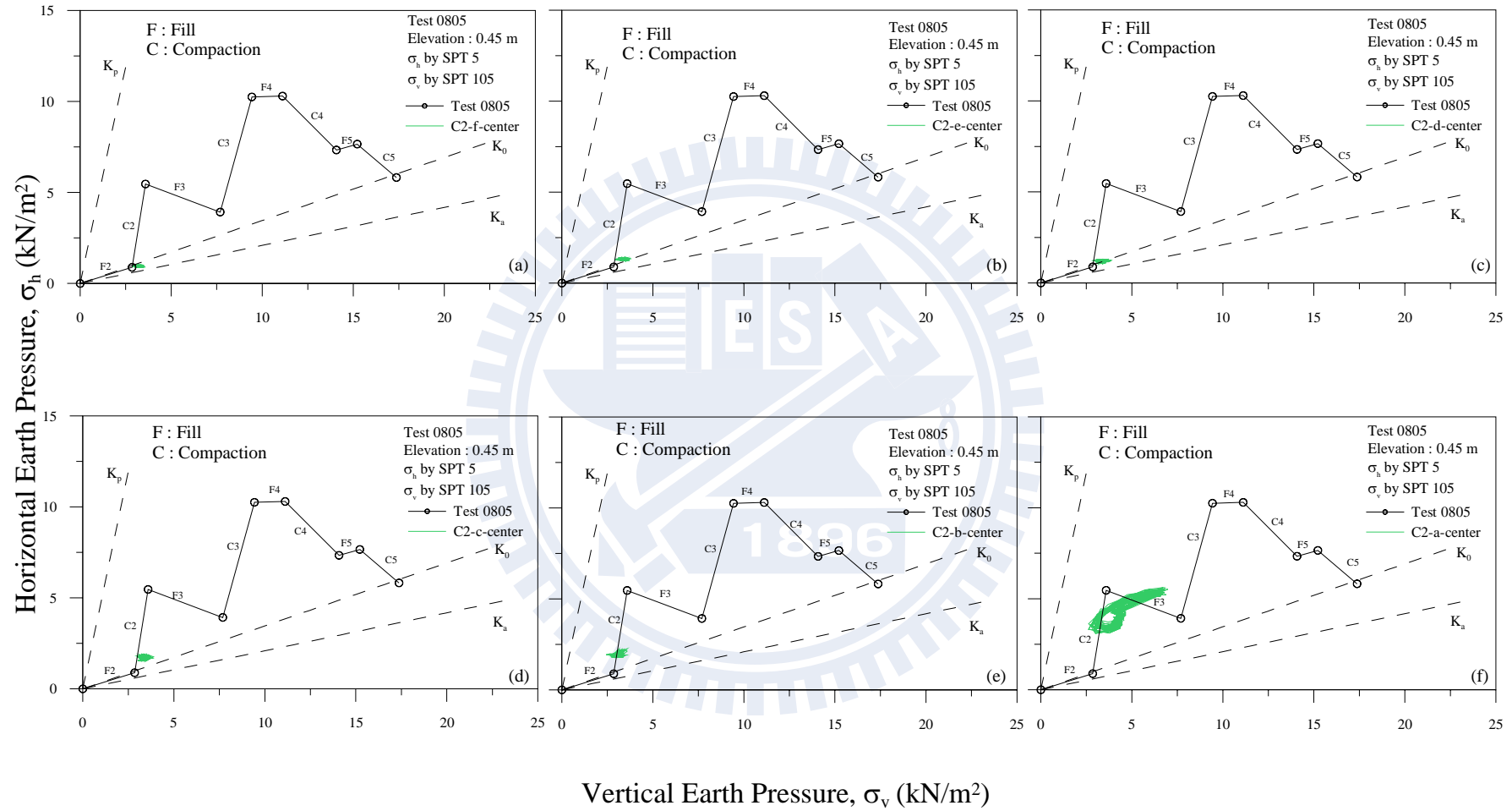Fig. B.1. Stress paths measured at center part of the model wall by SPT2 and SPT102 due to compaction on lift 1 from Lane f to Lane a

Fig. B.2. Stress paths measured at center part of the model wall by SPT5 and SPT105 due to compaction on lift 2 from Lane f to Lane a

120
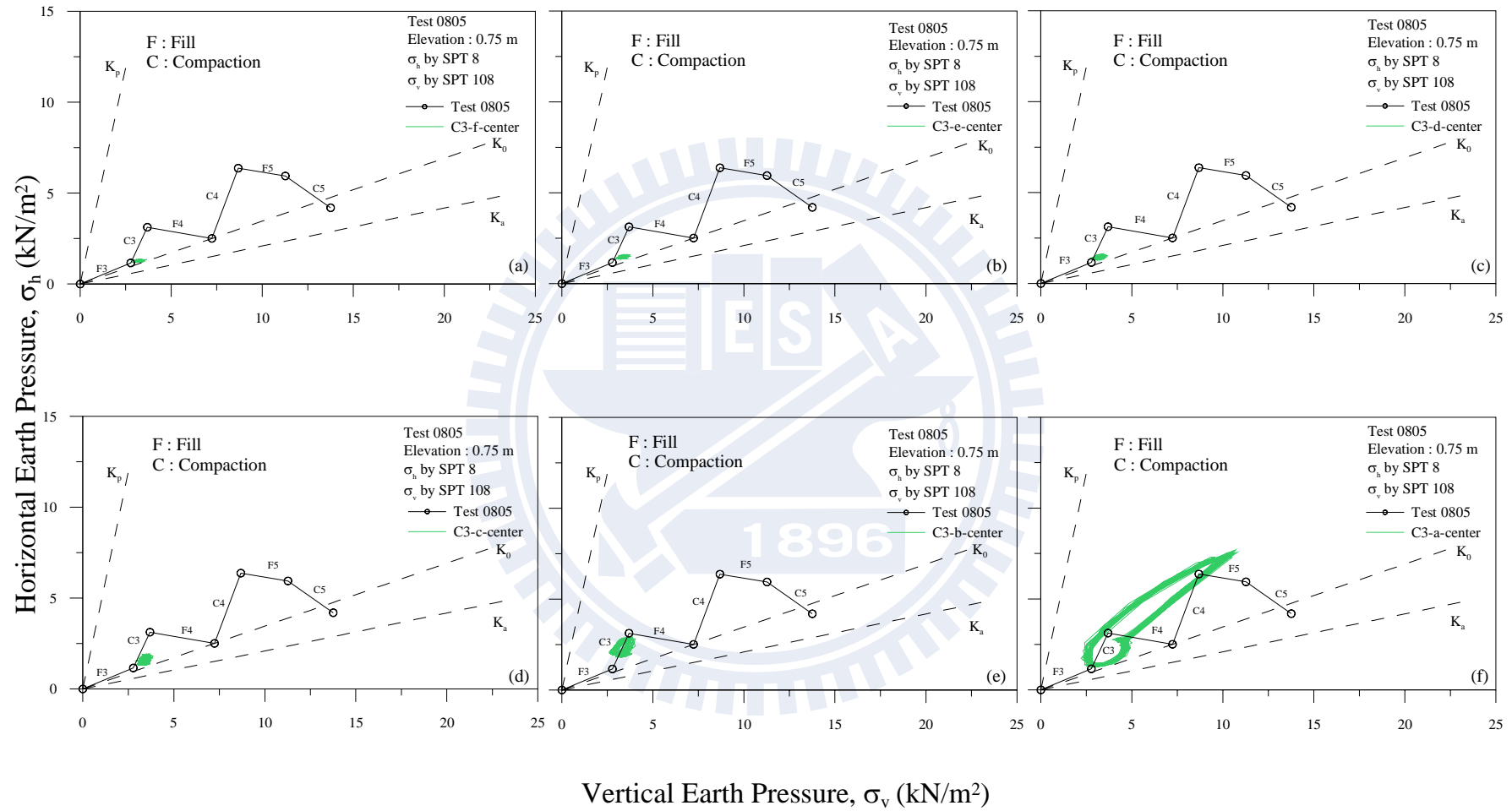
Fig. B.3. Stress paths measured at center part of the model wall by SPT8 and SPT108due to compaction on lift 3 from Lane f to Lane a

121
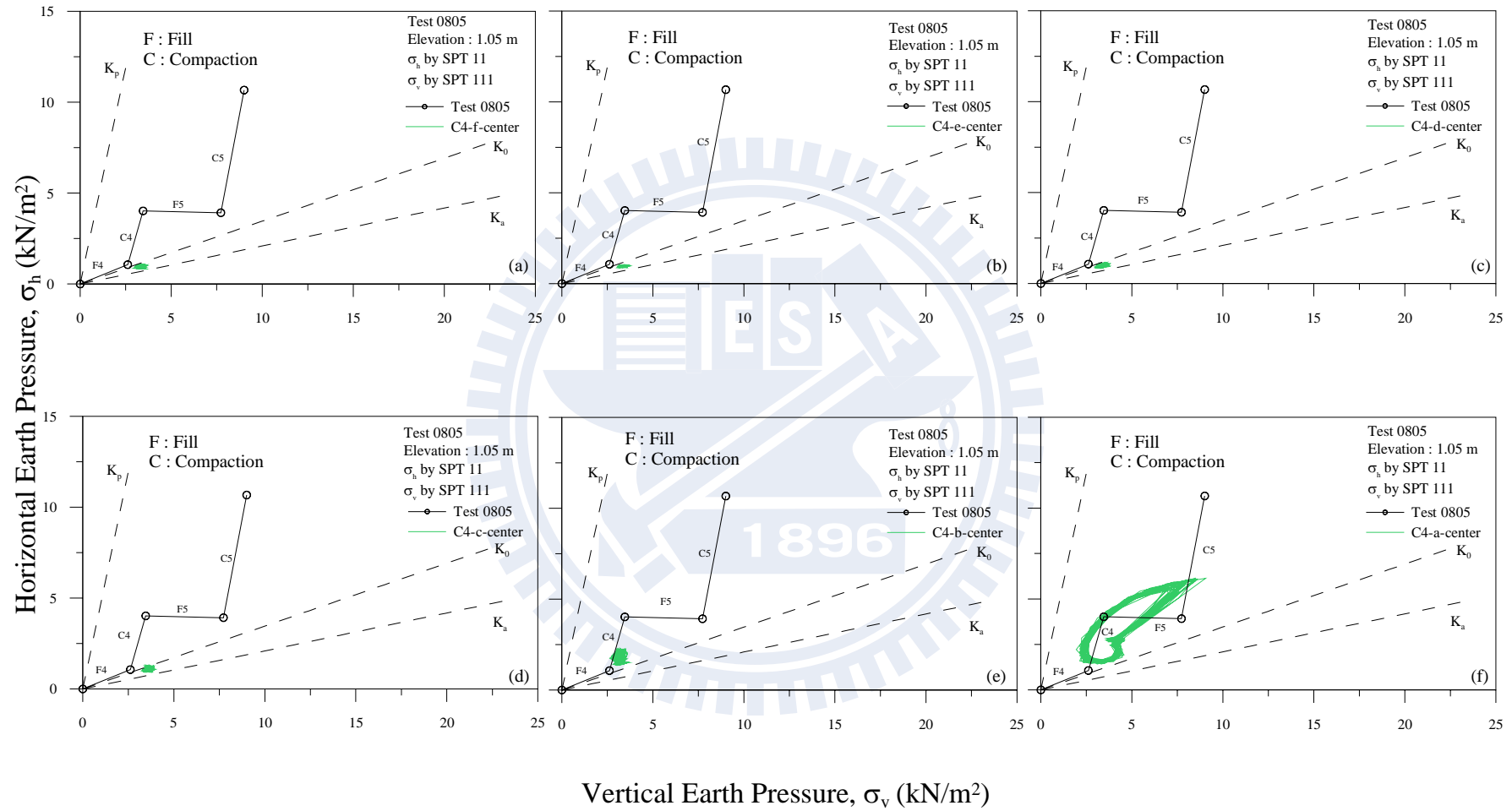
Fig. B.4. Stress paths measured at center part of the model wall by SPT11 and SPT111 due to compaction on lift 4 from Lane f to Lane a
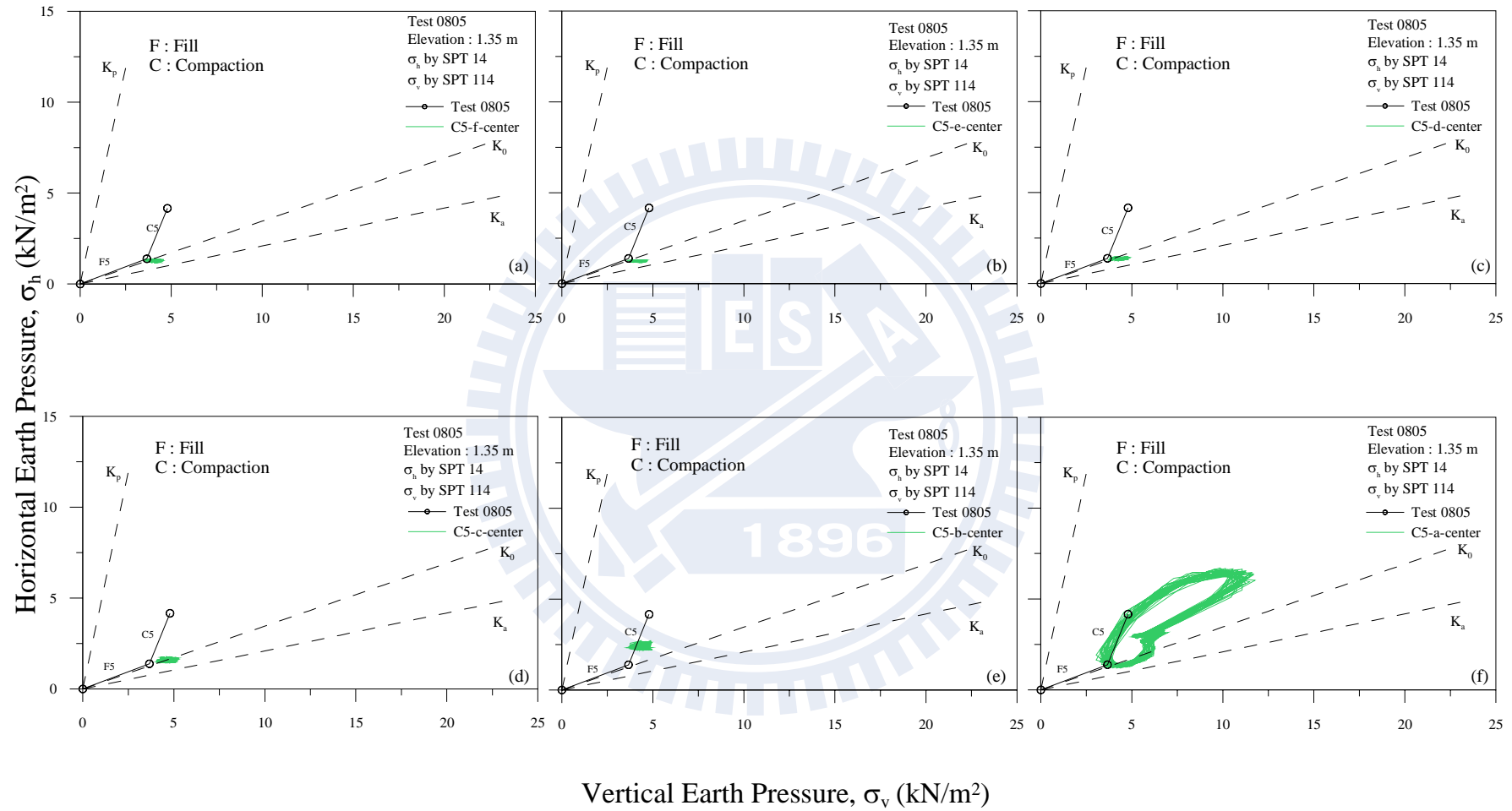
Fig. B.5. Stress paths measured at center part of the model wall by SPT14 and SPT114 due to compaction on lift 5 from Lane f to Lane a
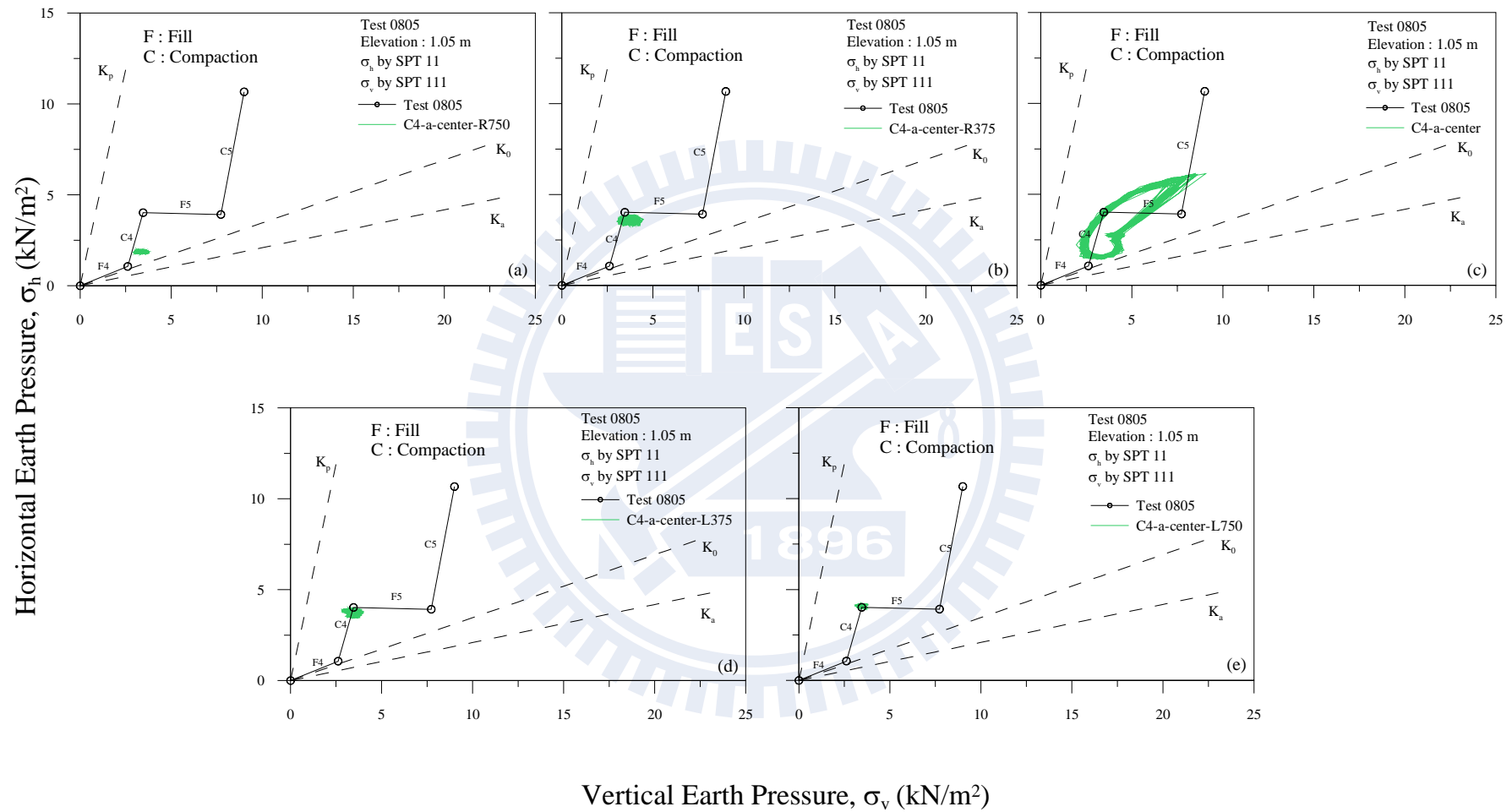
123
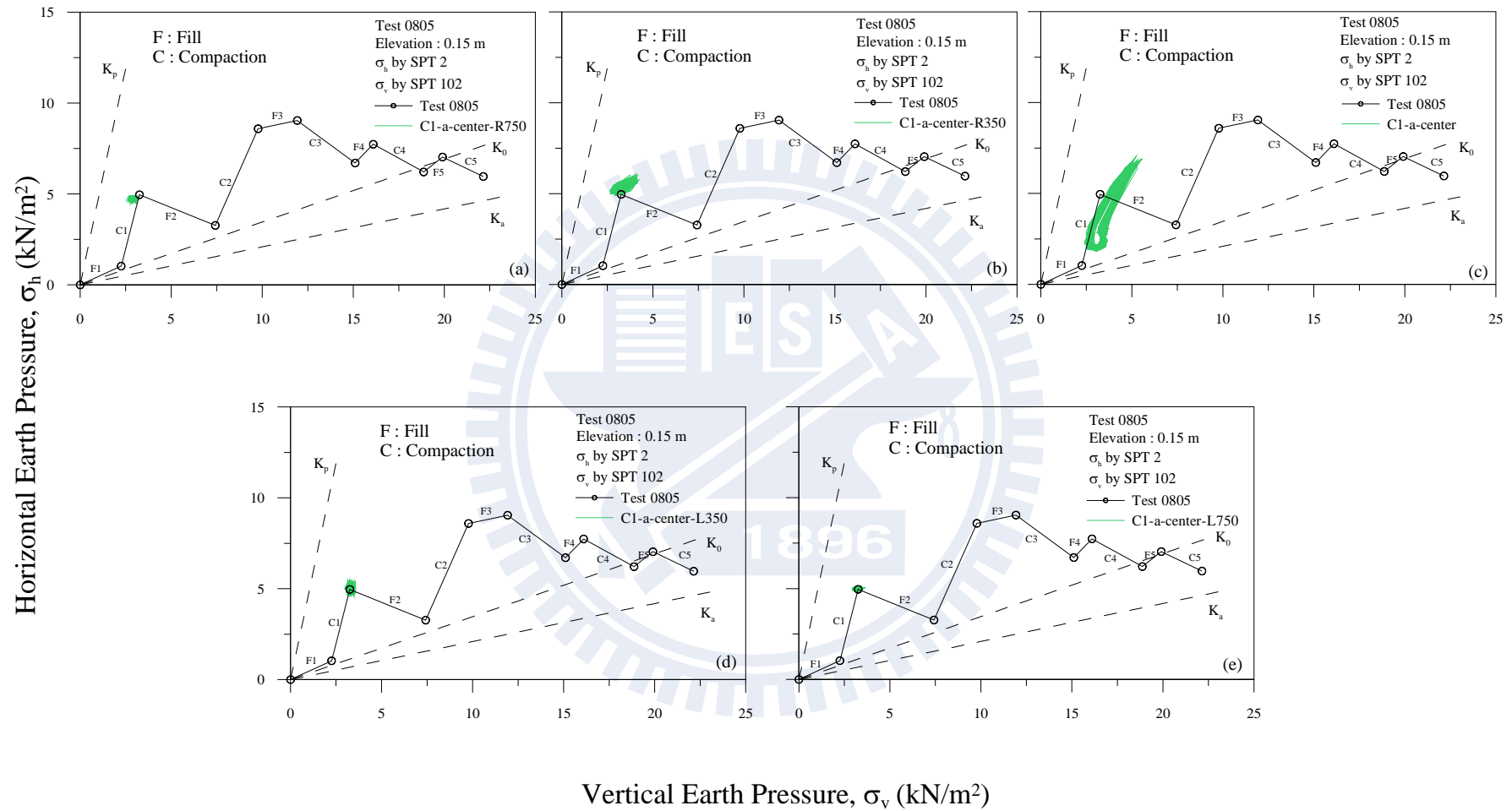
Fig. B.6. Stress paths measure at SPT2 and SPT102 due to compaction on Lane (near the wall) of Lift 1 from R750 to L750
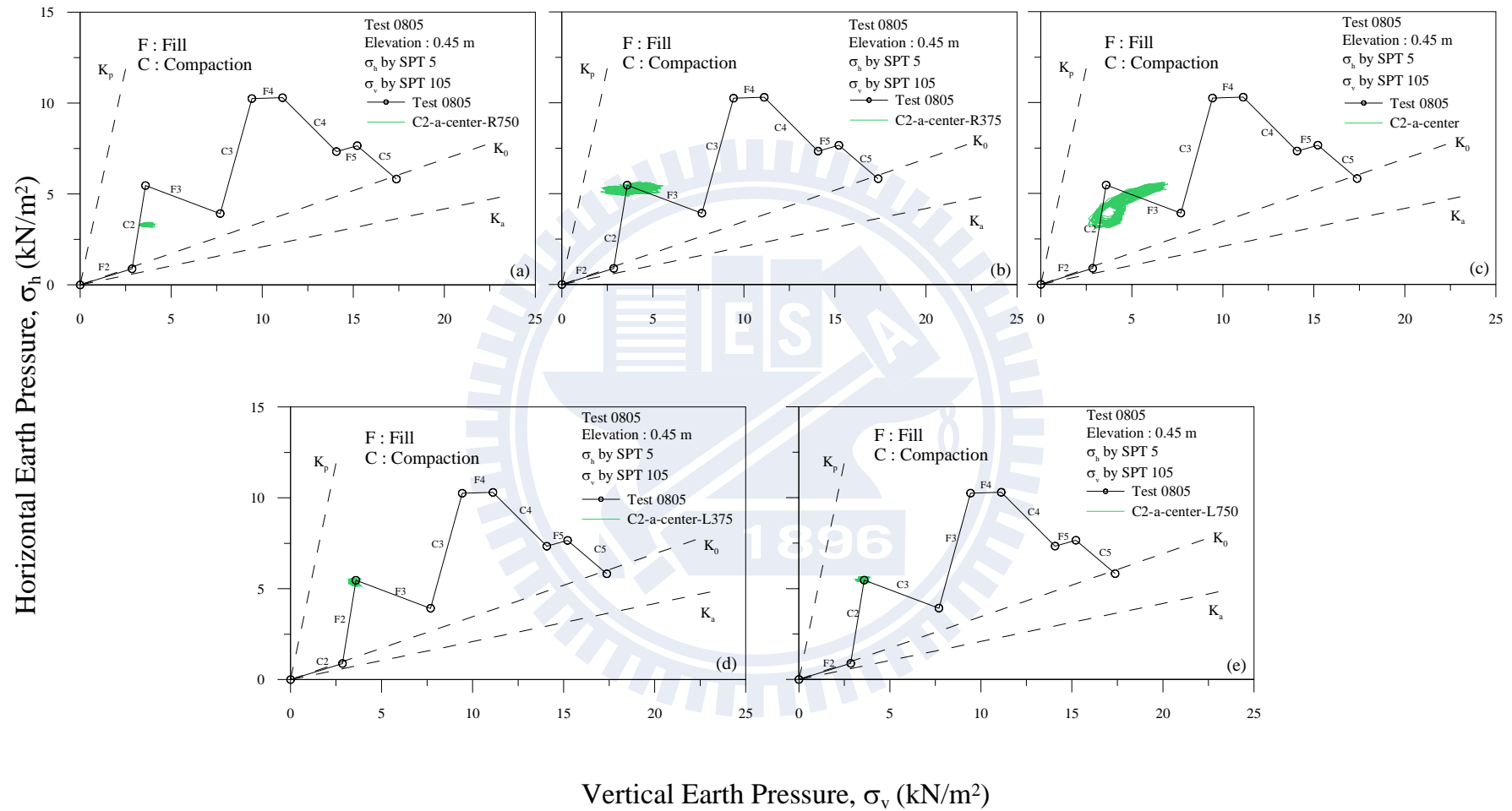
Fig. B.7. Stress paths measure at SPT5 and SPT105 due to compaction on Lane (near the wall) of Lift 2 from R750 to L750
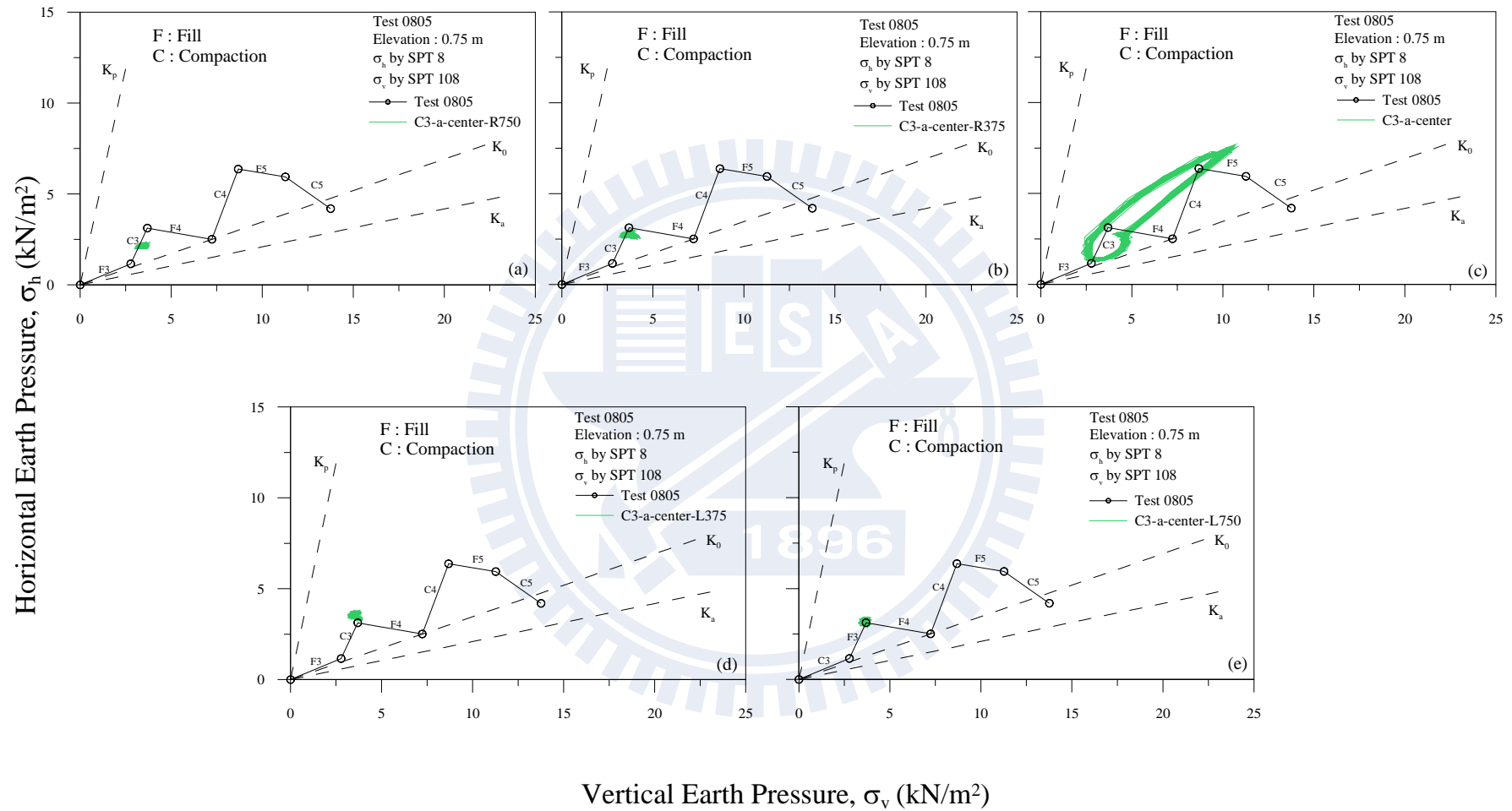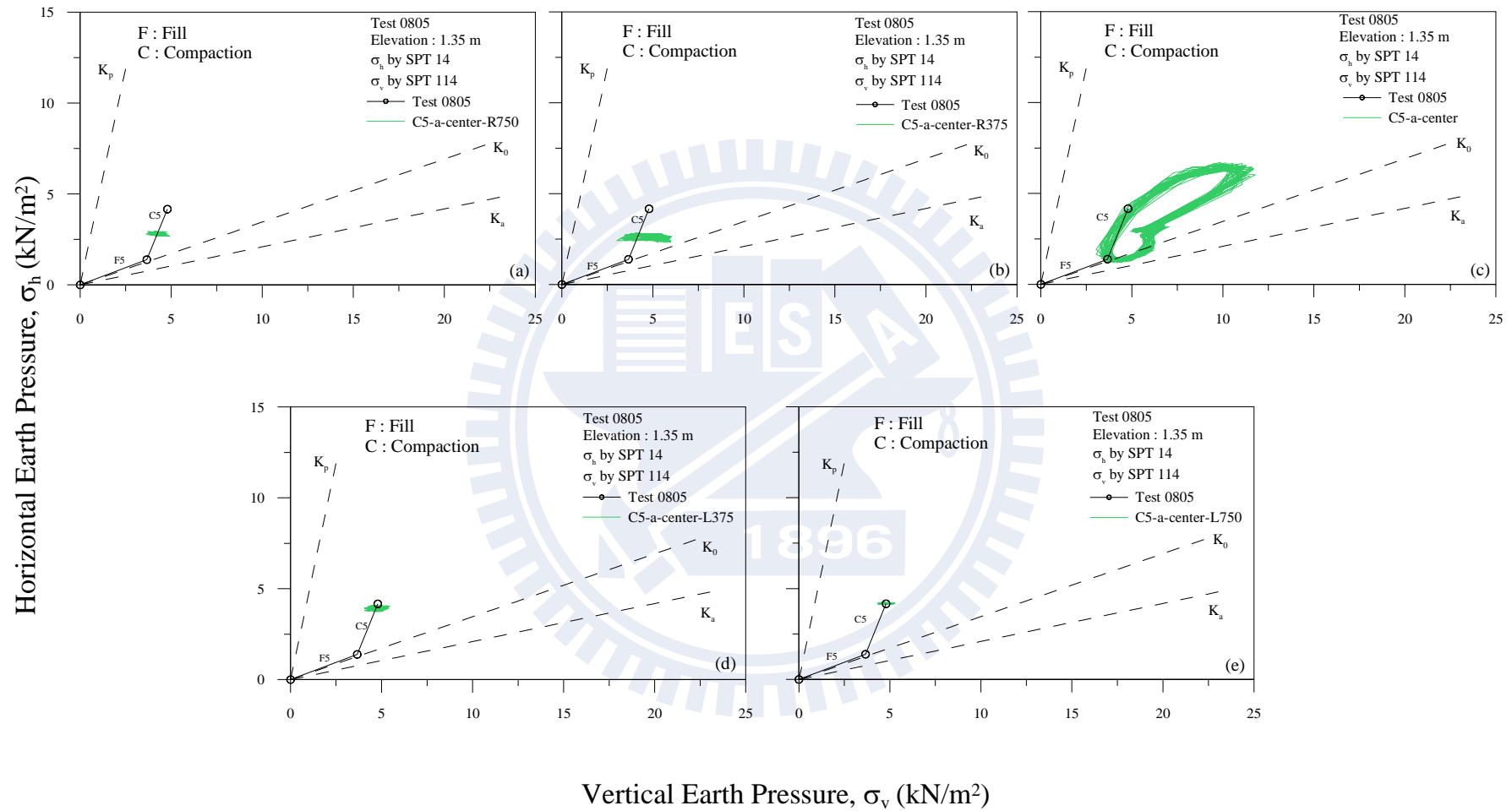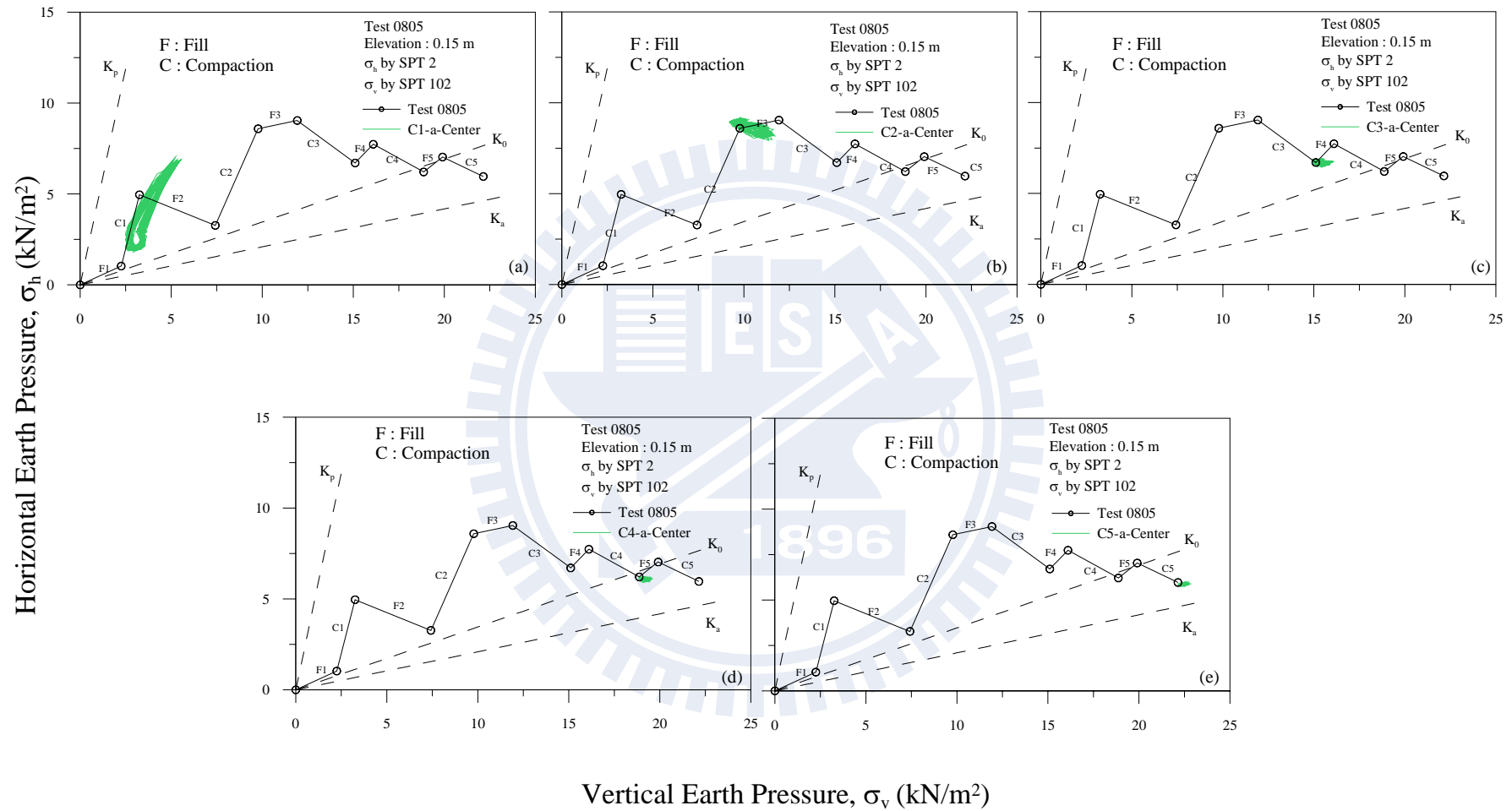
Fig. B.8. Stress paths measure at SPT8 and SPT108 due to compaction on Lane (near the wall) of Lift 3 from R750 to L750

126

Fig. B.9. Stress paths measure at SPT11 and SPT111 due to compaction on Lane (near the wall) of Lift 4 from R750 to L750

Fig. B.10. Stress paths measure at SPT14 and SPT114 due to compaction on Lane (near the wall) of Lift 5 from R750 to L750

Fig. B.11. Stress paths measure at SPT2 and SPT102 due to compaction on center part of Lane a (near the wall) of Lift 1 to Lift 5
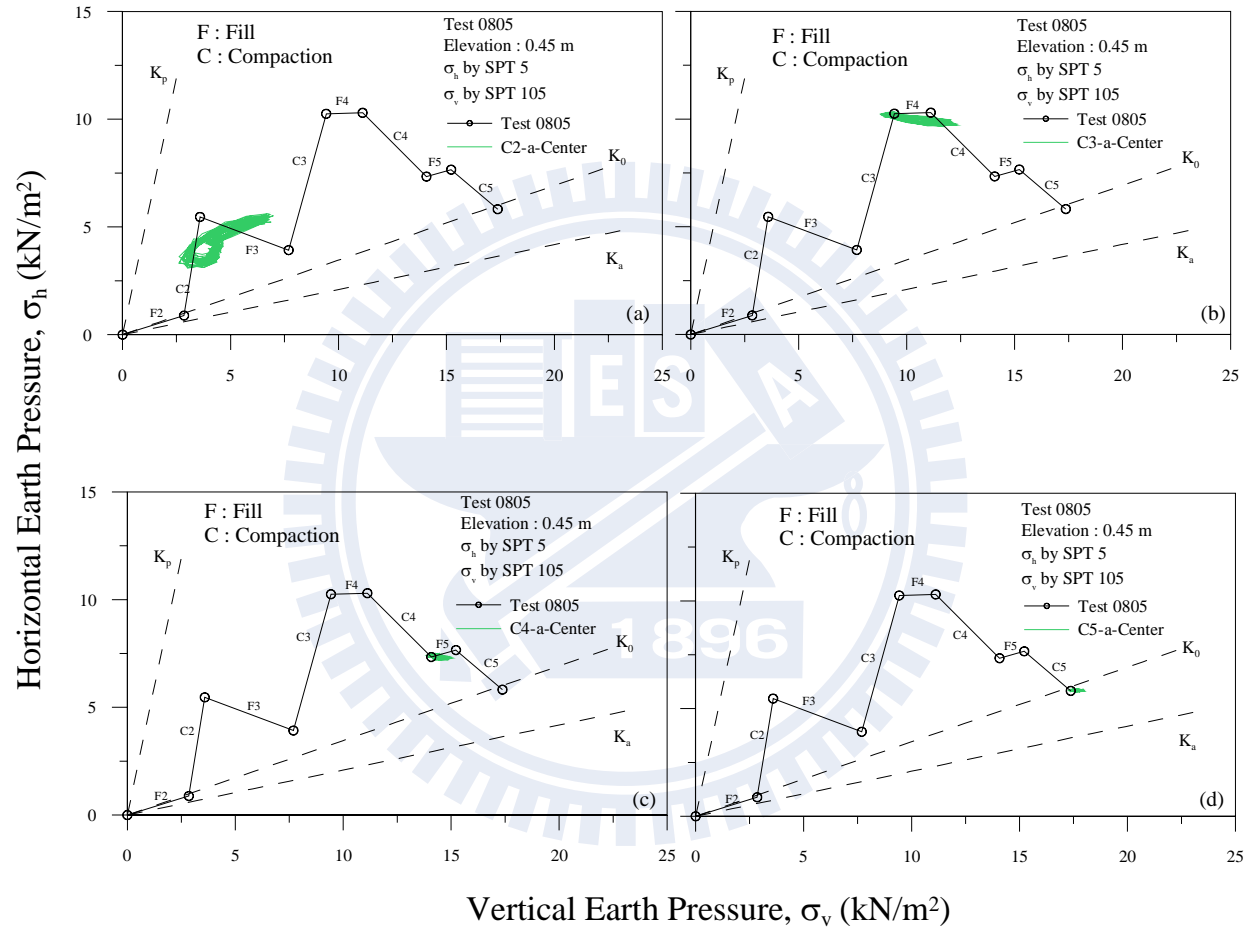
129

Fig. B.12. Stress paths measure at SPT5 and SPT105 due to compaction on center part of Lane a (near the wall) of Lift 2 to Lift 5
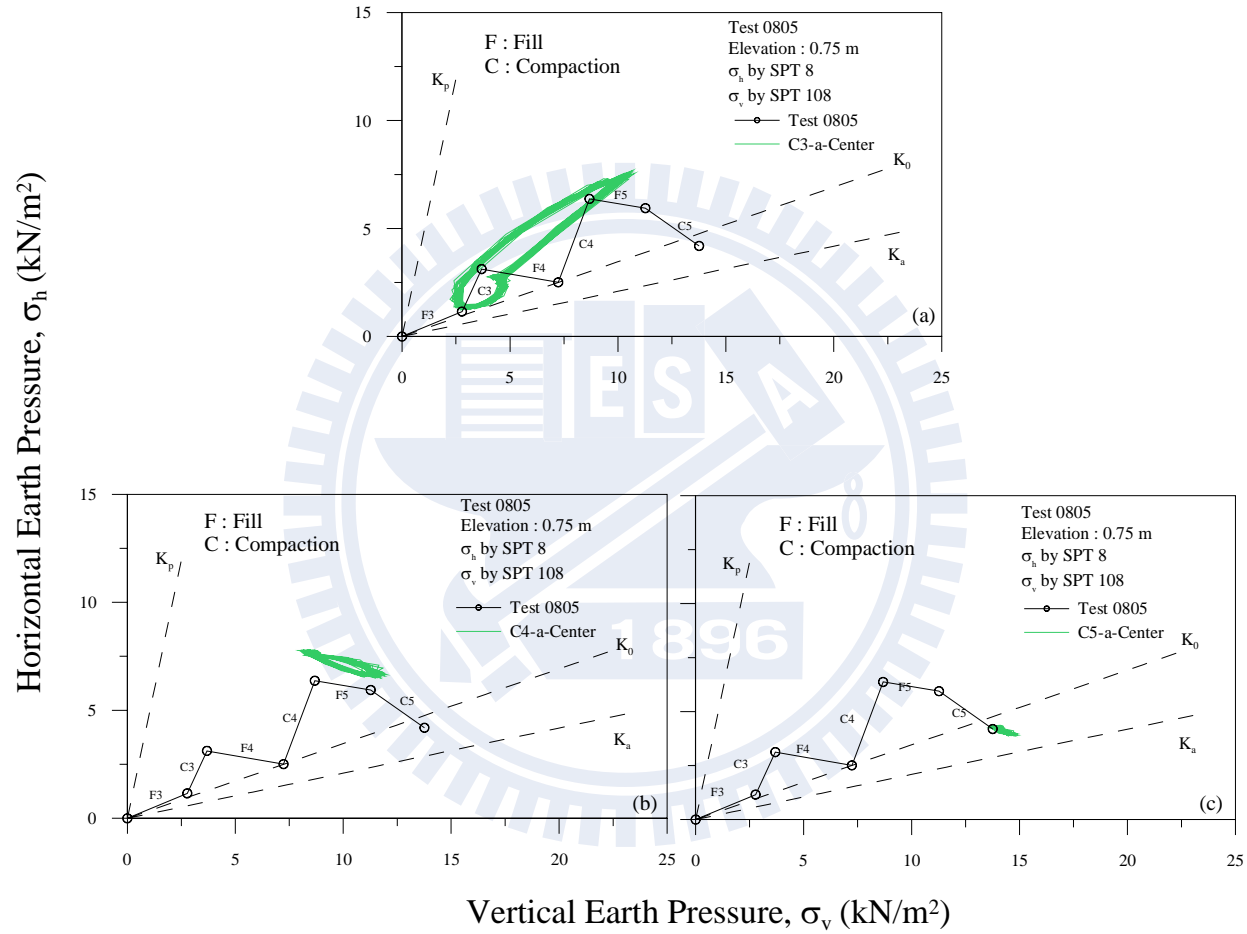
Fig. B.13. Stress paths measure at SPT8 and SPT108 due to compaction on center part of Lane a (near the wall) of Lift 3 to Lift 5
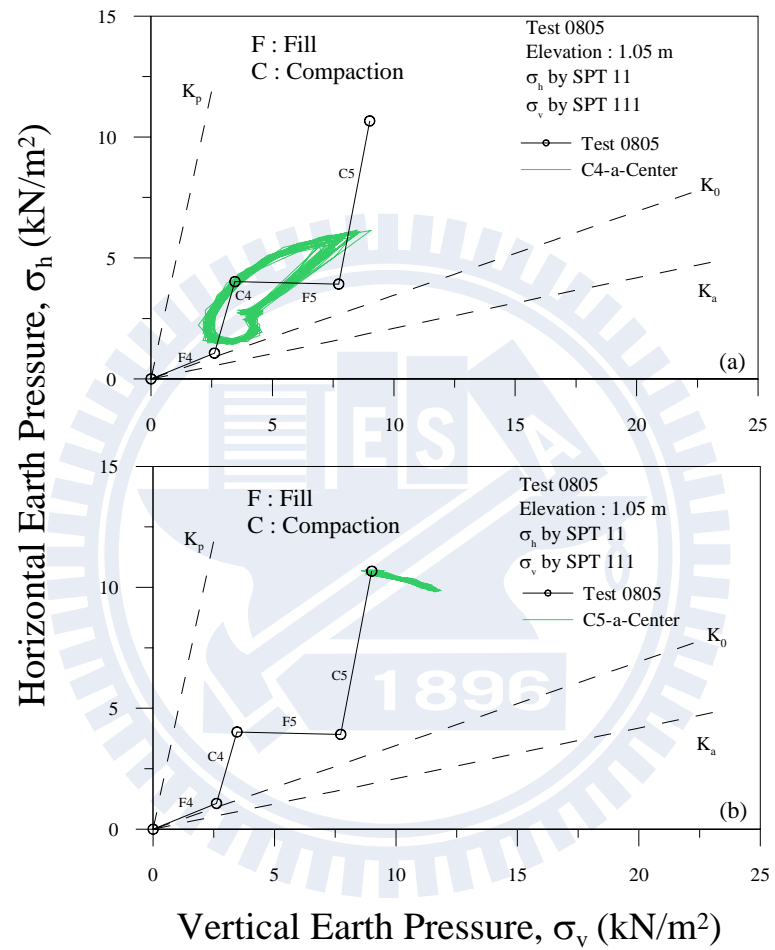
Fig. B.14. Stress paths measure at SPT11 and SPT111 due to compaction on center part of Lane a (near the wall) of Lift 4 to Lift 5
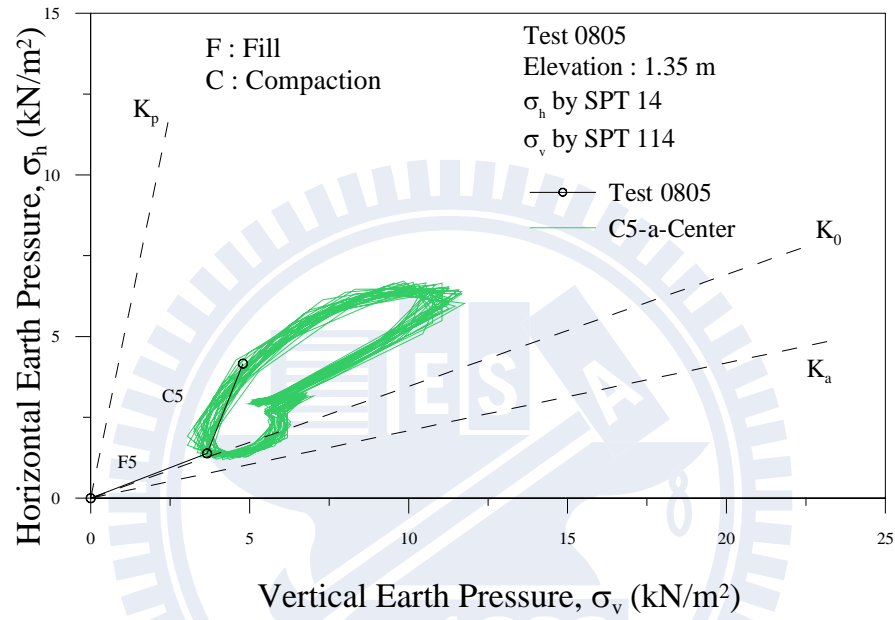
Fig. B.15. Stress paths measure at SPT14 and SPT114 due to compaction on center part of Lane a (near the wall) of Lift 5